# Integral field spectroscopy of H II regions in M33

Jesús López-Hernández,[1]⋆ Elena Terlevich,[1] Roberto Terlevich,[1,2]
Daniel Rosa-González,[1] Ángeles Díaz,[3] Rubén García-Benito,[4]
José Vílchez[4] and Guillermo Hägele[3,5,6]

[1]*Instituto Nacional de Astrofísica, Óptica y Electrónica, Luis Enrique Erro 1. Tonantzintla, Puebla, CP 72840, Mexico*
[2]*Institute of Astronomy, Madingley Road, Cambridge CB3 0HA, UK*
[3]*Departamento de Física Teórica, C-XI, Universidad Autónoma de Madrid, E-28049 Madrid, Spain*
[4]*Instituto de Astrofísica de Andalucía (CSIC), Glorieta de la Astronomía s. n., E-18008 Granada, Spain*
[5]*Consejo Nacional de Investigaciones Científicas y Técnicas (CONICET), Argentina*
[6]*Facultad de Ciencias Astronómicas y Geofísicas, Universidad Nacional de La Plata, Paseo del Bosque s/n, 1900 La Plata, Argentina*

## ABSTRACT

Integral field spectroscopy is presented for star-forming regions in M33. A central area of $300 \times 500 \, \text{pc}^2$ and the external H II region IC 132, at a galactocentric distance ∼19 arcmin (4.69 kpc), were observed with the Potsdam Multi-Aperture Spectrophotometer instrument at the 3.5-m telescope of the Centro Astronómico Hispano–Alemán (CAHA, aka Calar Alto Observatory). The spectral coverage goes from 3600 Å to 1 µm to include from [O II] $\lambda$3727 Å to the near-infrared lines required for deriving sulphur electron temperature and abundance diagnostics.

Local conditions within individual H II regions are presented in the form of emission-line fluxes and physical conditions for each spatial resolution element (spaxel) and for segments with similar H$\alpha$ surface brightness.

A clear dichotomy is observed when comparing the central to outer disc H II regions. While the external H II region has higher electron temperature plus larger H$\beta$ equivalent width, size and excitation, the central region has higher extinction and metal content.

The dichotomy extends to the Baldwin–Phillips–Terlevich (BPT) diagnostic diagrams that show two orthogonal broad distributions of points. By comparing with pseudo-3D photoionization models, we conclude that the bulk of observed differences are probably related to a different ionization parameter and metallicity.

Wolf–Rayet (WR) features are detected in IC 132, and resolved into two concentrations whose integrated spectra were used to estimate the characteristic number of WR stars. No WR features were detected in the central H II regions despite their higher metallicity.

**Key words:** ISM: abundances – H II regions – galaxies: individual: M33.

## 1 INTRODUCTION

Extragalactic H II regions provide an excellent laboratory to study star formation processes, evolution of massive stars and the properties of the surrounding interstellar medium. A wealth of information can be obtained from the spectral analysis of the bright emission lines and the stellar continuum.

The spectral information from extragalactic H II regions has been traditionally obtained from single-aperture or long-slit observations of the brightest part of the region. The data are then used to derive the physical conditions of the gas (temperatures and densities)

and to estimate abundances and ionization conditions, as well as characteristics of the ionizing star clusters [masses, ages, effective temperatures ($T_*$)]. These results constitute the main body of our knowledge regarding the evolution of disc galaxies (see e.g. Aller 1942; Searle 1971; Smith 1975; Pagel et al. 1979; Díaz et al. 1987; Vílchez et al. 1988; Dinerstein 1990; Kennicutt 1998; Skillman 1998; Bresolin et al. 2004).

Underpinning this proven methodology to study the emission-line spectra lies the tacit assumption that the observations and the derived measurements are representative of the whole H II region, basically internal variations within the nebula are assumed to be minimal or non-existent. The limitation of this assumption has long been recognized (Díaz et al. 1987; Rubin 1989; Castañeda et al. 1992); however, in the majority of the cases any solution has

⋆ E-mail: jlopez@inaoep.mx

been precluded by limitations in the observation technology and optimization of the assigned observing time. Nevertheless some options have been available to combine spectral information with spatial resolution. A simple solution is to sweep the H II region following a direction perpendicular to the slit elongation (Kosugi et al. 1995; Maíz-Apellániz et al. 2005) in steps separated by one slit width. A different approach involves the use of a set of narrow-band filters to obtain monochromatic images centred on the emission lines that, when combined with neighbouring continuum bands, allows the extraction of pure emission images. Tunable filters with Fabry–Perot interferometers offer a more flexible scheme by allowing the use of various passbands, centred at different wavelengths.

Of particular interest for this work is the technique of integral field spectroscopy (IFS; Allington-Smith 2006), also known as 3D or area spectroscopy, in which by the use of integral field units (IFUs) it is possible to obtain simultaneous spectral and spatial information over the observed object. The main advantage of the IFS approach over other techniques is that the observation is simultaneous in space and wavelength, producing an homogeneous set of data. The drawback of IFS is the small field of view (FOV); thus, the selection of the optimal method (tuneable filters, long-slit sweeping, IFS) for spatially resolved observations depends on the objective of each specific project.

IFS has proved its utility in observations of luminous and ultra-luminous infrared (IR) galaxies (Alonso-Herrero et al. 2009, 2010; García-Marín et al. 2009), the nuclei of active galaxies (Barbosa et al. 2009), circumnuclear star-forming regions (Dors et al. 2008) and blue compact galaxies (Cairós et al. 2009a,b; Lagos et al. 2009; James, Tsamis & Barlow 2010; Pérez-Montero et al. 2011). Some H II regions have been studied with IFS, including the observations of H II regions in the outer disc of NGC 6946 (García-Benito et al. 2010, with the same instrument and setup as in this work). IFS of H II regions in M33 has been already obtained [see Monreal-Ibero et al. (2011) and Relaño et al. (2010) for NGC 588 and 595, respectively]; in both cases the Potsdam Multi-Aperture Spectropho-tometer (PMAS) instrument at the 3.5-m telescope of the Centro Astronómico Hispano–Alemán (CAHA, aka Calar Alto Observa-tory) was used. They compared the distribution maps for different parameters against the reported values in the literature, obtaining a good agreement when the IFS data are integrated in a single spec-trum and noting that for some quantities (e.g. extinction) to assume a single value for the whole region is not strictly correct. For some of the empirical abundance estimators a spatial dispersion is present; however, the variation is within the estimated observational error and in such cases a uniform distribution may be assumed.

The general objectives of this work are, using IFS data for the centre and an external region of M33, to characterize the extent of the internal variations in H II regions for measured and de-rived values, to test whether the description of the whole H II region with a single value for different parameters is valid, to map the massive star content using characteristic spectral features [i.e. Wolf–Rayet (WR) stars] and to compare internal variations in high-metallicity (inner) versus low-metallicity (outer) H II regions. Also, given that the central region remains an ill-defined zone with scarce spectroscopic observations, IFS may contribute to its better characterization.

The organization of this paper is as follows. The observations, data reduction and integrated emission-line maps are described in Section 2. Section 3 describes the physical conditions of the gas. Section 4 concerns the chemical abundance determinations. Section 5 is devoted to the discussion of diagnostic diagrams. The detection

**Table 1.** M33 properties.

| Designations | Messier 033, Triangulum galaxy, NGC 0598, UGC 01117, PGC 005818 |
|---|---|
| Classification | SA(s)cd H II |
| Major diameter | 70.8 arcmin |
| Minor diameter | 41.7 arcmin |
| Position angle | 23° |
| Distance | 840 kpc (Freedman et al. 2001) |
| Redshift | $-0.000\,597 \pm 0.000\,010$ |
| Inclination angle | 53°.52 (Corbelli & Salucci 2000) |
| PPak scale | 4.07 pc arcsec$^{-1}$ (10.91 pc fibre$^{-1}$) |

*Note.* Source is NED unless otherwise specified.

of WR features is presented in Section 6. Analysis in projected shells is shown in Section 7. Finally, the conclusions are presented in Section 8.

## 2 OBSERVATIONS AND DATA REDUCTION

### 2.1 Object selection

M33 is the third brightest member of the Local Group (Van den Bergh 2000). Given its proximity, large angular size and low incli-nation, it is an ideal candidate for IFS observations, having a rich content of H II regions in the central region and across the disc at different galactocentric distances, allowing the exploration of re-cent star formation activity in a wide range of physical conditions. Hundreds of nebulae have been charted in M33 (Hodge, Skelton & Ashizawa 2002) and included in abundance and gradient studies (Vílchez et al. 1988; Crockett et al. 2006; Rosolowsky & Simon 2008; Bresolin et al. 2010). Table 1 summarizes the main properties of the galaxy. The values are obtained from NED[1] wherever no references are given.

As a first step of a larger project aimed to trace the chemical abundances, gradient and dispersion of physical conditions with high spatial resolution across M33, we obtained IFS data of the centre and the external H II region IC 132 located to the north-west of the centre of M33 at a galactocentric distance of ∼19 arcmin or 4.69 kpc (see Fig. 1).

The observed locations represent two scenarios of star formation in spiral galaxies with extremely different environments: outer spiral disc and central regions. Notorious differences between the two (disc versus central) exist regarding the star formation rate (20 versus 1000 M$_\odot$ yr$^{-1}$), star formation time-scales (1 Myr versus 1 Gyr) and electron density (10 versus $10^4$ cm$^{-3}$) among others (Kennicutt, Keel & Blaha 1989; Kennicutt 1998).

#### 2.1.1 The central region of M33

The central region of M33 has been the subject of various studies, given its notorious star formation activity (Keel 1983). From the fact that the dominant stellar population in the centre of M33 is young (<1 Gyr) and metal rich (up to solar metallicities), Van den Bergh (1991) suggested that the stars are the product of intense star-forming periods originated by the inflow of gas.

Star formation in the centre of spiral galaxies has been associated with the existence of bulges and bars. However, the presence of

---

[1] This research has made use of the NASA/IPAC Extragalactic Database (NED) which is operated by the Jet Propulsion Laboratory, California Insti-tute of Technology, under contract with the National Aeronautics and Space Administration (NASA).
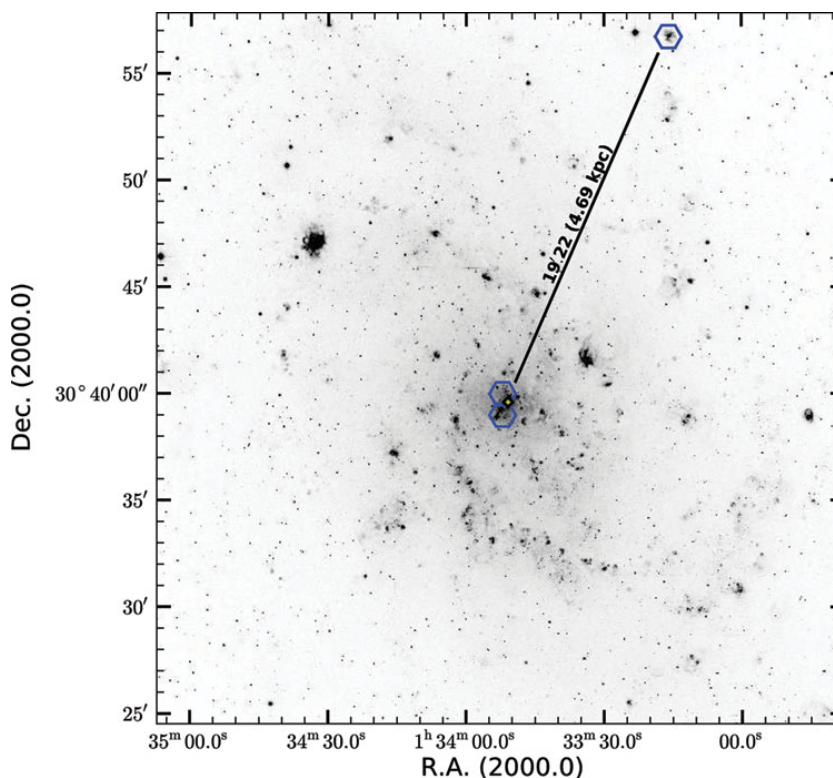
**Figure 1.** Position of the observed fields over M33. The hexagons are 74 arcsec in diameter. The diamond marks the centre of the galaxy with the coordinates RA = 01$^h$ 33$^m$ 50$^s$89, Dec. = +30° 39′ 36″80 (J2000). The outer region IC 132 has coordinates RA = 01$^h$ 33$^m$ 15$^s$90, Dec. = +30° 56′44″00 (J2000). North is up and east is left.

a bulge in M33 is controversial. The excess in surface brightness in the central region of M33 (Kent 1987) is not necessarily due to the existence of a bulge but may be explained by a large-scale diffuse halo (Bothun 1992, based on 12 μm photometry). By using *H*-band photometry of individual stars, Minniti, Olszewski & Rieke (1993) concluded that a bulge exists and that it has experienced a period of star formation less than 1 Gyr ago. The existence of a bar in M33 is also an open issue. Regan & Vogel (1994) propose that if a bar exists it has a length of 3 arcmin with a position angle of 90°. They also propose that the bar-like emission could be due to the continuation of the spiral arms. However, they claim that there is a lack of evidence in order to decide in favour of one or the other explanation. In any case, in M33 the bar-like structure contributes only 4 per cent to the total light out to 1.5 arcmin, in contrast with a 40 per cent contribution in strong barred galaxies (Blackman 1983). Also the existence of a massive central black hole has been discarded (Kormendy & McClure 1993; Massey et al. 1996) and no active galactic nucleus (AGN) like emission-line ratios have been reported. However, the centre of M33 harbours M33 X-8, the brightest ultraluminous X-ray source (ULX) in the Local Group. The observational evidence indicates that M33 X-8 emission originates in a stellar mass black hole ($M_{BH} \sim 10\,M_\odot$) with a super-Eddington accretion rate (Foschini et al. 2004; Weng et al. 2009; Middleton, Sutton & Roberts 2011). The position of M33 X-8 which coincides with the photometric centre of the galaxy is indicated with a cross symbol in the left-hand panel of Fig. 2.

The central region is an excellent scenario to study the star formation process in relatively high metallicity and density and low-excitation environments, offering a challenging scenario deviating from the conditions of the majority of H II region studies. Such conditions represent a test to the different abundance calibrators, gen-erally based on low-metallicity H II region samples (Kinkel & Rosa 1994; Bresolin et al. 2004) and extrapolated to the high-metallicity regime.

### 2.1.2 The outer disc region IC 132

IC 132 is one of the most external H II regions in M33, located 4.69 kpc (~19 arcmin) away from the centre. It ranks among the brightest in the galaxy and has been included in chemical composition and gradient studies (Aller 1942; Searle 1971; Smith 1975; Kwitter & Aller 1981; Magrini, Corbelli & Galli 2007a). WR features were detected from narrow-band interference filter surveys (Boksenberg, Willis & Searle 1977; D'Odorico & Benvenuti 1983). The metallicity has been reported ranging from 12 + log (O/H) = 7.85 to 8.08 with typical errors ~ 0.05 (Magrini et al. 2007b, 2010).

IC 132 shows the high-excitation, low-density and low-abundance environment typical of disc regions, for which in most of the H II studies, physical conditions and abundance estimators have been developed.

### 2.2 Observations

Observations were obtained with the CAHA 3.5-m telescope, using the PMAS instrument in fiber package (PPak) mode (Roth et al. 2005). With this configuration the IFU features 331 fibres for the science object packed in an hexagonal array with a FOV of 74 × 64 arcsec$^2$, surrounded by six bundles of six fibres each at a distance of 72 arcsec from the centre to sample the sky. 15 extra fibres, not on the focal plane, can be illuminated separately for calibration
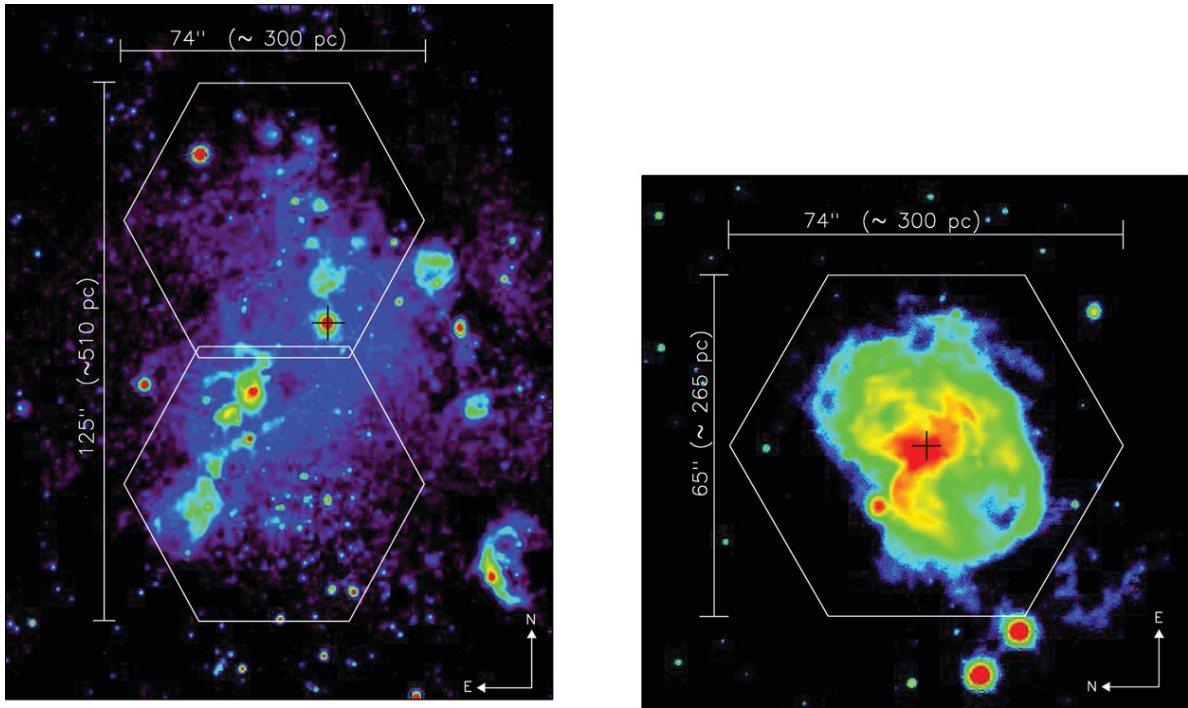
**Figure 2.** Identification of the observed fields. The images are narrow filters centred in Hα from the NOAO Science Archive (Massey et al. 2006). Overlaid is the PMAS-PPak hexagonal FOV. For the centre of M33 (left-hand panel), two consecutive fields are overlapped by one fibre line. The cross in the central regions indicates the centre of the galaxy coincident with the ULX M33 X-8; for IC 132 (right-hand panel) the cross marks the centre of the region. The scale in parsecs corresponds to the assumed distance to M33 of 840 kpc.

purposes. Although the unit contains more fibres to provide protection against mechanical stress, the total number of active fibres adds to 382. Each fibre has a projected diameter of 2.68 arcsec in the sky or 10.91 pc at the assumed distance of M33. The filling factor of the science packet is 60 per cent. The detector used was a thinned, blue enhanced, $2K \times 4K$ CCD (SITe ST002A) with 15 μm pixels (Kelz et al. 2006).

The centre of the galaxy and the external region IC 132 were observed between 2007 September 7 and September 9. The positions of the fields over an Hα image (Cheng et al. 1997) are shown in Fig. 1. Detailed identification is given in Fig. 2; the instrument FOV is overplotted on NOAO Science Archive images (Massey et al. 2006) taken with a 50 Å full width at half-maximum (FWHM) filter centred on Hα. The fields for the centre were overlaid by one fibre width.

Observations were performed at two different grating angles (GROT) with the 300 grooves mm$^{-1}$ (V300) grating. The value GROT = −75 was selected to cover from 3591 to 6996 Å (optical) with a dispersion of 3.4 Å pixel$^{-1}$, and GROT = −72 to cover from 6873 to 10 186 Å (near-IR) and a dispersion of 3.2 Å pixel$^{-1}$. In addition, high spectral resolution spectra were obtained using the V1200 grating at GROT = −55.5, covering from 6100 to 6650 Å with a dispersion of 0.64 Å pixel$^{-1}$. In all cases, the CCD was sampled in a $2 \times 2$ binning mode and the values quoted above are the effective ones after the resampling. A journal of observations are shown in Table 2. The stars BD +17° 4708 and BD +28° 4211 were observed for flux calibration in the optical and near-IR ranges, respectively. Various continuum illuminated and HeHgCs+ThAr lamp frames were acquired and interleaved as close as possible to the science observations to account for flexures in the telescope. Sky flats were acquired at the beginning of the night and biases at the end. For each object three dithered pointings were taken in order to

fully cover the instrument FOV. The positions are D1 = (0, 0), D2 = (1.56, 0.78) and D3 = (1.56, −0.78), where the displacements are in arcseconds relative to the initial position D1. The average seeing was 1.0 arcsec; higher values as well as the presence of clouds are indicated in the last column of Table 2. Half of the third night was lost due to weather which limited severely the observing time and neither bias nor sky frames were taken. In this case, the bias was determined from the overscan region of each frame.

### 2.3 Data reduction

The data reduction is based on the set of routines and tools grouped in the E3D (Sánchez 2004; Sánchez, Becker & Kelz 2004) and R3D (Sánchez & Cardiel 2005) packages. These were complemented with visualization and analysis tools developed by us, together with standard IRAF[2] utilities.

The pipeline includes spectra tracing, extraction, fibre flat correction, flux calibration, sky subtraction and data cube building. Once the 3D data cube was assembled, it was additionally corrected for differential atmospheric refraction, atmospheric correction for the [S III] near-IR lines and extinction. Details of the reduction can be found in García-Benito et al. (2010) and in the Complementary Online Material.

The final integrated spectra for the IC 132 region are shown in Fig. 3 with relevant lines identified in the optical and near-IR spectral ranges.

---

[2] IRAF is distributed by the National Optical Astronomy Observatory, which is operated by the Association of Universities for Research in Astronomy (AURA), Inc., under cooperative agreement with the National Science Foundation.

**Table 2.** Journal of observations.

| Object | Spectral range (Å) | Dispersion (Å pixel$^{-1}$) | Exposure time (s) | Median airmass | Notes |
|---|---|---|---|---|---|
| Centre P1 D1 | 3591–6996 | 3.4 | 500 × 3 | | seeing ≃ 1.46 arcsec |
| Centre P1 D2 | 3591–6996 | 3.4 | 500 × 3 | 1.49 | seeing ≃ 1.43 arcsec |
| Centre P1 D3 | 3591–6996 | 3.4 | 500 × 3 | | |
| Centre P2 D1 | 3591–6996 | 3.4 | 500 × 3 | | |
| Centre P2 D2 | 3591–6996 | 3.4 | 500 × 3 | 1.01 | |
| Centre P2 D3 | 3591–6996 | 3.4 | 500 × 3 | | |
| IC 132 D1 | 3591–6996 | 3.4 | 500 × 3 | | |
| IC 132 D2 | 3591–6996 | 3.4 | 500 × 3 | 1.02 | |
| IC 132 D3 | 3591–6996 | 3.4 | 500 × 3 | | |
| Centre P1 D1 | 6873–10186 | 3.2 | 500 + 700 × 2 | | seeing ≃ 1.33 arcsec |
| Centre P1 D2 | 6873–10186 | 3.2 | 700 × 3 | 1.49 | |
| Centre P1 D3 | 6873–10186 | 3.2 | 700 × 3 | | |
| Centre P2 D1 | 6873–10186 | 3.2 | 700 × 3 | | |
| Centre P2 D2 | 6873–10186 | 3.2 | 700 × 3 | 1.04 | Clouded, seeing ≃ 1.48 arcsec |
| Centre P2 D3 | 6873–10186 | 3.2 | 700 × 3 | | |
| IC 132 D1 | 6873–10186 | 3.2 | 500 × 3 | | Clouded |
| IC 132 D2 | 6873–10186 | 3.2 | 500 × 3 | 1.07 | Clouded |
| IC 132 D3 | 6873–10186 | 3.2 | 500 × 3 | | Clouded |
| Centre P1 D1 | 6100–6650 | 0.64 | 500 × 3 | | |
| Centre P1 D2 | 6100–6650 | 0.64 | 500 × 3 | 1.19 | |
| Centre P1 D3 | 6100–6650 | 0.64 | 500 × 3 | | Guiding stopped momentarily |
| Centre P2 D1 | 6100–6650 | 0.64 | 500 × 3 | | |
| Centre P2 D2 | 6100–6650 | 0.64 | 500 × 3 | 1.01 | |
| Centre P2 D3 | 6100–6650 | 0.64 | 500 × 3 | | |
| IC 132 D1 | 6100–6650 | 0.64 | 500 × 3 | | Clouded, seeing 1.50 arcsec |
| IC 132 D2 | 6100–6650 | 0.64 | 500 × 3 | 1.04 | Clouded, seeing 1.40 arcsec |
| IC 132 D3 | 6100–6650 | 0.64 | 500 | | Clouded, seeing 1.60 arcsec |

*Notes.* (i) The median seeing was 1.0 arcsec; those pointings with seeing above 1.3 arcsec are indicated as well as other non-photometric conditions.
(ii) The median airmass is given for each of the three dithering positions. For the third night, no bias or sky flat frames were taken.
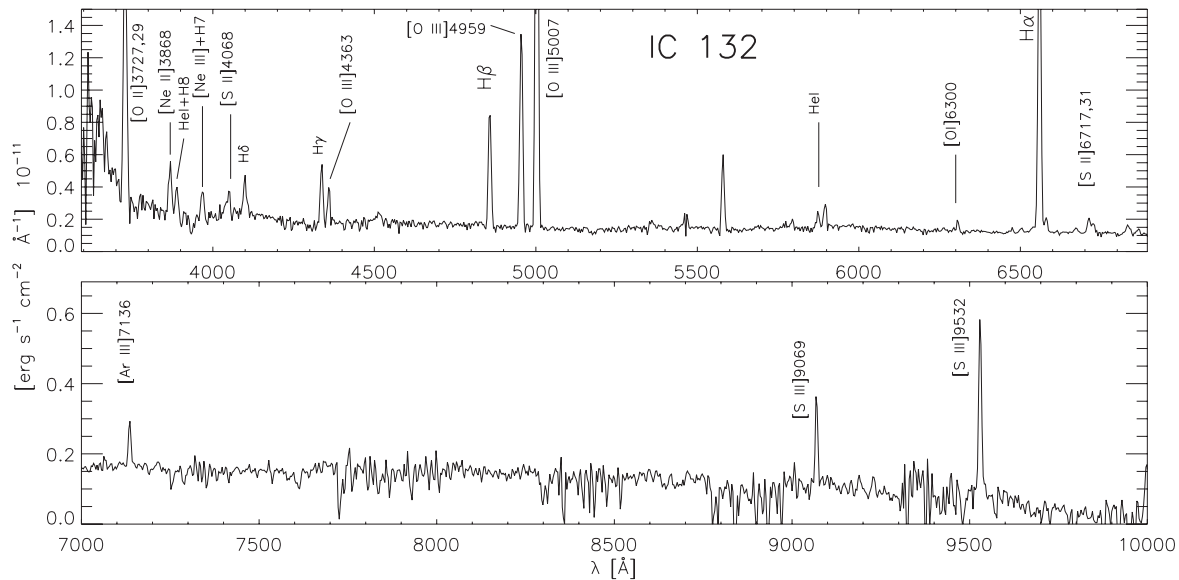


**Figure 3.** Integrated visual and near-IR spectra for IC 132. Relevant emission lines are identified. See text regarding special considerations for [O III] λ4363 Å and García-Benito et al. (2010) for the treatment of the near-IR [S III] lines.

## 2.4 Emission-line maps

Emission lines were fitted with a Gaussian, and continuum bands at both sides of the emission were measured additionally to estimate the error in the continuum placement. Given the low resolution of the data (FWHM effective resolution $R_{FWHM} \simeq 700$ at $\lambda = 5500$ Å and $R_{FWHM} \simeq 1100$ at $\lambda = 8500$ Å) for the first and second nights, some of the lines had to be deblended by fitting multiple Gaussians.
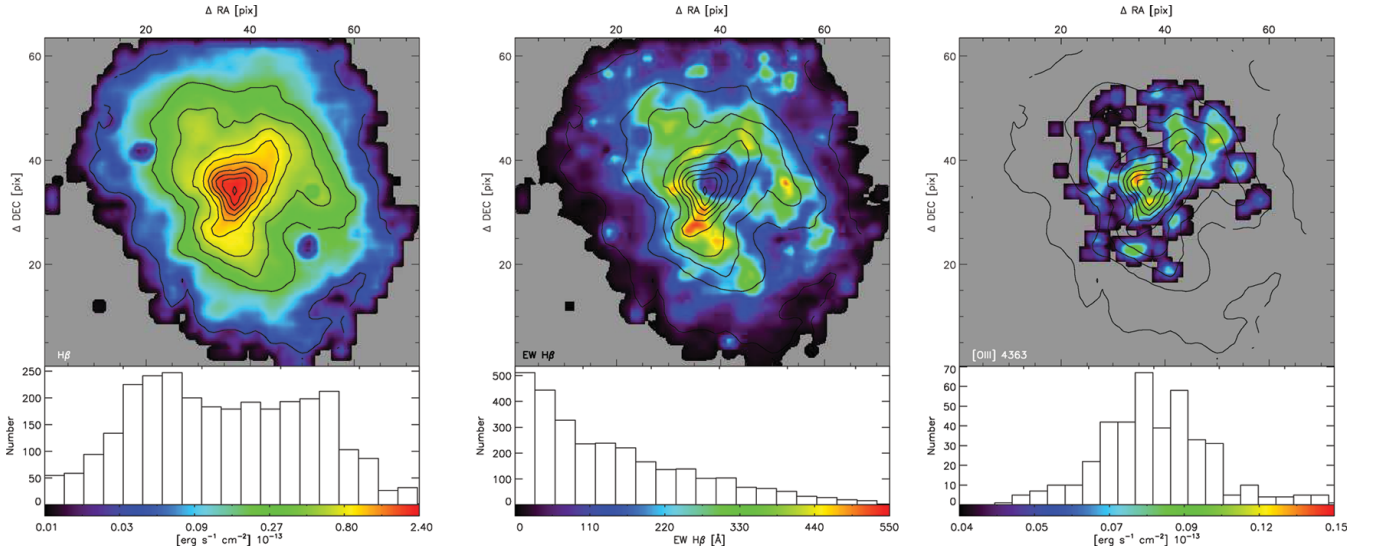
**Figure 4.** Example of maps for IC 132: Hβ, Hβ equivalent width [EW(Hβ)] and [O III] λ4363 Å with S/N > 2. The colour table has a logarithmic scale to increase the dynamical range. In this and all the other maps, the isocontours are from the Hα map.
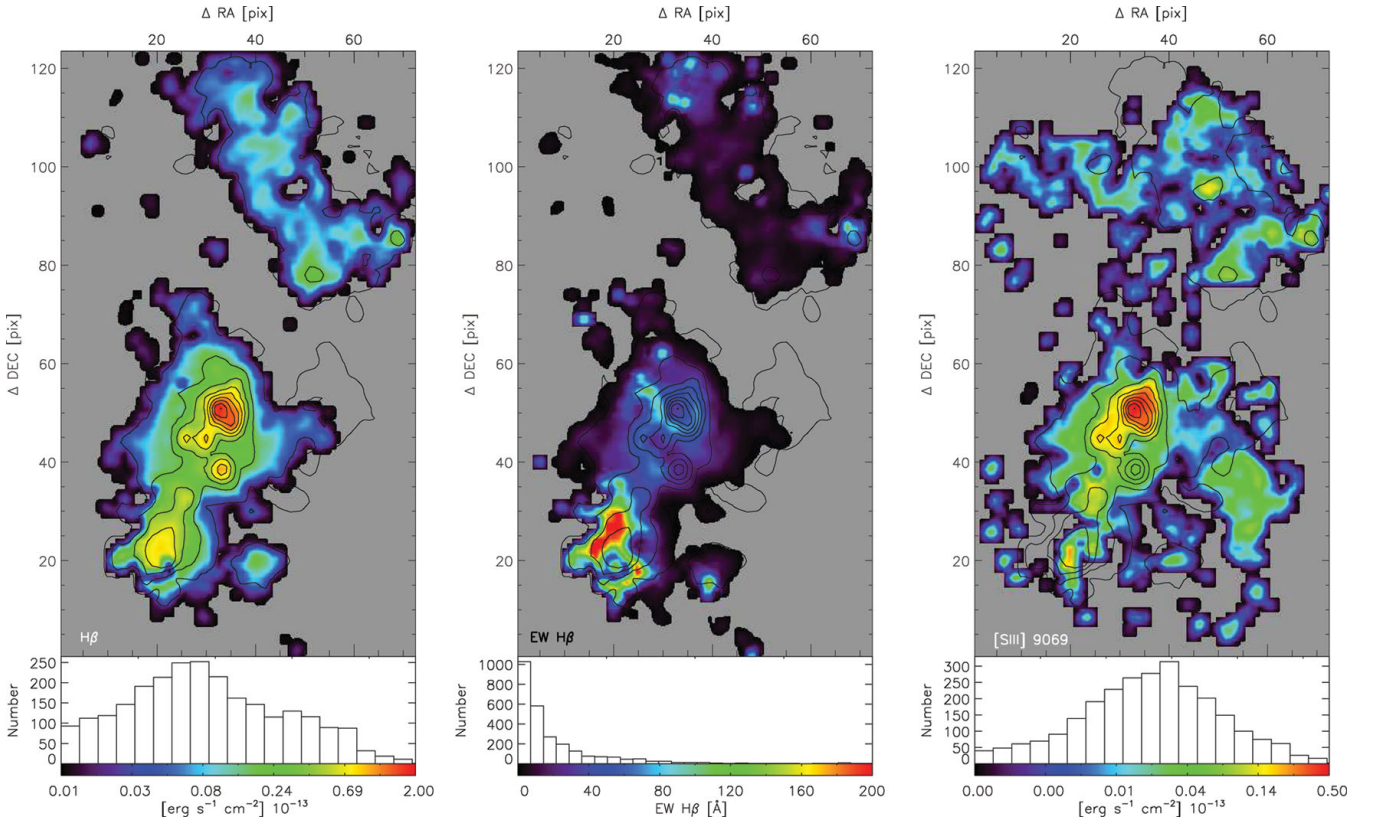


**Figure 5.** Example of maps for the central zone: Hβ, EW(Hβ) and [S III] λ9069 with S/N > 2. The colour table has a logarithmic scale to increase the dynamical range.

This was the case for the triple blend of Hα and the two [N II] lines at λλ6548,6584 Å and the [S II] λλ6717,6731 Å doublet. In each case a single Gaussian is assigned to each line and the best solution is determined using a non-linear least-squares fit. For the third night, the higher resolution ($R_{FWHM} \simeq 3100$ at $\lambda = 6500$ Å) allows the separation of the Hα–[N II] λλ6548,6584 Å system as well as the

measurement of the faint [S III] λ6312 line, at least for the brightest spatial resolution elements (spaxels) of IC 132.

Examples of 2D maps are shown in Fig. 4 for IC 132: $I$(Hβ), Hβ equivalent width [EW(Hβ)] and $I$([O III] λ4363), and in Fig. 5 for the central zone: $I$(Hβ), EW(Hβ) and $I$([S III] λ9069). The line maps have signal-to-noise ratio (S/N) > 2.0.
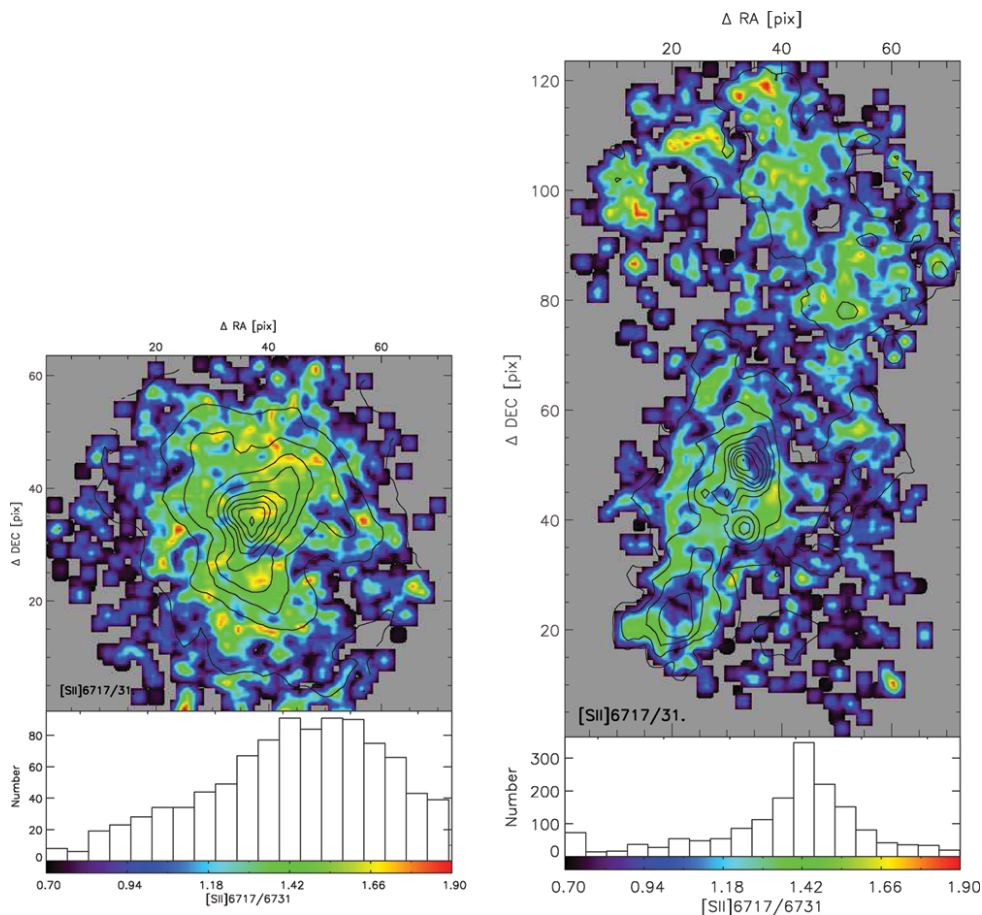
**Figure 6.** [S II] $\lambda 6717$/[S II] $\lambda 6731$ maps for IC 132 (left-hand panel) and for the central zone of M33 (right-hand panel). Notice the different vertical scale in the histograms.

## 3  PHYSICAL CONDITIONS OF THE GAS

Physical parameters describing the ionized gas were derived using the line fluxes measured in Section 2.4. To obtain these parameters, we used the TEMDEN routine included in the STSDAS nebular package for IRAF. This task solves the statistical equilibrium equation for the five-level atom approximation (Shaw & Dufour 1995). The transition probabilities have been updated with recent values computed for the [O II], [O III], [N II], [S II] and [S III] ions by Fischer & Tachiev (2004, 2006). The collision strength values were taken from Tayal (2007) for [O II], from Aggarwal & Keenan (1999) for [O III], from (Hudson & Bell 2005) for [N II], from Ramsbottom & Bell (1996) for [S II] and from Tayal & Gupta (1999) for [S III].

Computations were made for each individual spaxel where the required lines are detected with enough S/N and also for the shell analysis described in Section 7. The S/N > 5 requirement was met by the intense lines ([O III] $\lambda 5007$, H$\alpha$, H$\beta$) for all the spaxels, while for the auroral lines [O III] $\lambda 4363$ and [S III] $\lambda 6312$, S/N > 2 was reached only in the central part of IC 132.

The electron density ($n_e$) was estimated from the [S II] $\lambda 6717$/[S II] $\lambda 6731$ line ratio, and for the electron temperature ($T_e$) we used the faint auroral [O III] $\lambda 4363$ and [S III] $\lambda 6312$ lines, allowing the use of the [O III] $\lambda\lambda 4959,5007$/[O III] $\lambda 4363$ and [S III] $\lambda\lambda 9069,9532$/[S III] $\lambda 6312$ ratios to compute $T_e$([O III])

and $T_e$(S III), respectively. Due to strong atmospheric absorptions around 9300 Å, we defined the [S III] 9532 line by its theoretical ratio to the 9069 Å line.

### 3.1  Electron densities

To estimate $n_e$ we used the ratio $R_{S2} \equiv$ [S II] $\lambda 6717$/[S II] $\lambda 6731$ and the TEMDEN routine in IRAF (Shaw & Dufour 1995). Fig. 6 shows the $R_{S2}$ ratio for the external region IC 132 and for the centre of M33. For IC 132 the $R_{S2}$ distribution is quite uniform with a mean value around 1.45, and although the $R_{S2}$ ratio shows variations in the brightest parts, the conversion to $n_e$ would translate into variations within the low-density regime, which is of no significant impact in further parameter estimations.

The central region of M33 shows a broad distribution with the brightest H$\alpha$ region having $R_{S2}$ values around 1.4, indicating $n_e$ values also in the low-density regime, while the northern much fainter H$\alpha$ extension shows some spaxels with unrealistically large $R_{S2}$ ratios. From the $R_{S2}$ ratio, it seems that a structure exists and in such cases the hypothesis of a uniform value across the nebula would be too simplistic.

From the $n_e$ maps it is obvious that many pixels show an $R_{S2}$ ratio above the theoretical value for the low density limit and that it decreases down to the lower ratio limit, indicating that the region spans the whole range of $n_e$ from very high to very low densities.

There is positively some uncertainty from deblending the [S II] lines, and this is not exclusive of our data. Previous $R_{S2}$ determinations from IFS data also show ratios with significant excursions above the theoretical limit, from data obtained with the same instrument (Relaño et al. 2010; Monreal-Ibero et al. 2011) or other IFUs in a different telescope (Lagos et al. 2009), even with the [S II] lines resolved.

However, the problem does not seem to be exclusive of IFS data. From a literature compilation and their own observations, all obtained with long-slit spectroscopy, Kennicutt et al. (1989, fig. 5) report an $R_{S2}$ ratio peaked at 1.3 and with a significant number of H II regions, mainly in spiral discs, above the 1.4 theoretical limit. Also from long-slit spectra, Zaritsky et al. (1994, fig. 4) report a similar behaviour for $R_{S2}$.

When $R_{S2} \geq 1.4$ is obtained, it may be assumed that $n_e$ is below $10 \, \text{cm}^{-3}$; however, the assignment of a true density is very uncertain (it begins to be uncertain as $R_{S2}$ reaches the asymptotic limit even before 1.4). Although the safe way to proceed in such cases is to assume $n_e = 100 \, \text{cm}^{-3}$, (in any case for temperature and abundance determinations, the density plays a second-order role), and it seems that the theoretical ground for the determination of $n_e$ may need an adjustment to the atomic data and further investigation in the topic is required which is beyond the scope of this work.

This problem, which seems to be affecting both ends of the theoretical calibration, could be traced to uncertainties in the determination of the atomic data used, specifically the collision strengths for the low end and the transition probabilities for the high end, not only for [S II] but also for density indicators based on different line ratios (McLaughlin & Bell 1998; Copetti & Writzl 2002; Wang et al. 2004; Gary Ferland, private communication). We concur with Wang and collaborators that a full independent study with ad hoc data to validate previous results is crucial.

### 3.2 Electron temperatures

We have determined the $T_e([\text{O III}])$ and $T_e([\text{S III}])$ electron temperatures using the direct method based on the line ratios [O III] $\lambda\lambda 4959,5007/\lambda 4363$ and [S III] $\lambda\lambda 9069,9532/\lambda 6312$, respectively.

Only in the brightest parts of the core of IC 132 it was possible to derive reliable $T_e([\text{O III}])$ and $T_e([\text{S III}])$. Unfortunately, the sky at Calar Alto suffers from light pollution produced by street lamps, and among the several emissions in the visible range is the Hg I $\lambda 4358.3$ line, which is strong enough (Sánchez et al. 2007) to limit the use of the [O III] $\lambda 4363.2$ line in the temperature determination by the direct method in low-redshift systems. This is particularly bad for M33 because of its blueshifted spectrum ($z = -0.000\,597$) that brings the [O III] line to $\lambda = 4360.61$, close enough for it to blend with the Hg I line.

Nevertheless, by performing a careful sky subtraction, we were able to obtain upper limits for the [O III] $\lambda 4363$ line. This upper limit was used to compute an upper limit of $T_e([\text{O III}])$ and to estimate the ionization correction factor (ICF) for S. $T_e([\text{O III}])$ was computed using the ratio $R_{O3} = ([\text{O III}] \lambda 4959 + [\text{O III}] \lambda 5007)/[\text{O III}] \lambda 4363$ and the result is shown in Fig. 7 (top left-hand panel).

For $T_e([\text{O II}])$ we face the problem that while the [O II] $\lambda\lambda 3727,3729$ Å doublet was detected, the [O II] $\lambda 7320$ and $\lambda 7330$ lines were not. Thus, we have to relay on results from fits to photoionization models and their comparison with data with direct $T_e([\text{O II}])$ and $T_e([\text{O III}])$ determinations. Díaz et al. (2007) assume $T([\text{O II}]) \simeq T([\text{S III}])$, while Izotov et al. (2006), give expres-

sions to obtain $T([\text{O II}])$ from $T([\text{O III}])$ for the low, intermediate and high metallicity ranges. When possible, $T_e([\text{O II}])$ can be taken as $T_e([\text{N II}])$, however to estimate $T_e([\text{N II}])$, the weak [N II] $\lambda 5755$ line is required. In any case, alas, [N II] $\lambda 5755$ is not detected in our observations.

It seems that no strong correlation exists between the two temperatures in H II regions or in H II galaxies and that the effect of metallicity, density and maybe even other factors should be taken into account. Kennicutt, Bresolin & Garnett (2003) find only 'a hint of correlation', using their observations and data from the literature. Nevertheless, they use the Garnett (1992) expression to estimate $T([\text{O II}])$. Hägele et al. (2006, 2008) also show that the correlation between $T_e([\text{O II}])$ and $T_e([\text{O III}])$ is very weak and favours the use of the density-dependent Pérez-Montero & Díaz (2003) relation.

Here we apply the widely used relation from Garnett (1992) and the more recent fits from Pérez-Montero & Díaz (2003) to estimate $T_e([\text{O II}])$ from the upper limit of $T_e([\text{O III}])$. Fig. 7 shows the results from both estimates in the top middle and right-hand panels. For $T_e([\text{O II}])_{\text{PM03}}$ $n_e = 100$ was used for the whole region.

The electron temperature determined using the Garnett (1992) method gives a mean $T_e([\text{O II}])$ about 1600 K higher than Pérez-Montero & Díaz (2003). This difference may be traced to the fact that for $n_e = 100$ and $T_e([\text{O III}]) > 15\,000$, the Pérez-Montero & Díaz (2003) model is systematically below the Garnett (1992) relation. If $n_e = 10$ is assumed, then $T_e([\text{O II}])$ would increase by at least 2000 K, bringing the two methods to a better agreement.

The sulphur electron temperature $T_e([\text{S III}])$ was computed for spaxels where [S III] $\lambda 6312$ was detected with S/N > 2, using the ratio $R_{S23} = ([\text{S III}] \lambda 9069 + \lambda 9532)/[\text{S III}] \lambda 6312$. The intensity of [S III] $\lambda 9532$ was obtained from the theoretical relation [S III] $\lambda 9532 = 2.44 \times$ [S III] $\lambda 9069$, as the [S III] $\lambda 9532$ Å line is more affected in these spectra by telluric emissions and absorptions.

$T_e([\text{S III}])$ was also estimated using the fit obtained by (Hägele et al. 2006, hereafter H06) from a large set of observations that include H II galaxies, giant extragalactic H II regions and diffuse H II regions in the Galaxy and the Magellanic Clouds, given by $T_e([\text{S III}]) = 1.19 T_e([\text{O III}]) - 0.32$.

The set includes objects with $T_e([\text{S III}])$ up to 24 000 K. This not only extends the relation to higher temperatures, but also increases the uncertainty in the fit given that at the high temperature regime fewer objects exist and they exhibit large errors. In this case, we remark that $T_e([\text{O III}])$ is an upper limit and caution should be taken for its interpretation.

We also used the $SO_{23}$ parameter (Díaz & Pérez-Montero 2000; Díaz et al. 2007), defined as

$$SO_{23} = \frac{S_{23}}{O_{23}} = \frac{[\text{S II}] \, \lambda\lambda 6717, 6731 + [\text{S III}] \, \lambda\lambda 9069, 9532}{[\text{O II}] \, \lambda\lambda 3727, 3729 + [\text{O III}] \, \lambda\lambda 4959, 5007} \quad (1)$$

which has weak dependence on the ionization parameter. $T_e$ is then obtained as $T_e([\text{S III}]) = 0.596 - 0.283(\log SO_{23}) + 0.199(\log SO_{23})^2$.

Although this calibration was obtained for high-metallicity objects and its use is justified for the central region, we also applied it for IC 132, given that the $SO_{23}$ values obtained are within the parameter validity range of the original fit.

Fig. 7 maps the distribution of $T_e([\text{S III}])$ computed using the H06 and $SO_{23}$ methods for IC 132. In the first case, the
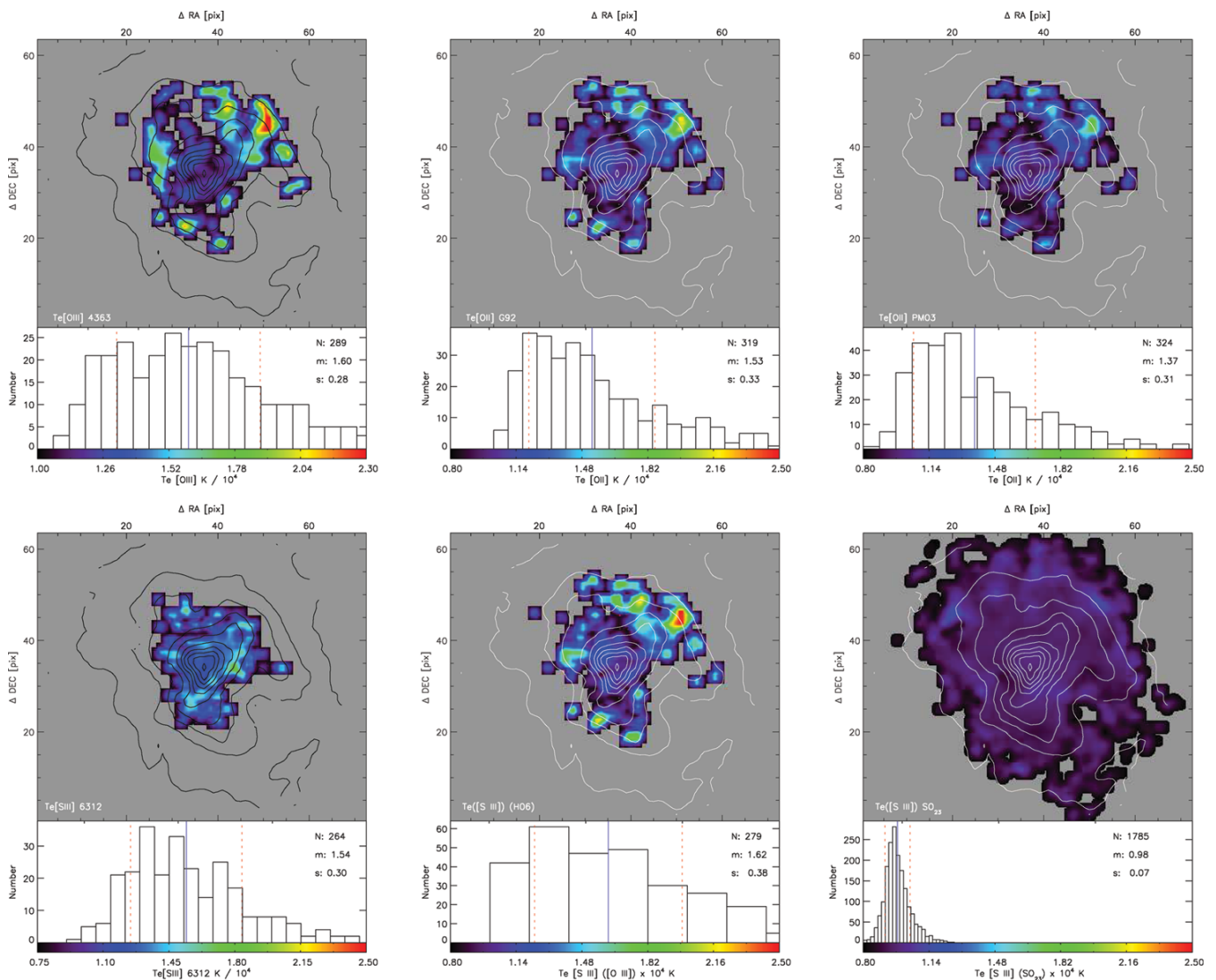
**Figure 7.** Top left-hand to right-hand side: $T_e$([O III]) upper limit for IC 132. $T_e$([O II]) estimated from the relations provided by (Garnett 1992) and (Pérez-Montero & Díaz 2003). Bottom left-hand to right-hand side: $T_e$([S III]) obtained from the direct method, using (Hägele et al. 2006) and (Díaz et al. 2007). Here and in the following figures, the histogram of the distribution also indicates the total number of pixels used ($N$), the mean ($m$, solid blue line) and the s.d. ($s$, red dashed lines).

dependency on $T_e$([O III]) and consequently on [O III] $\lambda4363$ is reflected in the facts that only the area where [O III] is detected with S/N > 2 has $T_e$([S III]) and that these values are higher than the ones obtained with the other methods, being $T_e$([O III]) an upper limit.

Besides the fact that SO$_{23}$ has low sensitivity to the ionization parameter, the difference in scatter may also be traced to the difference in errors associated with the lines used. For the H06 method, the large error of the [O III] $\lambda4363$ line is propagated to give a standard deviation (s.d.) of about 3800 K in $T_e$([S III]), while for SO$_{23}$ all the involved lines having S/N > 10 give a standard deviation of just 700 K in $T_e$([S III]). The low mean $T_e$([S III]) = 9800 may have its root in the fact that the SO$_{23}$ calibration was obtained mainly with high-metallicity objects.

Fig. 8 shows the temperature distribution for the central region of M33 using the SO$_{23}$ method. It also gives a very uniform temperature for all the measured spaxels in the field.

If the scatter in temperature can be mainly associated with the ionization structure and SO$_{23}$ effectively cancels it, then it would be

worth to investigate the inclusion of more low-metallicity objects in the $T_e$([S III]) SO$_{23}$ fit. This may modify the relation to produce higher temperatures in the low-metallicity range [see fig. 9 of Díaz et al. 2007].

## 4 CHEMICAL ABUNDANCES

### 4.1 Direct method

#### 4.1.1 Oxygen

Taking the upper limit temperatures obtained for the central zone of IC 132, we computed the lower limit ionic abundances using the IONIC task from the NEBULAR package for IRAF, also based on the five-level atom statistical equilibrium approximation (De Robertis et al. 1987). This task requires additionally the electron density $n_e$ and the emission-line flux relative to H$\beta$ of an atom in specific ionization stages. For O$^{++}$/H$^+$ we used the upper limit $T_e$([O III]), while for O$^+$/H$^+$ we adopted the $T_e$([O II]) obtained from
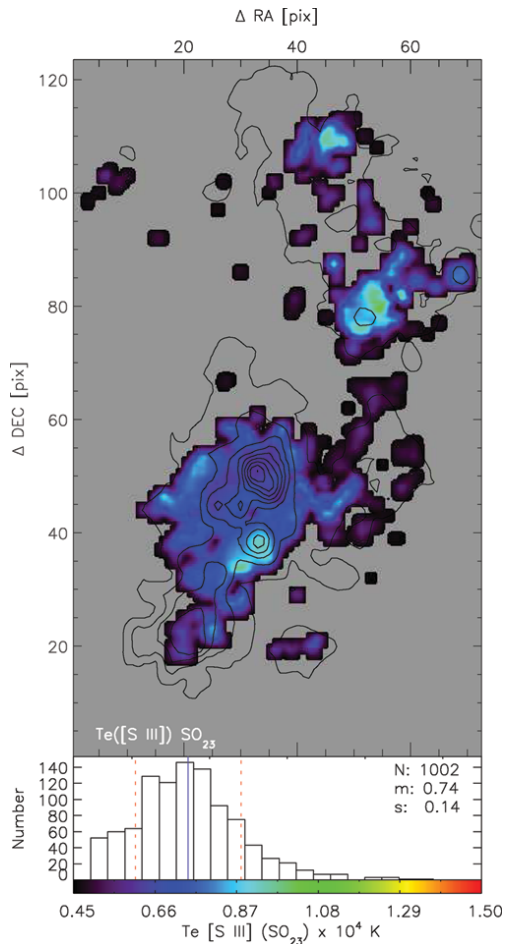
**Figure 8.** $T_e$([S III]) obtained as in (Díaz et al. 2007) for the centre of M33.

the relations given by Pérez-Montero & Díaz (2003). The total oxygen abundance was obtained as

$$\frac{O}{H} = \frac{O^+}{H^+} + \frac{O^{++}}{H^+} \qquad (2)$$

and is displayed, together with the ionic values, in the top panels of Fig. 9.

### 4.1.2 Sulphur

Sulphur ionic abundances were obtained using the expressions derived by (Díaz et al. 2007) from fits to results from the IONIC task. The unobserved $S^{3+}$ can represent an important contribution in high-ionization zones; thus, in order to estimate the total sulphur abundance, an ICF must be included. We used the ICF from (Barker 1980). Although $O^+$ and $O^{++}$ are lower limits, their inclusion in the sulphur ICF yields a better S estimation than just ignoring the correction factor.

The bottom panels of Fig. 9 shows the ionic and total sulphur abundances for IC 132. For the central region, the corresponding maps are in Fig. 10. The spatial distribution in IC 132 seems to have a wider dynamical range than the central zone in $S^+$ and $S^{++}$. This variation is primarily produced by a diagonal zone in the lower left-hand corner of IC 132, which we call a 'wall' that could probably be attributed to a zone of diffuse radiation (see Fig. 16).

## 4.2 Empirical methods

The direct method is useful in a restricted range of abundances. For systems with oxygen abundance larger than $\sim 0.2(O/H)_\odot$, as the metallicity increases, so does the cooling by IR fine structure lines and the [O III] $\lambda 4363$ Å line becomes extremely weak, requiring high-S/N observations to be detected. [Kennicutt et al. (2003) estimate oxygen abundances $\sim 0.5(O/H)_\odot$ as the practical upper limit to detect [O III] $\lambda 4363$ Å.]

The difficulty of direct abundance estimation has led to the development of *empirical* or *strong line* methods amply used in the literature.

### 4.2.1 The $R_{23}$ parameter

The empirical parameter $R_{23}$ = ([O II] $\lambda\lambda 3727,29$ + [O III] $\lambda\lambda 4959,5007$)/H$\beta$, also known as $O_{23}$, was first proposed by (Pagel et al. 1979) and is widely used as an abundance indicator. Several calibrations exist for $R_{23}$, revised in light of new observations with direct $T_e$ determinations or improvements to photoionization models. Some reformulations of the parameter have also been produced in an effort to compensate for the effect of the stellar temperature and ionization parameter (Edmunds & Pagel 1984; Zaritsky, Kennicutt & Huchra 1994; Kobulnicky, Kennicutt & Pizagno 1999; Pilyugin 2001a,b).

$R_{23}$ has two main drawbacks. First is the fact that the metallicity mapping is double valued. For each value of $R_{23}$ there is a low metallicity value corresponding to the lower branch of the relation and a high metallicity estimate corresponding to the upper branch. Besides, the transition between branches depends on the calibration and is ill defined [see e.g. fig. 12 of Kennicutt et al. (2003)]. Secondly, most of the data points tend to lie close to the knee of the relation, i.e. in the region in which there is no dependence of the $R_{23}$ parameter on metallicity. The $R_{23}$ method is in practice a reliable abundance estimator only for the metal rich or very metal poor systems.

Here we used the calibration from McGaugh (1991), based on H II region photoionization models obtained with CLOUDY (Ferland et al. 1998) and taking into account the effect of the ionization parameter. The analytic expressions for the upper and lower branches are taken from Kobulnicky, Kennicutt & Pizagno (1999). The estimated uncertainty for this calibration ranges from 0.1 to 0.2 dex when the lines are detected with S/N > 8, reaching up to ±0.25 dex in the turnover zone around $12 + \log (O/H) \sim 8.4$.

To break the $R_{23}$ degeneracy, the [N II] $\lambda 6584$/[O II] $\lambda 3727$ ratio is used as an initial guess of metallicity helping in the selection of the appropriate $R_{23}$ branch (McCall, Rybski & Shields 1985). This ratio shows a weak dependence on the ionization parameter and a strong correlation with metallicity (Kewley & Dopita 2002). Another diagnostic ratio used to distinguish the proper $R_{23}$ branch is [N II] $\lambda 6584$/H$\alpha$ (Raimann et al. 2000), the N2 index, calibrated in [O/H] by Denicoló et al. (2002). However, this ratio has a strong dependence on the ionization parameter (see below).

Fig. 11 shows $R_{23}$ as a function of the [N II] $\lambda 6584$/[O II] $\lambda 3727$ ratio. The Kewley & Ellison (2008) empirical separation between the upper and lower branches of $R_{23}$ at [N II] $\lambda 6584$/[O II] $\lambda 3727$ = $-1.2$ [$12 + \log (O/H) \sim 8.4$] is used. For IC 132 the majority of the pixels fall within the lower branch regime, while for the central zone the opposite is observed. The central region seems to follow a continuous distribution of $R_{23}$, while in IC 132 most
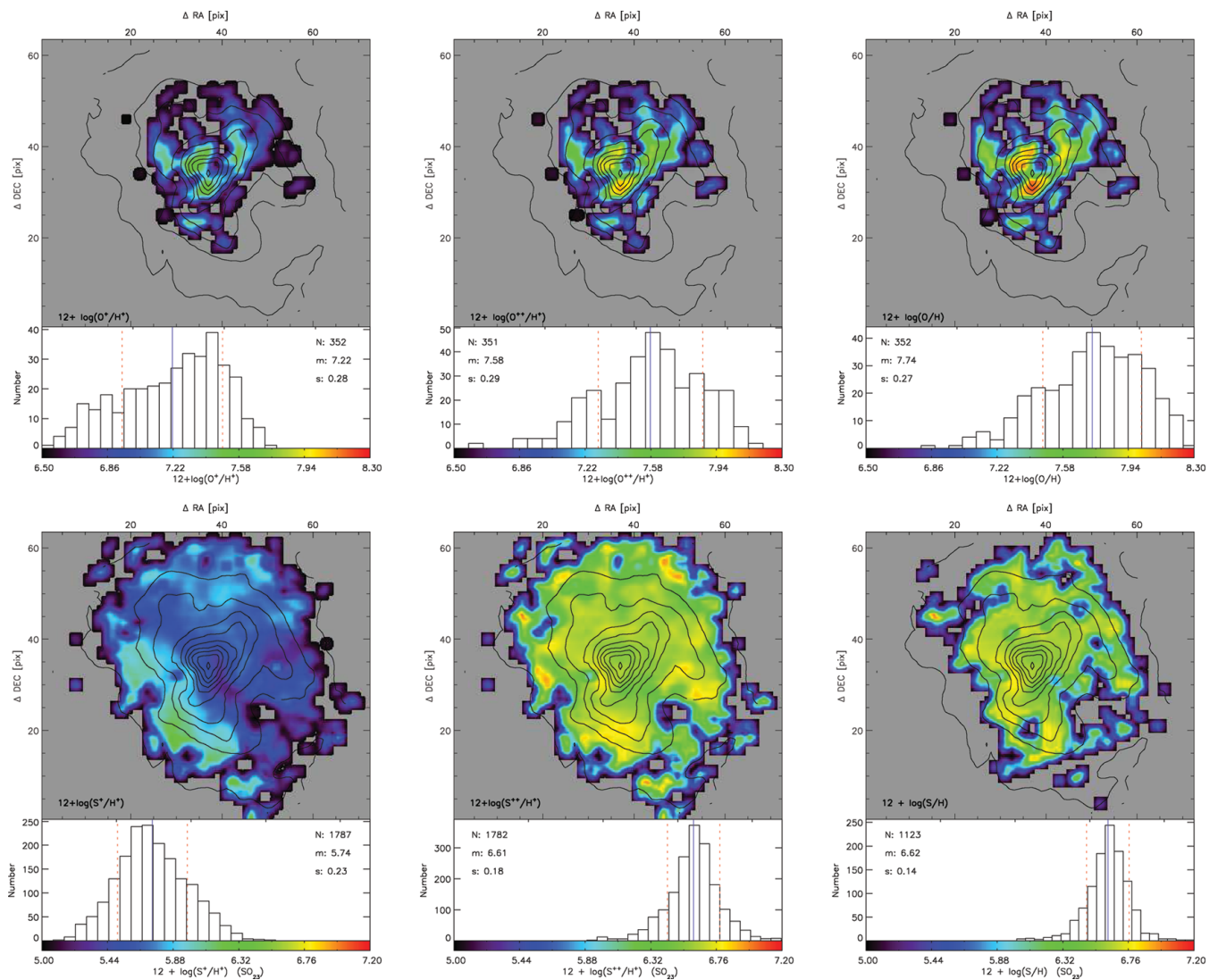
**Figure 9.** IC 132 ionic and total lower limit abundances for oxygen (top panels) and sulphur (bottom panels).

of the points are clustered between $\log(R_{23}) \sim -1.2$ and $\sim 0.8$ and the distribution shows a particularly abrupt cut-off at $\log(R_{23}) \sim 0.8$.

The empirical division by Kewley & Dopita (2002) was obtained combining observations and photoionization model grids. These models show a dispersion below [N II] $\lambda 6584$/[O II] $\lambda 3727 = 1.2$ for different values of ionization parameters and metallicities [see fig. 8 from Kewley & Dopita (2002)]. However, the correlation is remarkably extended up to $\log(R_{23}) > 1.6$ for the centre. This tail is produced by the faint (diffuse) radiation, not included in Kewley & Ellison (2008) models.

The resulting maps for the $R_{23}$ estimator are shown in the left-hand panels of Fig. 12 for IC 132 and Fig. 13 for the centre of M33.

Another empirical indicator based on the $R_{23}$ method is proposed by (Pilyugin 2001a,b,c) where the excitation parameter $P$ is introduced to compensate for $R_{23}$ variations along the region produced by differences in the ionization parameter. The upper branch applies to $12 + \log(O/H) > 8.2$ and the lower branch to $12 + \log(O/H) < 8.2$. Results from a spaxel-by-spaxel estimation are shown in Figs 12

and 13 for IC 132 and the centre, respectively. In this case, we used the [N II] $\lambda 6584$/[O II] $\lambda 3727$ ratio to select the branch and break the $R_{23}$ degeneracy.

*4.2.2 The N2 parameter*

The N2 index, defined by Denicoló et al. (2002) as N2 = [N II] $\lambda 6584$/H$\alpha$, was previously used by Storchi-Bergmann, Calzetti & Kinney (1994) as an empirical abundance estimator for star-forming galaxies. Its usefulness is based on the fact that it is easy to observe up to relatively high redshifts and, due to the closeness of the lines involved, it is unaffected by reddening and can even be measured directly from uncalibrated spectra. Here we use the N2 fit from Denicoló et al. (2002), given as $12 + \log(O/H) = 9.12 + 0.73 \, N2$. The resulting maps from the N2 estimator are shown in the lower panels of Fig. 12 for IC 132 and in Fig. 13 for the centre of M33.

It is remarkable that the abundance based on N2 shows practically no variation in the maps. One may conclude from this indicator that the oxygen abundance has one single value for the
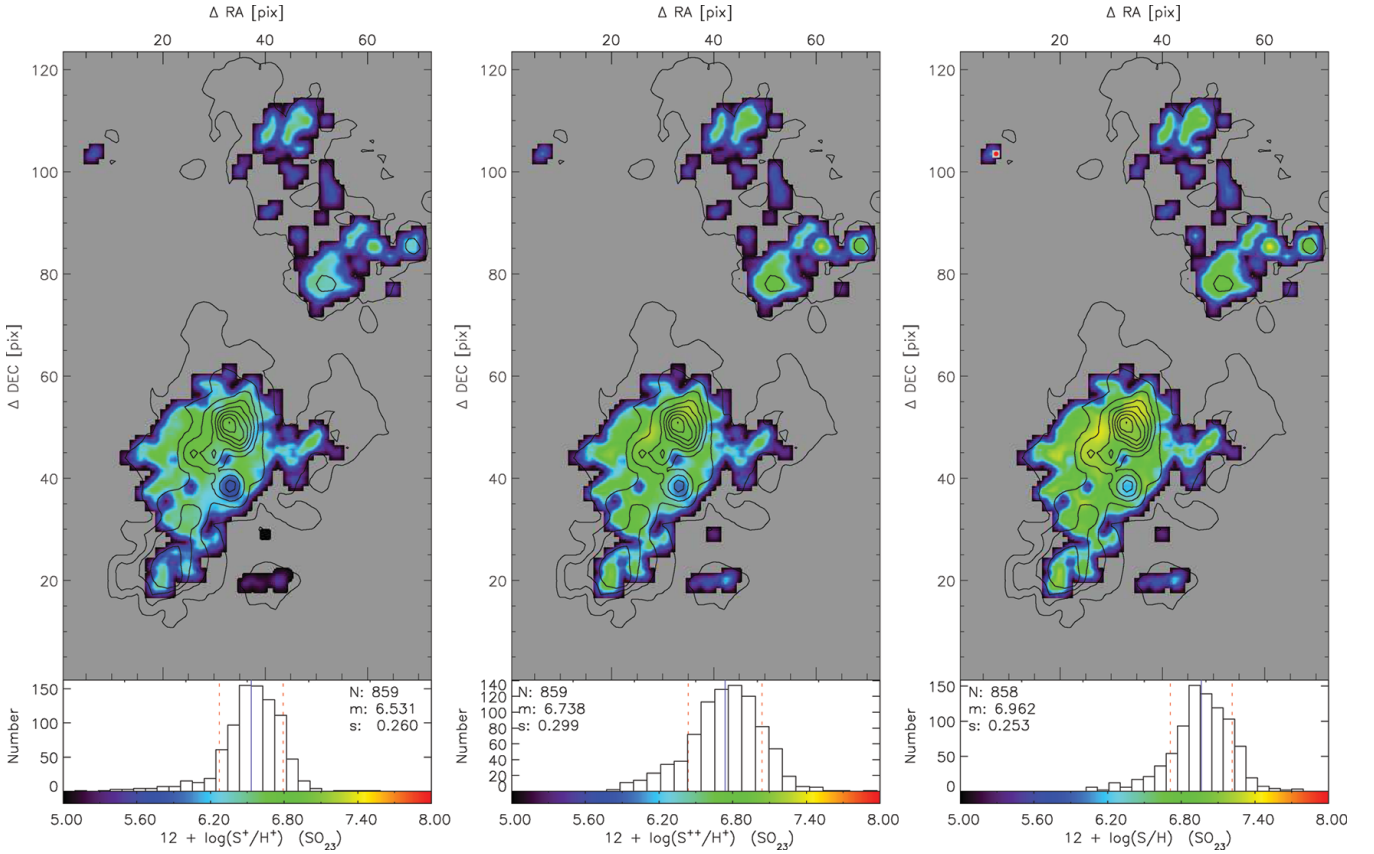
**Figure 10.** Ionic $(S^+/H^+)$ and $(S^{++}/H^+)$ and total sulphur abundances for the centre of M33.
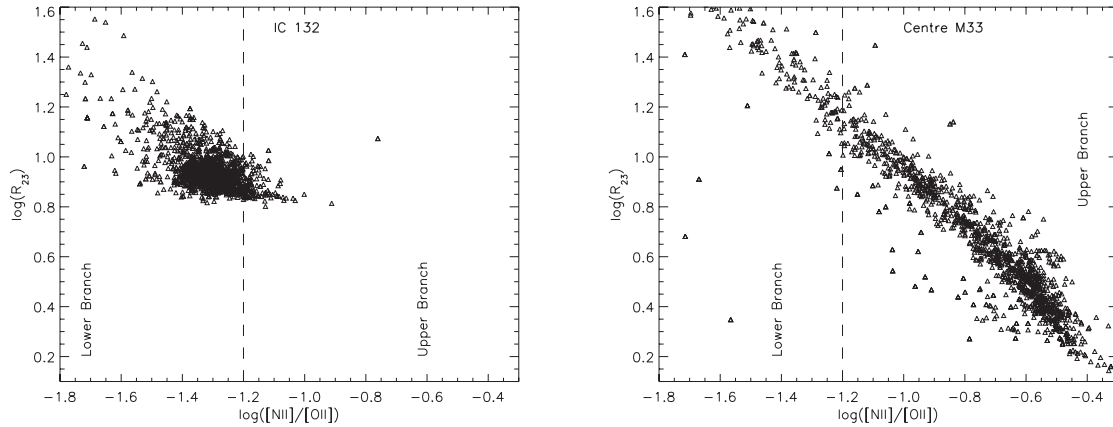


**Figure 11.** [N II]/[O II] versus $R_{23}$ to select the upper or lower branch for each pixel. Left-hand panel: IC 132; right-hand panel: central zone. The dividing dashed line is from (Kewley & Ellison 2008) calibration. Only those pixels with errors lower than 0.1 dex in each axis are plotted.

whole region. It seems that all the variations within the region can be traced to the error which effectively increases with radius both for IC 132 and for the bright central condensation, hereinafter called BCLMP 93, as identified in Boulesteix et al. (1974).

### 4.2.3 The O3N2 parameter

Pettini & Pagel (2004) calibrated the O3N2 ratio (Alloin et al. 1979) as an abundance estimator, giving the relation $12 + \log(O/H) = 8.73 - 0.32 \times O3N2$, where $O3N2 = \log([O \text{ III}] \lambda 5007/H\beta)/([N \text{ II}] \lambda 6584/H\alpha)$.

The resulting maps of $12 + \log(O/H)$ from the O3N2 estimator are shown in the right-hand panels of Fig. 12 for IC 132 and Fig. 13 for the centre of M33.

The distributions of O/H obtained via N2 and O3N2 are very similar; the scatter is smaller when the abundance is derived using O3N2 than when using N2 in IC 132.

### 4.2.4 The S23 parameter

The $S_{23}$ parameter, proposed by (Vílchez & Esteban 1996), which uses the strong [S II] and [S III] lines, in analogy to $R_{23}$, is defined as $S_{23} = ([S \text{ II}] \lambda\lambda 6717,6731 + [S \text{ III}] \lambda\lambda 9069,9532)/H\beta$.
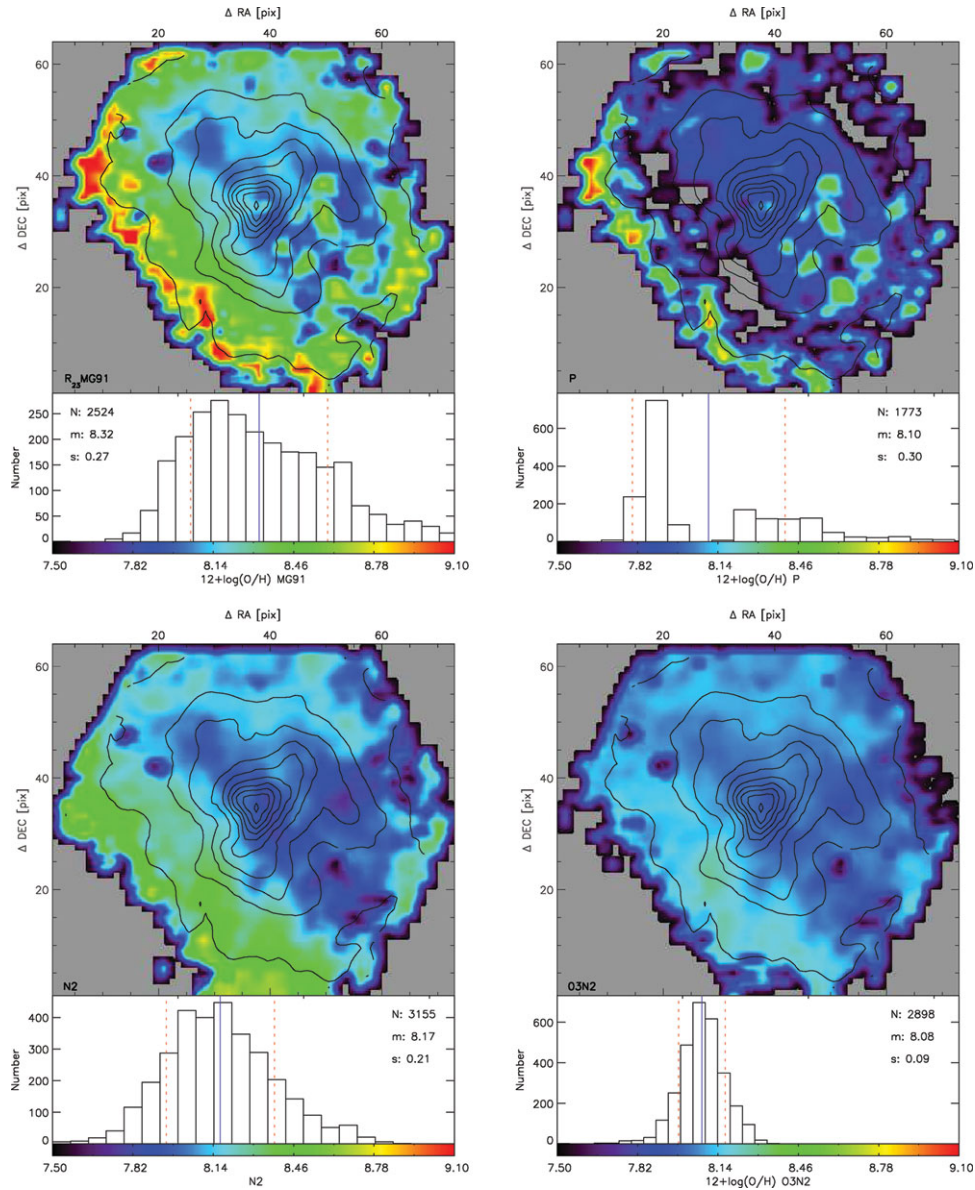
**Figure 12.** Empirical metallicity estimators for IC 132. Top panels: $R_{23}$ with the calibrations from (McGaugh 1991) and (Pilyugin 2001c). Bottom panels: N2 and O3N2.

Christensen et al. (1997) calibrated $S_{23}$ as a sulphur abundance indicator based on observational data compiled from the literature, while Díaz & Pérez-Montero (2000) proposed $S_{23}$ as an alternative to $R_{23}$ as an oxygen abundance indicator. $S_{23}$ presents some advantages over $R_{23}$: it is single valued up to solar metallicities and has less dependence on the ionization parameter and on the effective temperature of the ionizing stars. On the other hand, it needs wider spectral coverage to detect the near-IR [S III] lines and corrections for the unseen $S^{3+}$ ion.

We estimated the sulphur abundance (S/H) using the relation from Pérez-Montero et al. (2006), while for (O/H) we used the expression from Pérez-Montero & Díaz (2005). Both are fits obtained from observed data sets.

Sulphur and oxygen abundance maps obtained from the $S_{23}$ indicator are shown in Figs 14 and 15, respectively. The mean $12 + \log{(S/H)}_{S23}$ value for the central region is 7.02 with a s.d. of 0.34, while for IC 132 it is 9.5 with a smaller s.d. of 0.28. The estimates

of S/H and O/H for IC 132 using $S_{23}$ show little scatter, albeit slightly larger than that for the O/H abundance using the N2 or O3N2 estimators.

### 4.2.5 $Ar_3O_3$ and $S_3O_3$ calibrations

Based on a compilation of H II regions in spiral galaxies and blue compact galaxies, (Stasińska 2006) proposed the use of two line ratios ($Ar_3O_3 \equiv$ [Ar III] $\lambda 7135$/[O II] $\lambda 5007$ and $S_3O_3 \equiv$ [S III] $\lambda 9069$/[O III] $\lambda 5007$) as metallicity indicators. The calibration of the relation is based on the Pilyugin (2001a) method. In Section 7 we will analyse the results separating the data in sections of equal H$\alpha$ intensity in a treatment that we call individual shell segmentation. The respective line ratios for the individual shell segmentation are given in Tables 5 and 7 for IC 132 and in Tables 9 and 11 for BCLMP 93. The $12 + \log{(O/H)}$ values, also for shell
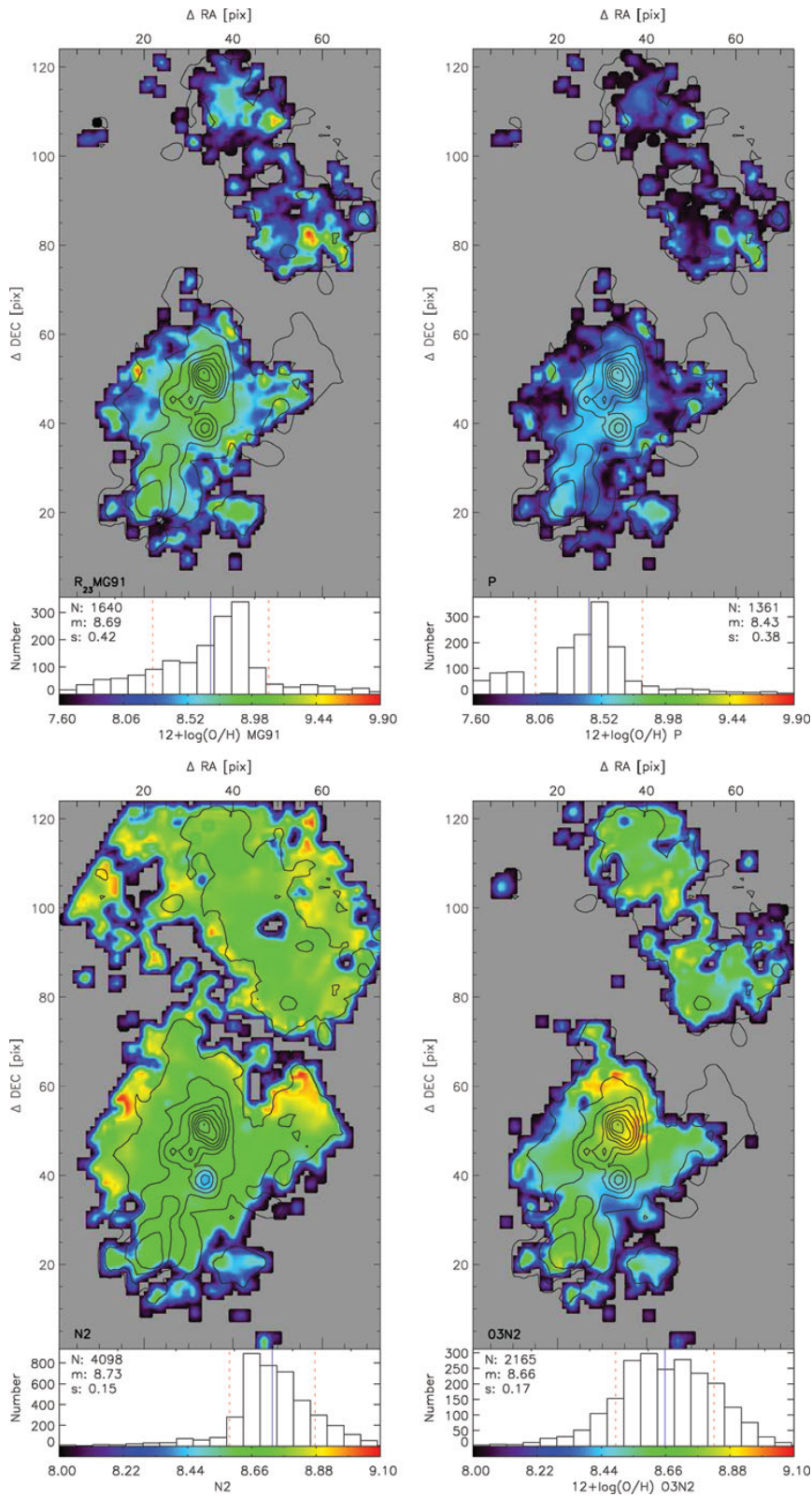
**Figure 13.** Empirical metallicity estimators for the centre of M33. Top panels: $R_{23}$ with the calibrations from (McGaugh 1991) and (Pilyugin 2001c). Bottom panels: N2 and O3N2.
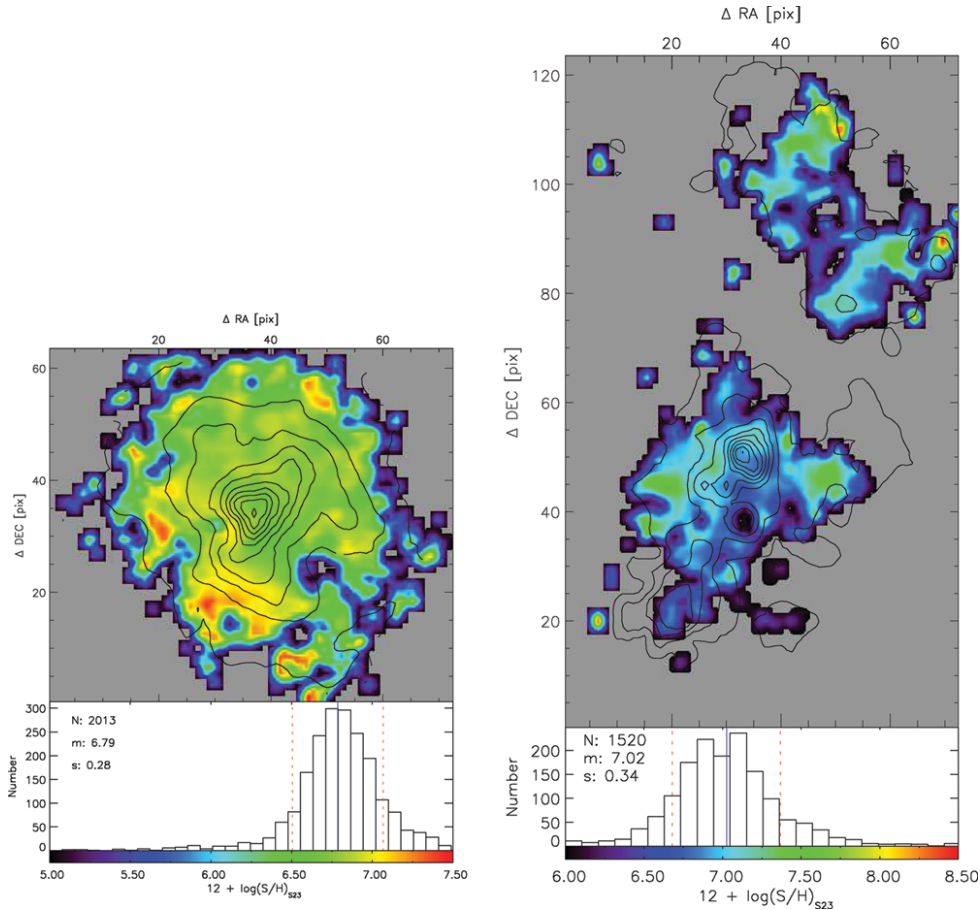
**Figure 14.** $12 + \log(S/H)$ abundance using the $S_{23}$ indicator for IC 132 (left-hand panel) and for the centre of M33 (right-hand panel).

segmentation, are shown in Figs 26 and 34 for IC 132 and BCLMP 93, respectively.

### 4.2.6 About the abundance estimations

The spatially resolved data on the M33 H II regions allow the comparison of the different estimators on the assumption that the metal content of the ionized gas is well mixed giving a uniform total abundance across the H II region. For IC 132, $R_{23}$ gives an average $12 + \log(O/H) = 8.32$ with s.d. $= 0.27$, the $P$ method gives $12 + \log(O/H) = 8.1$ with s.d. $= 0.30$, the N2 method gives an average $12 + \log(O/H) = 8.17$ with s.d. $= 0.27$ and O3N2 gives $12 + \log(O/H) = 8.08$ with s.d. $= 0.09$.

Hence, considering the mean of the abundance distribution we may say that the different indicators are consistent with each other in the sense that they give the same mean abundance value. Caution should arise for applying the $P$ method to IC 132, given that the mean of the abundance distribution falls between the two branches and the turnaround region is not formally defined by the method.

The results for the central H II regions are equally in agreement for the mean abundance, but with a larger scatter in the three estimators. $R_{23}$ gives an average $12 + \log(O/H) = 8.69$ with s.d. $= 0.42$ and $P$ gives $12 + \log(O/H) = 8.43$ with s.d. $= 0.38$. The N2 method gives an average $12 + \log(O/H) = 8.73$ with s.d. $= 0.15$ and O3N2 gives $12 + \log(O/H) = 8.66$ with s.d. $= 0.17$.

When the whole of the distribution is considered, then the agreement between indicators seems to hold only for the brightest parts of the region and breaks badly for the spaxels at the borders, especially for the $R_{23}$ and $P$ methods. The uniform abundance assumption is strongly supported by O3N2 and N2, making these methods the preferred ones for abundance estimation for our data.

The $P$ method for IC 132 is actually producing two separate distributions because the low- and high-abundance branches are selected for the same region. This is also the case for $R_{23}$. If $R_{23}$ is restricted to only one branch, the abundance would be more uniform. This brings up the question about the validity of applying a branch selection for each spaxel, maybe in this case the selection by the [N II]/[O II] criterion only applies to the integrated region. Another point to consider about empirical indicators is their sensitivity to the ionization parameter. From the maps it seems that O3N2 gives low dispersion because it can effectively cancel out this effect. On the other hand, $R_{23}$ shows high values especially in the lower left-hand corner of IC 132 where we suspect that the diffuse ionized gas is dominant. The validity of applying $R_{23}$ in such conditions is questioned.

Similar results are found for the sulphur abundance. Using the $S_{23}$ we find for IC 132 a sulphur abundance of $12 + \log(S/H) = 6.79$ with s.d. $= 0.28$ and for the central H II regions $12 + \log(S/H) = 7.02$ with s.d. $= 0.34$.

Regarding oxygen abundance, $S_{23}$ also shows a relatively small scatter albeit higher than that of the oxygen abundance estimates using N2 and O3N2.

When comparing direct abundance estimated with strong line methods, and using global measurements, i.e. including the whole of the H II regions, Kennicutt et al. (2003) found that $(O/H)_{R_{23}}$ is always higher than $(O/H)_{T_e}$, while the $(O/H)_{S_{23}}$ method gives results
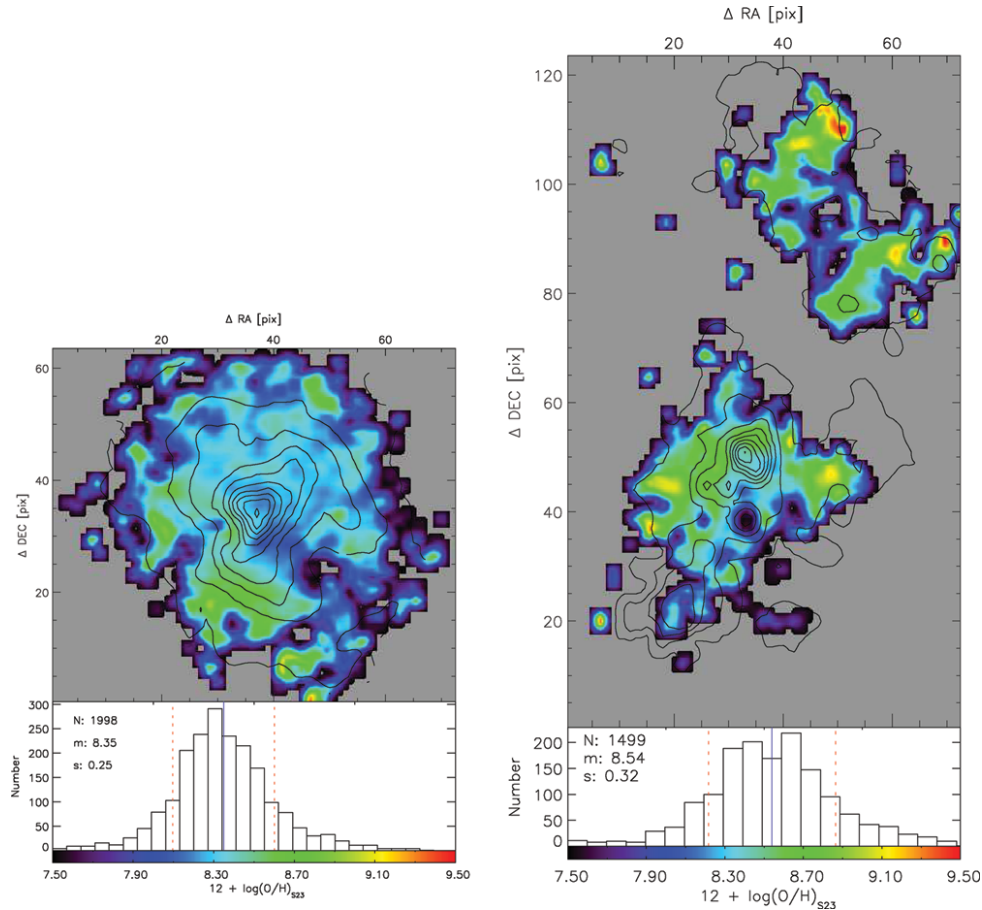
**Figure 15.** $12 + \log(\mathrm{O/H})$ abundance from the $S_{23}$ indicator for IC 132 (left-hand panel) and for the centre of M33 (right-hand panel).

in agreement with $(\mathrm{O/H})_{T_e}$ except for objects with high abundance values $[12 + \log(\mathrm{O/H})_{T_e} > 8.5]$, where $(\mathrm{O/H})_{S_{23}}$ is also larger than $(\mathrm{O/H})_{T_e}$. Stasińska (2002) noted this systematic overestimates by strong line methods, pointing out as possible causes the few number of objects with high quality $T_e$ determination and offsets between the temperatures assumed in the photoionization models and the temperatures observed.

For N2, comparing the Denicoló et al. (2002) calibration with direct $(\mathrm{O/H})$ determinations Pérez-Montero & Díaz (2005) found that $(\mathrm{O/H})_{N2}$ overestimates abundances for low-metallicity objects and underestimates them at high metallicity with a turnover at around $12 + \log(\mathrm{O/H})_{T_e} \sim 8.0$.

The selection of the empirical abundance indicator to use is primarily dictated by the available lines and their S/N; however, in our case various indicators are available that produce considerable differences between the estimated abundances. The question of what empirical indicator can be trusted is not a simple one to answer. As the $(\mathrm{O/H})$ calibrations are based on a set of objects with oxygen abundance derived with the $T_e$ method, the reliability of the relation depends on the quality, homogeneity and distribution of the reference objects. Ideally, to construct an empirical estimator the reference sample should cover all the abundance range; in practice, the reference is generally weighted towards low- or high-abundance objects and with gaps at certain abundances. This situation is partially alleviated by the use of photoionization models; nevertheless, its validity at different metallicities depends on our knowledge of transitional probabilities and collisional strengths for the different species.
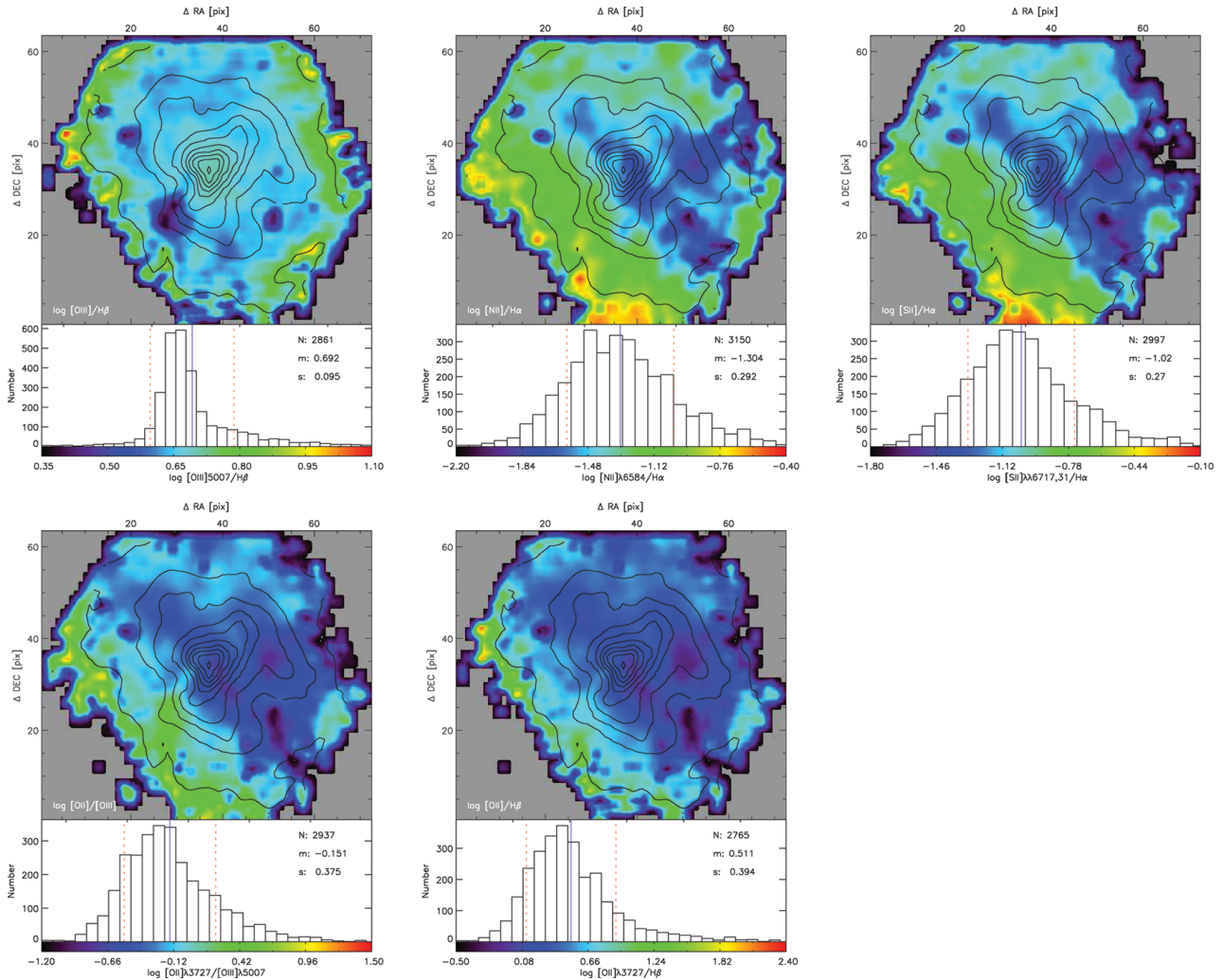
A warning may be raised about the use of empirical estimators for individual spaxels, given that the methodology was developed for global observations. The comparison of the empirical abundance maps with the integrated zones shows in general good statistical agreement, and this may indicate that the estimators can be used for spatially resolved observations, some with more confidence (O3N2,N2) than others ($R_{23}$, $P$). Nevertheless, determining the range of physical conditions where each empirical method is valid requires further investigation.

## 5 DIAGNOSTIC DIAGRAMS IN 2D

When interpreting emission-line spectra, it is important to be able to distinguish emission produced by star-forming regions from other sources such as planetary nebulae, supernova remnants or even an AGN. The conventional means for quantitatively classifying emission-line objects and distinguishing between gas ionized by stars or by non-thermal processes are diagnostic diagrams, such as BPT diagrams (Baldwin, Phillips & Terlevich 1981; Veilleux & Osterbrock 1987), involving the ratios of the strongest emission lines in the optical spectra. This traditional approach involves the comparison of the integrated emission-line ratios with global photoionization models, leaving open the question of the validity of using these diagnostic diagrams with spatially resolved spectroscopic data.

To search for systematic differences between the inner and outer H II regions as well as detecting regions with line ratios indicative of non-stellar ionization, we computed the $[\mathrm{O\,III}]\lambda5007/\mathrm{H}\beta$,

**Figure 16.** Top panels: IC 132 maps of the diagnostic line ratios [O III] λ5007/Hβ, [N II] λ6584/Hα and [S II] λλ 6717,31/Hα. Bottom panels: [O II] λ3727/[O III] λ5007 and [O II] λ3727/Hβ.

[N II] λ6584/Hα, [S II] λ6717+λ6731/Hα, [O II] λ3727/[O III] λ5007 and [O II] λ3727/Hβ line ratios, both spaxel by spaxel and the integrated values, to produce the distribution maps and investigate the emission-line diagnostic diagrams and the excitation structure within the regions.

Given the large ionization potential of [O III] (54.9 eV), the [O III] λ5007/Hβ ratio traces highly ionized gas, and grows directly proportional to the degree of ionization. On the other hand, because of the smaller ionization potential of both [N II] and [S II] (29.6 and 23.4 eV, respectively), their line intensities trace the low-ionization zones. These line ratio maps are shown in Fig. 16 for IC 132 and in Figs 17 and 18 for the central regions. For IC 132 the 'wall' in the lower left-hand part is present in most of the plots and is the strongest zone in the low-ionization indicator maps ([N II] λ6584/Hα, [S II] λ6717+λ6731/Hα), pointing to the existence of diffuse ionized gas in this area.

The Hα emission, being a tracer of star formation, can be expected to be spatially related to the position of the ionizing stars (this is true also for the highly ionized gas). Although the gas density and kinematics may play a role, in a first-order approximation the maxima of Hα emission should follow the high-ionization zones in the ionization ratio maps. From the [O III]/Hβ ratio maps, it is possible to see that this is true for the brightest part of IC 132 but

not for the H II regions in the central regions of M33. In particular, the behaviour of the region BCLMP 93 is just the opposite – the brightest Hα peak coincides with a low-ionization region and is partially surrounded by higher ionization gas.

Diagnostic BPT diagrams were created from the ionization and excitation sensitive line ratio maps shown before. In Fig. 19, the [N II] λ6584/Hα versus[O III] λ5007/Hβ BPT diagrams are shown. The individual spaxels are plotted in the diagrams, coloured according to the Hα intensity, and the inset shows the map for reference. Boundary starburst model lines are shown as follows: the solid line is from Kewley & Dopita (2002), the dotted line is from Kauffmann et al. (2003) and the dashed line is from Stasińska et al. (2006). The location of the integrated spectra is indicated in the black and white concentric circles.

The main and obvious result from an inspection of Fig. 19 is that there is an almost complete dichotomy in the distribution of points between the central and outer H II regions. While most of the line ratios of the central region are vertically distributed on the right-hand side of the diagram, all of the points from IC 132 are located horizontally in the upper left-hand part of the diagram. The regions occupied by the distributions have hardly any superposition; in fact, they are perpendicular to each other, but in both regions there are spaxels that clearly move away from the H II region zone of the
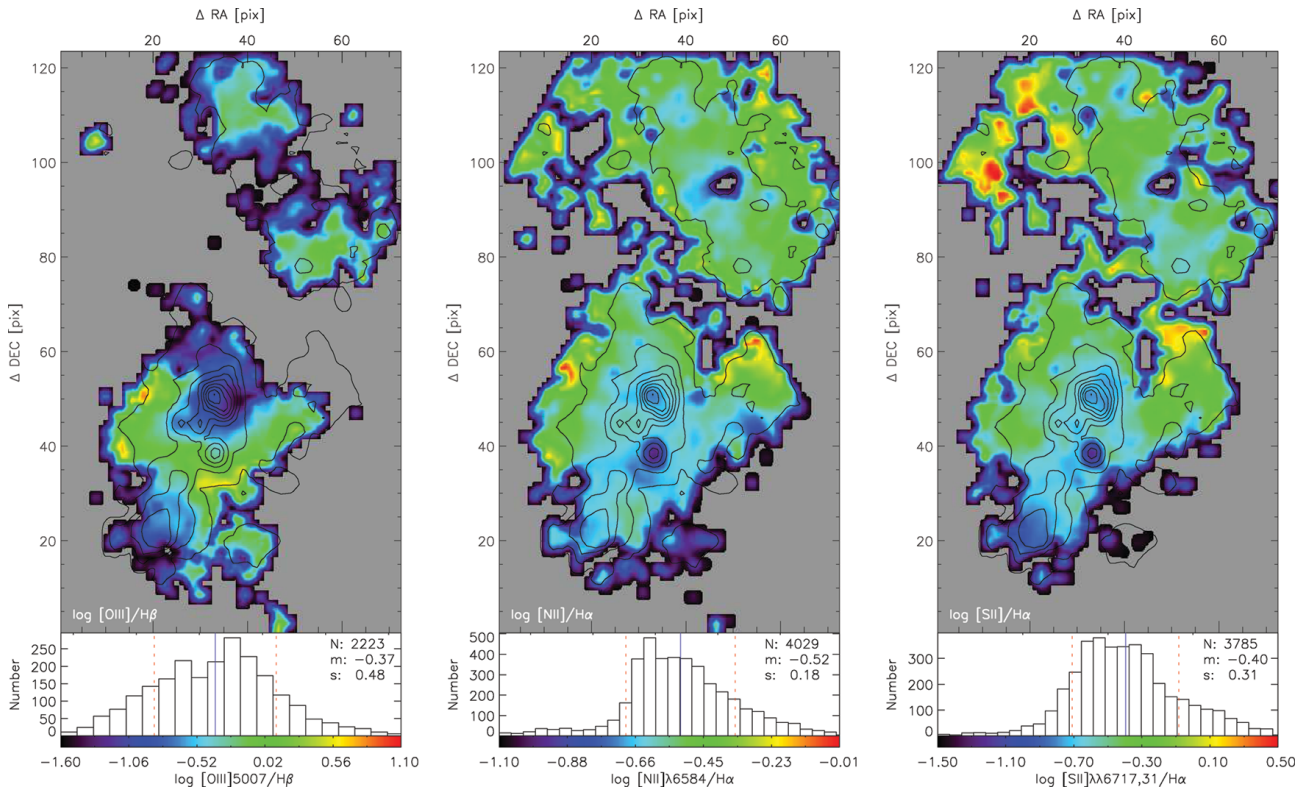
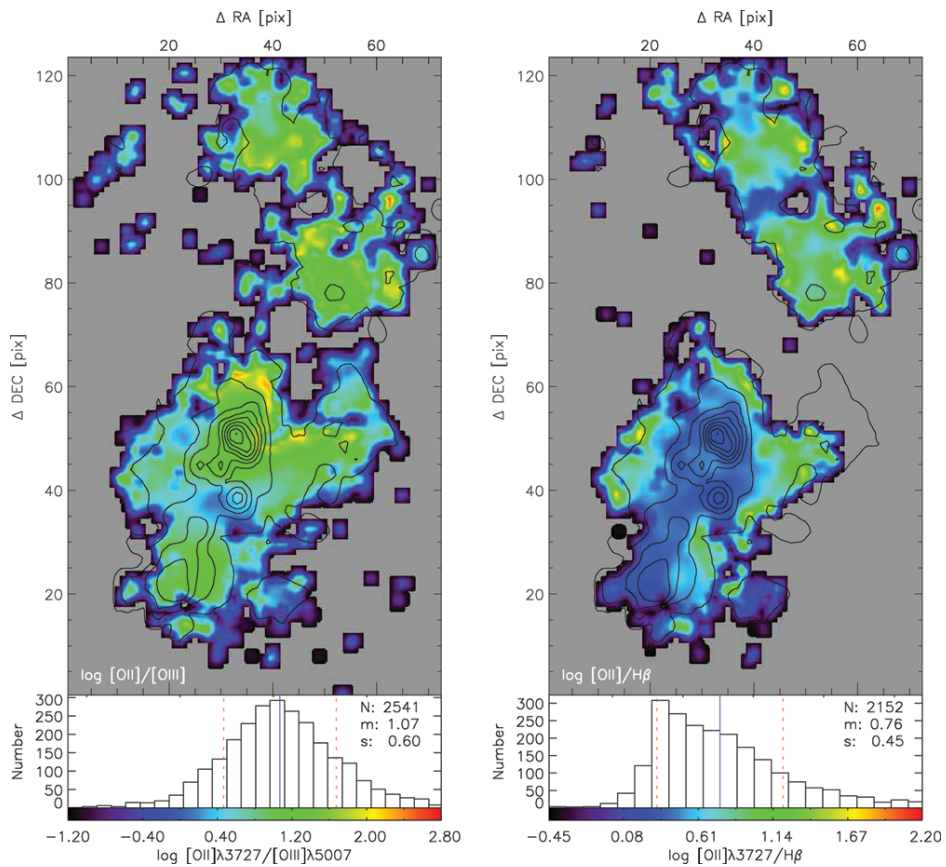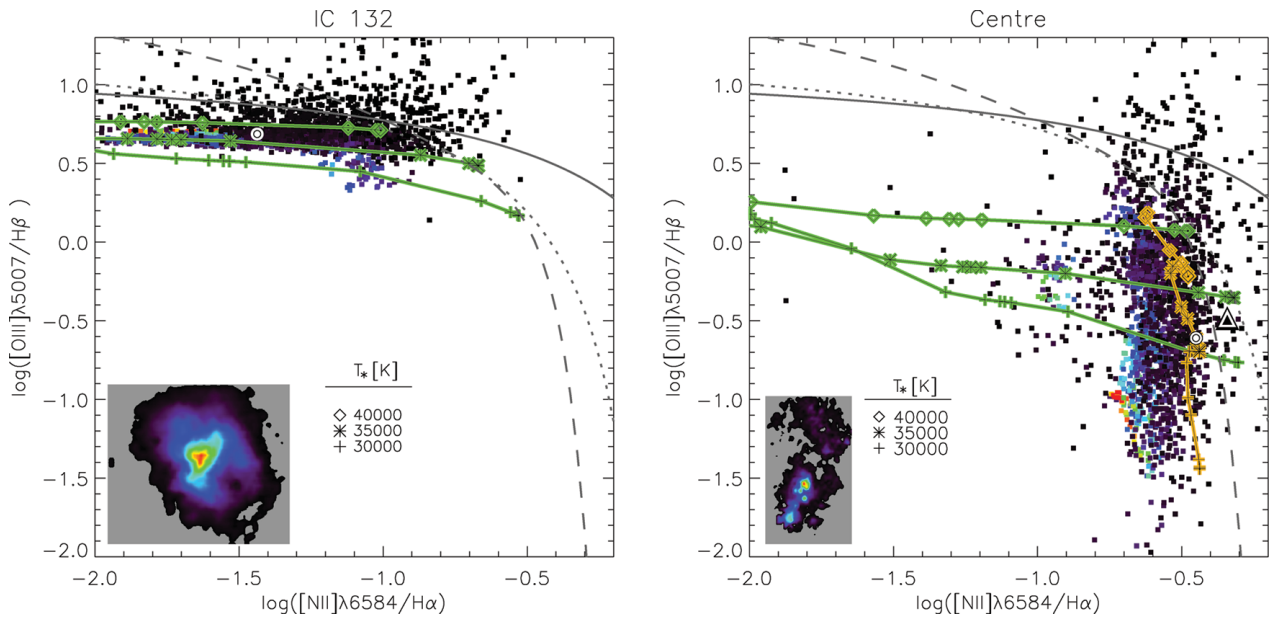**Figure 17.** Diagnostic line ratios for the central regions as labelled.

**Figure 18.** Ionization sensitive ratios [O II] λ3727/[O III] λ5007 and [O II] λ3727/Hβ for the central region.

**Figure 19.** BPT diagnostic diagrams for each spaxel in the external zone IC 132 (left-hand panel) and the central zones of M33 (right-hand panel). Different boundaries for photoionization are represented: continuous line from (Kewley & Dopita 2002), dotted line from (Kauffmann et al. 2003) and dashed line from (Stasińska et al. 2006). The colours of individual squares indicate the spatial position according to the inserted map of the regions. The black and white concentric circles are the position of the integrated field for IC 132 and BCLMP 93. The symbols connected by coloured lines are the results from photoionization models computed at increasing distance from the ionization source, where the symbols closest to the boundary lines are the final result of the computation. Three temperatures are given for a combination of $\log U$ and abundance. For IC 132, the best fit was found with models running horizontally in the diagram (green lines), while the central zone was fitted not only by horizontal but also by vertical (orange lines) models. The triangle symbol in the diagram for the centre indicates the emission-line zone closer to the strong X-ray source (see text).

diagnostic diagram intruding in the AGN zone, mostly the Seyfert zone in the case of IC 132 and the LINER and transition zones in the case of the M33 central region. Curiously, no anomalous line ratios are detected for the position of individual spaxels near the M33 X-8 X-ray source in the central region. The position of the emission-line zone nearest to the X-ray source is indicated with a triangle symbol in the left-hand panel of Fig. 19.

### 5.1 Matching the diagnostic diagrams to pseudo-3D photoionization models

Bearing in mind that we are dealing with spatially resolved data and in an effort to understand the dichotomy in the distribution of individual spaxel line ratios in the BPT diagrams shown in Fig. 19, we have computed what can be called pseudo-3D photoionization models. Our grid of models have spherical closed geometry, constant density with a blackbody as the ionizing source and a range of ionization parameters ($\log U$) from $-2.0$ to $0.0$, metallicities ($Z$) from 0.1 to 2.0 $Z_\odot$ and stellar temperature ($T_*$) from 30 000 to 50 000 K. As a first approach to full 3D models, we have used all intermediate shell results from each CLOUDY (Ferland et al. 1998) photoionization model to represent the radial behaviour of the relevant gas parameters inside the nebula. The models are discussed in detail in a forthcoming paper (López et al., in preparation).

Fig. 19 shows in the green-black solid lines the results from the photoionization models. Each line corresponds to a model with a given combination of $\log U$, $Z$ and $T_*$, following the computed results at increasing distance from the inner face of the cloud. The end or outer edge of the computation is marked with the corresponding symbol in bold and is generally the one closest to the boundary lines.

It is possible to see in Fig. 19 that the models are capable of reproducing the position and spread of values of both regions even though the spaxels in IC 132 show a horizontal dispersion while those of the central zones have a vertical dispersion. In particular, the models that best fit the data for IC 132 have $\log(U) = -1$, $T_* = 35\,000$ and $40\,000$ K and $Z = 0.1\,Z_\odot$. $T_* = 35\,000$ fits the high-brightness spaxels and $T_* = 40\,000$ lies above these spaxels but fits better the low-brightness ones. $T_* = 30\,000$ is below most of the spaxels but fits a small spur of objects around [N II]/H$\alpha = -1.05$.

For the central zone, models with the same temperatures (3.0, 3.5 and 4.0 kK), $\log(U) = -1$ and $Z = 2.0\,Z_\odot$ span the location of most of the individual spaxels. Another set of models with the same $T_*$, but $\log(U) = -2$ and $Z = 0.1\,Z_\odot$ also fit the observations but with vertical spread; these are the orange broken lines in the right-hand panel of Fig. 19. These vertical models only fit the rightmost distribution of central spaxels, corresponding to the faint ones. The bright spaxels fall on the lower left-hand tip of the distribution cloud and could not be fitted by our set of models. However, the integrated position for BCLMP 93 (concentric circles in the figure) is well fitted by both sets of models.

For the same temperatures, the position of the horizontal models is controlled by the metallicity – the higher it is, the lower the [O III] $\lambda5007$/H$\beta$ ratio. The orientation of the models is controlled by the ionization parameter, being vertical for low values of $U$.

For the central zone, we favour the vertical models as indicators of the physical conditions in the nebula, mainly because they are consistent with the high metallicity expected in this region, and the horizontal models instead would represent regions of low metallicity.

As mentioned above, while the spaxels with high H$\alpha$ surface brightness are inside the boundary starburst line of the BPT diagram,

many of the low Hα surface brightness spaxels that are farther away from the ionizing source appear outside the boundary; this obviously does not mean that an AGN exists. Possible explanations are that those pixels have low S/N or perhaps diffuse radiation has to be considered. In any case, this raises a question about the wisdom of using photoionization models computed for integrated systems to define a reference boundary for photoionization and apply it to diagnostic diagrams for resolved systems.

## 6 WR STARS

WR stars are hot and luminous, with broad emission lines in the optical range due to a considerable mass-loss through winds (Abbott & Conti 1987). They represent an evolved stage of O stars when the radiation pressure cannot be counterbalanced by gravity and the outer layers of the stars are blown away. WR stars' more common subtypes are the WN that show a prominent nitrogen emission in the 4600–4720 Å range, known as the blue bump (BB), and the WC, with carbon emission in the 5750–5870 Å range, known as the red bump. The [He II] λ4686 Å emission line is present in both types.

If WR features are detected, then stars more massive than $M_{WR} \sim 25\,M_\odot$ must be present in the cluster if solar metallicity is presumed (Pindao et al. 2002). Assuming an instantaneous burst, the WR features are visible from roughly 3 Myr to almost 7 Myr of age, their lifetimes getting shorter with lower metallicity (Schaerer & Vacca 1998). The WR feature can serve as a constraint to estimate the age of the burst if its metallicity is known.

D'Odorico & Benvenuti (1983) studied the integrated ultraviolet (*IUE*) and optical (ESO 3.6 m) spectrum of IC 132. They found the presence of the BB (λ4686), indicating the existence of WR stars, which they classified as WN4. They estimated the ionizing source as a single star with $T_* = 40\,000 \pm 5\,000$ K and mass larger than $100\,M_\odot$ or a system of three components (O4V+O9.5I+WN4). They noted the need for spatial resolution to determine the extent and nature of the WR stars (few overluminous objects versus many normal WR stars).

We used the IFS observations to map the spatial distribution of the WR features by measuring the detected BB in each individual spectrum and reconstructing the spatial map in the same fashion as the emission-line maps were constructed. We detected two peaks in the BB distribution in IC 132. Fig. 20 shows the map of the blue feature flux measured by fitting a Gaussian in a 70 Å interval centred at 4686 Å, with the Hα contour overlaid. Also shown is a zoom-in of the BB emission in the region where we detect two peaks and the integrated spectra of both regions. The BB luminosity, equivalent width and flux normalized to Hβ are shown in Table 3. Assuming an average luminosity for the BB of $10^{36.5}$ (Pindao et al. 2002, for a single WN7 star), the estimated number of WN stars in region A is 21 and in region B is 24. Taking the total number of Lyman photons estimated by (D'Odorico & Benvenuti 1983) $N_{Ly} = 8.2 \times 10^{49}$ s$^{-1}$ and assuming that a single WR produces $1.7 \times 10^{49}$ s$^{-1}$ (WN; Schaerer & Vacca 1998), the derived number of stars is 5 for the whole region. It is interesting to note the discrepancy found in the number of WR stars computed by different methods. This discrepancy may be linked to aperture effects in the observations.

Given that the models of WR formation predict that as a result of the increased mass-loss rates the number of WR stars will increase with increasing metallicity (Schaerer & Vacca 1998; Meynet & Maeder 2005), it is surprising that no WR features are detected in the higher metallicity central region of M33. One has to consider that the spectrum of the central region BCLMP 93 is of lower S/N than
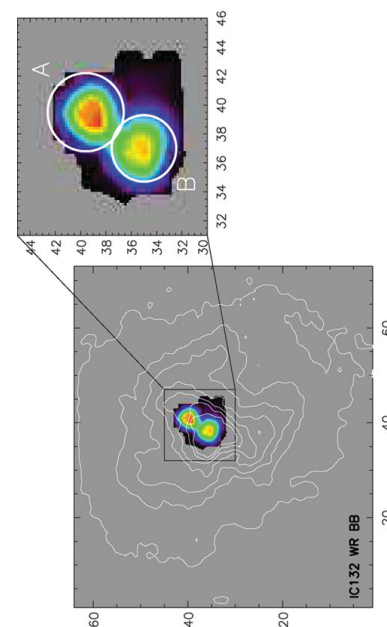


**Figure 20.** WR detection in IC 132. The left-hand panel shows the distribution of the BB with the Hα isocontours overplotted. The central panel is a zoomed-in version. The right-hand panel shows the integrated spectrum for regions A and B. The position of the blue and red bumps is indicated. No red bump is detected.

**Table 3.** BB luminosity, EW and BB/Hβ for the two regions identified in IC 132.

| Region | log(L) (erg s⁻¹) | EW(BB) (Å) | BB/Hβ |
|---|---|---|---|
| A | 37.84 | 15 | 0.38 |
| B | 37.89 | 13 | 0.41 |

that of IC 132, which makes it more difficult to detect and measure the WR bumps. Nevertheless, a limit to the number of WR stars in BCLMP 93 that may be present but cannot be confidently detected can be obtained by estimating the BB with different continuum placements. In this way, we find that BCLMP 93 could contain at most four WN7 stars.

## 7 SEGMENTATION ANALYSIS

Although the intensity maps provide a view of the spatial distribution of the emission-line flux, temperatures, abundances and other estimated values, an easier quantitative representation of variations with position as well as a study of the effect of aperture size is provided by analysing the H II region in concentric layers. To this end, we have adopted an approach that defines segments or shells of the H II region according to the Hα surface brightness level. The segmentation of the observed FOV allows the study of the faint areas where the spaxel-by-spaxel analysis cannot be performed, given the low S/N of individual elements. However, when the flux is integrated in a single spectrum, the S/N improves and conditions can be estimated, albeit with the loss of spatial azimuthal resolution. This kind of analysis is a clear advantage of IFS over long-slit observations for the study of faint areas.

We present the results in two forms:

(I) The individual shell values, i.e. considering each section as an individual region
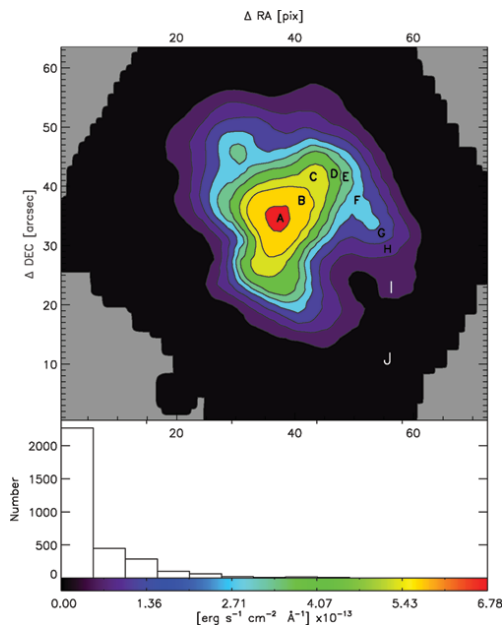


**Figure 21.** IC 132 Hα map with concentric apertures. The single letter (A through J) designates the shell's area.

**Table 4.** Reddening-corrected integrated fluxes for IC 132 individual shells. Fluxes are normalized to Hβ = 100.

| λ | Ion | Individual | | | | | | | | | |
|---|---|---|---|---|---|---|---|---|---|---|---|
| | | A | B | C | D | E | F | G | H | I | J |
| 3727 | [O II] | 150.7 ± 8.0 | 164.7 ± 8.9 | 192.4 ± 11.7 | 210.5 ± 15.7 | 204.5 ± 16.5 | 188.9 ± 17.6 | 221.6 ± 21.0 | 241.3 ± 27.7 | 267.2 ± 44.8 | 634.6 ± 282.6 |
| 4010 | Hδ | 33.5 ± 2.4 | 31.5 ± 2.6 | 31.9 ± 3.1 | 32.0 ± 3.9 | 31.5 ± 3.9 | 31.0 ± 4.0 | 30.5 ± 4.8 | 29.5 ± 7.0 | 28.4 ± 10.8 | 24.6 ± 54.3 |
| 4340 | Hγ | 50.0 ± 2.8 | 48.5 ± 2.6 | 49.2 ± 3.8 | 49.3 ± 5.3 | 48.2 ± 5.6 | 47.7 ± 6.7 | 47.1 ± 7.8 | 45.7 ± 10.0 | 43.0 ± 15.1 | 31.4 ± 52.5 |
| 4363 | [O III]ᵃ | 6.7 ± 1.2 | 6.4 ± 1.3 | 7.7 ± 1.7 | 8.4 ± 2.3 | 10.7 ± 2.7 | 11.2 ± 3.3 | 14.0 ± 4.3 | 18.9 ± 6.3 | 29.0 ± 11.6 | 127.0 ± 67.6 |
| 4861 | [Hβ] | 100.0 ± 3.1 | 100.0 ± 4.1 | 100.0 ± 5.7 | 100.0 ± 7.9 | 100.0 ± 7.9 | 100.0 ± 8.6 | 100.0 ± 9.6 | 100.0 ± 12.1 | 100.0 ± 18.5 | 100.0 ± 48.2 |
| 4959 | [O III] | 175.1 ± 6.4 | 171.4 ± 7.3 | 164.7 ± 8.0 | 159.6 ± 11.8 | 157.8 ± 11.6 | 158.0 ± 12.3 | 154.7 ± 13.4 | 155.4 ± 17.4 | 160.9 ± 27.5 | 208.3 ± 85.4 |
| 5007 | [O III] | 500.1 ± 12.2 | 485.6 ± 15.4 | 463.5 ± 20.3 | 449.1 ± 27.8 | 443.5 ± 28.1 | 445.1 ± 30.8 | 435.0 ± 33.3 | 433.3 ± 42.4 | 444.6 ± 66.5 | 576.1 ± 209.9 |
| 6312 | [S III] | 2.7 ± 1.3 | 3.4 ± 2.1 | 3.9 ± 2.7 | 4.6 ± 3.4 | 4.9 ± 4.0 | 5.5 ± 4.7 | 6.1 ± 5.8 | 7.4 ± 7.9 | 12.0 ± 13.8 | 51.9 ± 60.3 |
| 6548 | [N II] | 2.9 ± 1.1 | 2.8 ± 1.2 | 3.2 ± 1.3 | 3.4 ± 1.8 | 3.5 ± 2.2 | 3.5 ± 2.1 | 4.1 ± 2.7 | 4.7 ± 3.4 | 6.7 ± 4.4 | 16.4 ± 14.8 |
| 6564 | Hα | 284.5 ± 7.1 | 284.1 ± 8.8 | 284.3 ± 12.2 | 284.2 ± 17.8 | 284.8 ± 18.8 | 284.5 ± 19.5 | 284.5 ± 22.5 | 284.8 ± 28.0 | 285.8 ± 40.0 | 317.8 ± 112.4 |
| 6584 | [N II] | 6.7 ± 0.8 | 7.7 ± 0.9 | 9.1 ± 1.2 | 9.8 ± 2.2 | 9.6 ± 2.7 | 9.1 ± 2.4 | 10.1 ± 3.3 | 11.3 ± 4.2 | 12.7 ± 5.0 | 20.0 ± 15.7 |
| 6717 | [S II] | 8.9 ± 0.8 | 9.9 ± 0.9 | 11.7 ± 1.2 | 12.7 ± 3.2 | 12.3 ± 4.2 | 11.5 ± 3.0 | 12.9 ± 4.6 | 14.0 ± 5.4 | 16.1 ± 4.9 | 26.0 ± 16.2 |
| 6731 | [S II] | 5.7 ± 0.4 | 6.6 ± 0.7 | 7.6 ± 0.9 | 8.4 ± 1.5 | 8.2 ± 1.7 | 7.3 ± 2.0 | 8.6 ± 2.5 | 9.2 ± 3.4 | 9.5 ± 5.5 | 11.6 ± 18.8 |
| 7136 | [Ar III] | 8.3 ± 1.0 | 6.6 ± 1.2 | 7.7 ± 1.4 | 8.3 ± 2.9 | 8.3 ± 1.8 | 8.4 ± 2.2 | 8.2 ± 3.0 | 7.3 ± 4.8 | 5.6 ± 4.3 | 2.9 ± 12.6 |
| 9068 | [S III] | 27.5 ± 6.3 | 24.0 ± 5.4 | 28.4 ± 6.5 | 30.8 ± 8.2 | 30.6 ± 7.6 | 28.1 ± 7.5 | 28.2 ± 9.3 | 23.4 ± 9.9 | 18.9 ± 13.2 | 13.1 ± 33.5 |
| I(Hβ)(erg s⁻¹ cm⁻² 10⁻¹³) | | 79.29 ± 0.18 | 82.86 ± 0.24 | 79.24 ± 0.32 | 80.21 ± 0.45 | 80.99 ± 0.45 | 80.17 ± 0.49 | 80.52 ± 0.55 | 80.50 ± 0.69 | 80.21 ± 1.05 | 71.20 ± 2.43 |
| C(Hβ) | | 0.50 ± 0.06 | 0.42 ± 0.04 | 0.40 ± 0.04 | 0.40 ± 0.05 | 0.37 ± 0.05 | 0.36 ± 0.05 | 0.36 ± 0.06 | 0.39 ± 0.06 | 0.49 ± 0.09 | 1.30 ± 0.13 |
| EW(Hβ) (Å) | | 130.34 ± 11.42 | 139.98 ± 11.83 | 194.10 ± 13.93 | 292.21 ± 17.09 | 284.06 ± 16.85 | 266.77 ± 16.33 | 218.40 ± 14.78 | 183.85 ± 13.56 | 132.50 ± 11.51 | 23.46 ± 4.84 |

ᵃContaminated by mercury street lamps.

**Table 5.** Integrated temperatures, abundances and line ratios for IC 132 individual shells.

| | Individual | | | | | | | |
| --- | --- | --- | --- | --- | --- | --- | --- | --- |
| | A | B | C | D | E | F | G | H |
| $T_e([O III])^a$ | 12800 ± 900 | 12700 ± 1000 | 13900 ± 1300 | 14600 ± 1800 | 16500 ± 2100 | 16800 ± 2600 | 19200 ± 3500 | 23400 ± 5700 |
| $T_e([O II])_{PM03}$ | 11300 ± 400 | 12100 ± 300 | 12800 ± 400 | 13200 ± 500 | 14200 ± 500 | 14400 ± 600 | 15600 ± 700 | 17300 ± 900 |
| $T_e([O II])_{G92}$ | 12000 ± 600 | 11900 ± 700 | 12700 ± 900 | 13200 ± 1300 | 14500 ± 1500 | 14800 ± 1800 | 16500 ± 2400 | 19400 ± 4000 |
| $T_e([S III])_{6312}$ | 10700 ± 100 | 12800 ± 200 | 12500 ± 300 | 13100 ± 400 | 13500 ± 500 | 15100 ± 700 | 16500 ± 1000 | 22400 ± 2800 |
| $T_e([S III])_{SO23}$ | 9300 ± 1900 | 9600 ± 1900 | 9200 ± 1700 | 9000 ± 1500 | 900 ± 1500 | 9100 ± 1600 | 9100 ± 1600 | 9600 ± 1700 |
| $T_e([S III])_{H06}$ | 12000 ± 1000 | 11900 ± 1200 | 13300 ± 1600 | 14000 ± 2200 | 16400 ± 2500 | 16800 ± 3100 | 19800 ± 4100 | 24700 ± 6800 |
| $12 + \log(O^+/H^+)^b$ | 7.46 ± 0.19 | 7.50 ± 0.22 | 7.46 ± 0.26 | 7.44 ± 0.33 | 7.29 ± 0.32 | 7.23 ± 0.39 | 7.16 ± 0.42 | 7.01 ± 0.52 |
| $12 + \log(O^{++}/H^+)^b$ | 7.94 ± 0.19 | 7.93 ± 0.23 | 7.80 ± 0.26 | 7.73 ± 0.32 | 7.60 ± 0.30 | 7.58 ± 0.36 | 7.44 ± 0.38 | 7.27 ± 0.45 |
| $12 + \log(O/H)^b$ | 8.06 ± 0.27 | 8.07 ± 0.32 | 7.97 ± 0.37 | 7.91 ± 0.46 | 7.77 ± 0.44 | 7.74 ± 0.53 | 7.62 ± 0.57 | 7.46 ± 0.68 |
| $12 + \log(S^+/H^+)$ | 5.49 ± 0.32 | 5.35 ± 0.36 | 5.46 ± 0.44 | 5.46 ± 0.56 | 5.43 ± 0.66 | 5.29 ± 0.79 | 5.29 ± 1.07 | 5.14 ± 1.73 |
| $12 + \log(S^{++}/H^+)$ | 6.69 ± 0.18 | 6.49 ± 0.17 | 6.58 ± 0.18 | 6.57 ± 0.22 | 6.55 ± 0.19 | 6.45 ± 0.19 | 6.39 ± 0.26 | 6.12 ± 0.35 |
| $ICF(S^+ + S^{++})$ | 1.31 ± 0.08 | 1.28 ± 0.10 | 1.22 ± 0.11 | 1.19 ± 0.13 | 1.20 ± 0.13 | 1.22 ± 0.15 | 1.19 ± 0.16 | 1.18 ± 0.18 |
| $12 + \log(S/H)$ | 6.83 ± 0.37 | 6.63 ± 0.39 | 6.70 ± 0.47 | 6.68 ± 0.60 | 6.66 ± 0.68 | 6.56 ± 0.81 | 6.49 ± 1.10 | 6.24 ± 1.77 |
| $\log(S/O)$ | −1.34 ± 0.02 | −1.55 ± 0.02 | −1.35 ± 0.02 | −1.31 ± 0.03 | −1.19 ± 0.03 | −1.27 ± 0.03 | −1.20 ± 0.03 | −1.29 ± 0.04 |
| $12 + \log(N^+/H^+)$ | 5.92 ± 0.01 | 5.98 ± 0.01 | 5.99 ± 0.01 | 5.98 ± 0.02 | 5.88 ± 0.03 | 5.85 ± 0.03 | 5.80 ± 0.03 | 5.73 ± 0.04 |
| $\log(N/O)$ | −1.54 ± 0.06 | −1.52 ± 0.06 | −1.47 ± 0.06 | −1.46 ± 0.07 | −1.41 ± 0.07 | −1.38 ± 0.08 | −1.36 ± 0.08 | −1.28 ± 0.09 |
| $12 + \log(O/H) (N2)$ | 8.02 ± 0.06 | 8.05 ± 0.09 | 8.08 ± 0.20 | 8.09 ± 0.43 | 8.09 ± 0.48 | 8.08 ± 0.50 | 8.10 ± 0.71 | 8.12 ± 1.19 |
| $12 + \log(O/H) (R_{23 lower})$ | 8.06 ± 0.08 | 8.07 ± 0.10 | 8.10 ± 0.13 | 8.11 ± 0.18 | 8.10 ± 0.18 | 8.07 ± 0.20 | 8.12 ± 0.22 | 8.15 ± 0.27 |
| $12 + \log(O/H) (Ar_3O_3)$ | 8.03 ± 0.06 | 7.91 ± 0.09 | 8.03 ± 0.08 | 8.09 ± 0.14 | 8.10 ± 0.09 | 8.10 ± 0.11 | 8.10 ± 0.15 | 8.04 ± 0.29 |
| $12 + \log(O/H) (S_3O_3)$ | 8.27 ± 0.05 | 8.24 ± 0.05 | 8.29 ± 0.04 | 8.32 ± 0.05 | 8.32 ± 0.04 | 8.31 ± 0.05 | 8.31 ± 0.06 | 8.27 ± 0.09 |
| $R_{S2}$ | 1.21 ± 0.03 | 1.45 ± 0.03 | 1.49 ± 0.03 | 1.51 ± 0.05 | 1.71 ± 0.06 | 1.62 ± 0.05 | 1.86 ± 0.06 | 2.21 ± 0.07 |
| $\log(SO_{23})$ | −0.77 ± 0.26 | −0.82 ± 0.26 | −0.74 ± 0.25 | −0.71 ± 0.24 | −0.71 ± 0.24 | −0.73 ± 0.24 | −0.74 ± 0.23 | −0.81 ± 0.23 |
| N2 | −1.63 ± 0.01 | −1.57 ± 0.02 | −1.49 ± 0.05 | −1.46 ± 0.11 | −1.47 ± 0.12 | −1.50 ± 0.12 | −1.45 ± 0.18 | −1.40 ± 0.31 |
| $\log(R_{23})$ | 0.92 ± 0.04 | 0.91 ± 0.05 | 0.91 ± 0.06 | 0.91 ± 0.09 | 0.91 ± 0.09 | 0.90 ± 0.10 | 0.91 ± 0.11 | 0.92 ± 0.14 |
| $\log(O_{32})$ | 0.65 ± 0.06 | 0.60 ± 0.06 | 0.51 ± 0.07 | 0.46 ± 0.09 | 0.47 ± 0.10 | 0.50 ± 0.11 | 0.43 ± 0.11 | 0.39 ± 0.14 |
| $\log(Ar_3O_3)$ | −1.78 ± 0.04 | −1.87 ± 0.06 | −1.78 ± 0.06 | −1.73 ± 0.12 | −1.73 ± 0.08 | −1.73 ± 0.10 | −1.72 ± 0.13 | −1.77 ± 0.23 |
| $\log(S_3O_3)$ | −1.15 ± 0.08 | −1.19 ± 0.07 | −1.10 ± 0.08 | −1.06 ± 0.09 | −1.05 ± 0.08 | −1.08 ± 0.08 | −1.07 ± 0.11 | −1.15 ± 0.15 |
| $\log(U) ([S II]/[S III])$ | −1.46 ± 0.16 | −1.58 ± 0.15 | −1.61 ± 0.16 | −1.62 ± 0.21 | −1.59 ± 0.21 | −1.55 ± 0.21 | −1.62 ± 0.26 | −1.81 ± 0.31 |
| $\log(U) ([O II]/[O III])$ | −2.50 ± 0.02 | −2.54 ± 0.02 | −2.61 ± 0.02 | −2.65 ± 0.03 | −2.65 ± 0.03 | −2.62 ± 0.04 | −2.68 ± 0.04 | −2.71 ± 0.05 |
| $\log(\eta')$ | 0.26 ± 0.07 | 0.24 ± 0.06 | 0.31 ± 0.07 | 0.35 ± 0.08 | 0.36 ± 0.09 | 0.35 ± 0.10 | 0.39 ± 0.10 | 0.32 ± 0.12 |
| $\log([O III]\lambda5007/H\beta)$ | 0.70 ± 0.01 | 0.69 ± 0.01 | 0.67 ± 0.02 | 0.65 ± 0.03 | 0.65 ± 0.03 | 0.65 ± 0.03 | 0.64 ± 0.03 | 0.64 ± 0.04 |
| $\log([N II]\lambda6584/H\alpha)$ | −1.63 ± 0.05 | −1.57 ± 0.05 | −1.49 ± 0.06 | −1.46 ± 0.09 | −1.47 ± 0.12 | −1.50 ± 0.11 | −1.45 ± 0.14 | −1.40 ± 0.16 |
| $\log([S II]\lambda\lambda6717,31/H\alpha)$ | −1.27 ± 0.06 | −1.25 ± 0.06 | −1.17 ± 0.06 | −1.13 ± 0.08 | −1.15 ± 0.10 | −1.20 ± 0.09 | −1.16 ± 0.10 | −1.13 ± 0.10 |

*References.* PM03: (Pérez-Montero & Díaz 2003); G92: (Garnett 1992); H06: (Hägele et al. 2006).
$^a$Upper limit. $^b$Lower limit.

(II) The cumulative values, i.e. adding the sections in a cumulative way from the centre to the outer boundary, going from $\overline{AB} = A + B$ to $\overline{AJ} = A + B + \cdots + I + J$.

Therefore, in this notation A is the spectrum of the brightest central spaxels, while $\overline{AJ}$ represents the integrated spectrum of the whole region (see Fig. 21 for the segmentation of IC 132). The same notation is used for BCLMP 93 but with lowercase letters going from 'a' to 'h' (see Fig. 32).

## 7.1 Integrated properties of IC 132

To analyse the radial properties of IC 132, the field was segmented in 10 sections of equal Hα surface brightness covering from the brightest to the faintest spaxels. The shells were labelled from A to J as shown in Fig. 21. The segment sizes were defined to have constant integrated flux in Hα after applying the extinction correction.

As can be seen from Tables 4 and 8, the integrated flux of Hβ is roughly the same for all sections in both regions, i.e. about $80 \times 10^{-13}$ erg s$^{-1}$ cm$^{-2}$ for IC 132 and about $20 \times 10^{-13}$ erg s$^{-1}$ cm$^{-2}$ for BCLMP 93; small variations are present because of the discrete jumps in flux between spaxels and no interpolation was used to exactly define the isocontours.

The emission-line measurements, their errors, and the resulting line ratios, temperatures and abundances, are given in Tables 4–7 for the individual and cumulative spectra.

The resulting integrated properties for IC 132 are shown in Figs 22–30, for electron temperatures, ionic and total abundances, empirical abundances, line ratios, ionization sensitive ratios, extinction and EW(Hβ). Each figure shows the values for individual shells in the left-hand panels and for cumulative segmentation in the right-hand panels. Individual shells I and J are not shown, given the large errors obtained. Errors were calculated by formal propagation of each line flux associated error. For $T_e([O\ II])_{PM03}$, also the error in $n_e$ determination at the low density limit was added in quadrature, to take into account the spread of the models in the original paper.

Fig. 22 shows the radial trend of the electron temperatures. Inside the errors there is a clear tendency for the temperature to increase with radius, except for $T_e([S\ III])$ computed with the $SO_{23}$ method, which shows no temperature gradient. The $T_e$ increasing tendency is reflected in the radial trend of abundance shown in Fig. 23 where it is possible to see that the estimated O/H goes to smaller abundances in the outer regions. However, given the large errors obtained, the radial behaviour is also compatible with a constant value for the whole region. In such cases, the total (O/H) may be set between 7.8 and 8.2.

For Fig. 24, although a slight decrease with radius is noted, the ionic and total abundances are compatible with a constant value within errors. Total (S/H) is between 6.4 and 7.1. The mean value from the 2D map of 6.62 may as well be adopted as the representative value of the region.

Interestingly, in Fig. 25, S/O has a rather flat trend, while N/O displays an apparent increase with radial distance in the individual shell analysis. This is contrary to the inverse trend naively expected, given that the WR stars are located at the centre of IC 132 (see Section 6). On the other hand, it might simply mean that the WR phenomenon did not have enough time to pollute the ionized gas or that, even if some contamination occurs, within the errors it cannot be observed. The radial increase may be explained by: (i) star formation was propagated from the border to the central part of the region; and (ii) enrichment of an old population (by

**Table 6.** Reddening-corrected fluxes for IC 132 accumulated shells. Fluxes are normalized to Hβ = 100.

| λ | Ion | Cumulative | | | | | | | | | |
| --- | --- | --- | --- | --- | --- | --- | --- | --- | --- | --- | --- |
| | | $\overline{AA}$ | $\overline{AB}$ | $\overline{AC}$ | $\overline{AD}$ | $\overline{AE}$ | $\overline{AF}$ | $\overline{AG}$ | $\overline{AH}$ | $\overline{AI}$ | $\overline{AJ}$ |
| 3727 | [O II] | 150.7 ± 8.0 | 157.8 ± 8.0 | 169.2 ± 8.7 | 179.5 ± 9.5 | 184.5 ± 10.1 | 185.2 ± 10.6 | 190.4 ± 11.4 | 196.7 ± 13.0 | 204.5 ± 15.5 | 242.8 ± 33.9 |
| 4010 | Hδ | 33.5 ± 2.4 | 32.5 ± 2.4 | 32.3 ± 2.6 | 32.2 ± 2.8 | 32.1 ± 2.9 | 31.9 ± 3.0 | 31.7 ± 3.3 | 31.4 ± 3.7 | 31.1 ± 4.5 | 30.8 ± 9.4 |
| 4340 | Hγ | 50.0 ± 2.8 | 49.2 ± 2.2 | 49.2 ± 2.5 | 49.2 ± 2.9 | 49.0 ± 3.3 | 48.8 ± 3.8 | 48.5 ± 4.3 | 48.2 ± 5.0 | 47.6 ± 6.2 | 45.7 ± 11.4 |
| 4363 | [O III]$^a$ | 6.7 ± 1.2 | 6.6 ± 1.0 | 6.9 ± 1.1 | 7.3 ± 1.3 | 8.0 ± 1.5 | 8.5 ± 1.8 | 9.2 ± 2.1 | 10.4 ± 2.5 | 12.4 ± 3.3 | 22.6 ± 7.8 |
| 4861 | [Hβ] | 100.0 ± 3.1 | 100.0 ± 3.5 | 100.0 ± 4.0 | 100.0 ± 4.7 | 100.0 ± 5.2 | 100.0 ± 5.6 | 100.0 ± 6.1 | 100.0 ± 6.8 | 100.0 ± 8.2 | 100.0 ± 12.8 |
| 4959 | [O III] | 175.1 ± 6.4 | 173.2 ± 6.7 | 170.4 ± 6.8 | 167.7 ± 7.6 | 165.7 ± 8.2 | 164.4 ± 8.7 | 163.0 ± 9.2 | 162.0 ± 10.1 | 161.9 ± 12.0 | 166.1 ± 19.3 |
| 5007 | [O III] | 500.1 ± 12.2 | 492.7 ± 13.4 | 483.1 ± 15.1 | 474.6 ± 17.3 | 468.3 ± 19.0 | 464.5 ± 20.6 | 460.2 ± 22.2 | 456.8 ± 24.7 | 455.4 ± 29.8 | 466.4 ± 47.9 |
| 6312 | [S III] | 2.7 ± 1.3 | 3.1 ± 1.7 | 3.4 ± 2.0 | 3.7 ± 2.4 | 3.9 ± 2.7 | 4.2 ± 3.0 | 4.4 ± 3.4 | 4.8 ± 4.0 | 5.6 ± 5.1 | 9.7 ± 9.8 |
| 6548 | [N II] | 2.9 ± 1.1 | 2.8 ± 1.1 | 3.0 ± 1.2 | 3.1 ± 1.3 | 3.2 ± 1.4 | 3.2 ± 1.5 | 3.3 ± 1.7 | 3.5 ± 1.9 | 3.8 ± 2.1 | 5.0 ± 3.1 |
| 6564 | Hα | 284.5 ± 7.1 | 284.3 ± 7.7 | 284.3 ± 8.8 | 284.3 ± 10.4 | 284.4 ± 11.7 | 284.4 ± 12.7 | 284.4 ± 14.0 | 284.4 ± 15.7 | 284.6 ± 18.4 | 287.8 ± 28.2 |
| 6584 | [N II] | 6.7 ± 0.8 | 7.2 ± 0.8 | 7.8 ± 0.9 | 8.3 ± 1.1 | 8.6 ± 1.4 | 8.7 ± 1.6 | 8.9 ± 1.8 | 9.2 ± 2.1 | 9.6 ± 2.4 | 10.5 ± 3.4 |
| 6717 | [S II] | 8.6 ± 1.9 | 9.2 ± 1.4 | 10.0 ± 0.9 | 10.7 ± 1.1 | 11.0 ± 1.0 | 11.3 ± 2.2 | 11.6 ± 1.1 | 11.7 ± 1.0 | 12.2 ± 2.8 | 12.8 ± 1.5 |
| 6731 | [S II] | 5.8 ± 0.3 | 6.3 ± 0.3 | 6.2 ± 0.5 | 6.3 ± 0.6 | 6.6 ± 0.8 | 6.6 ± 0.9 | 6.9 ± 1.0 | 6.9 ± 1.2 | 7.2 ± 1.4 | 7.0 ± 2.0 |
| 7136 | [Ar III] | 8.3 ± 1.0 | 7.4 ± 0.9 | 7.5 ± 1.0 | 7.7 ± 1.3 | 7.8 ± 1.3 | 7.9 ± 1.3 | 7.9 ± 1.3 | 7.9 ± 1.5 | 7.6 ± 1.7 | 7.2 ± 2.1 |
| 9068 | [S III] | 27.5 ± 6.3 | 25.7 ± 5.0 | 26.6 ± 5.3 | 27.6 ± 5.8 | 28.2 ± 5.9 | 28.2 ± 5.9 | 28.2 ± 6.3 | 27.6 ± 6.5 | 26.6 ± 6.9 | 25.1 ± 8.9 |
| $I(H\beta)$(erg s$^{-1}$ cm$^{-2}$ 10$^{-13}$) | | 79.29 ± 0.18 | 162.15 ± 0.40 | 241.39 ± 0.69 | 321.61 ± 1.07 | 402.61 ± 1.47 | 482.78 ± 1.91 | 563.35 ± 2.43 | 643.90 ± 3.10 | 724.18 ± 4.18 | 795.15 ± 7.19 |
| $C(H\beta)$ | | 0.50 ± 0.06 | 0.45 ± 0.03 | 0.43 ± 0.03 | 0.42 ± 0.02 | 0.40 ± 0.02 | 0.40 ± 0.02 | 0.39 ± 0.02 | 0.39 ± 0.02 | 0.40 ± 0.02 | 0.49 ± 0.02 |
| EW(Hβ)(Å) | | 130.34 ± 11.42 | 135.09 ± 11.62 | 150.07 ± 12.25 | 170.79 ± 13.07 | 185.69 ± 13.63 | 195.56 ± 13.98 | 198.54 ± 14.09 | 196.59 ± 14.02 | 186.62 ± 13.66 | 114.99 ± 10.72 |

$^a$Contaminated by mercury street lamps.

**Table 7.** Integrated temperatures, abundances and line ratios for IC 132 accumulated shells.

| | Cumulative | | | | | | | | | |
|---|---|---|---|---|---|---|---|---|---|---|
| | $\overline{AA}$ | $\overline{AB}$ | $\overline{AC}$ | $\overline{AD}$ | $\overline{AE}$ | $\overline{AF}$ | $\overline{AG}$ | $\overline{AH}$ | $\overline{AI}$ | $\overline{AJ}$ |
| $T_e$([O III]) | 12700 ± 900 | 12700 ± 700 | 13100 ± 900 | 13400 ± 1000 | 14000 ± 1200 | 14500 ± 1300 | 15000 ± 1600 | 16000 ± 1900 | 17600 ± 2600 | 25300 ± 6960 |
| $T_e$([O II])$_{PM03}$ | 12100 ± 300 | 12100 ± 200 | 12300 ± 200 | 12600 ± 300 | 12900 ± 300 | 13100 ± 300 | 13500 ± 400 | 14000 ± 400 | 14800 ± 500 | 18000 ± 1000 |
| $T_e$([O II])$_{G92}$ | 11900 ± 600 | 11900 ± 500 | 12200 ± 600 | 12400 ± 700 | 12800 ± 800 | 13100 ± 900 | 13600 ± 1100 | 14200 ± 1300 | 15300 ± 1800 | 20700 ± 4900 |
| $T_e$([S III])$_{6312}$ | 10600 ± 100 | 11600 ± 200 | 12000 ± 200 | 12200 ± 200 | 12500 ± 200 | 13000 ± 300 | 13400 ± 400 | 14300 ± 500 | 16200 ± 800 | 27900 ± 4500 |
| $T_e$([S III])$_{SO_{23}}$ | 9400 ± 1900 | 9500 ± 1900 | 9400 ± 1800 | 9300 ± 1800 | 9200 ± 1700 | 9100 ± 1700 | 9200 ± 1700 | 9200 ± 1700 | 9300 ± 1700 | 9600 ± 1700 |
| $T_e$([S III])$_{H06}$ | 12000 ± 1000 | 12000 ± 900 | 12400 ± 1000 | 12800 ± 1200 | 13500 ± 1400 | 14000 ± 1600 | 14700 ± 1900 | 15900 ± 2200 | 17700 ± 3000 | 27000 ± 8300 |
| $12 + \log(O^+/H^+)$ | 7.45 ± 0.19 | 7.47 ± 0.16 | 7.47 ± 0.18 | 7.46 ± 0.21 | 7.43 ± 0.22 | 7.39 ± 0.25 | 7.35 ± 0.27 | 7.30 ± 0.30 | 7.22 ± 0.36 | 6.94 ± 0.56 |
| $12 + \log(O^{++}/H^+)$ | 7.94 ± 0.19 | 7.94 ± 0.17 | 7.89 ± 0.19 | 7.85 ± 0.21 | 7.80 ± 0.22 | 7.76 ± 0.24 | 7.70 ± 0.26 | 7.64 ± 0.28 | 7.54 ± 0.33 | 7.24 ± 0.48 |
| $12 + \log(O/H)$ | 8.06 ± 0.27 | 8.06 ± 0.23 | 8.03 ± 0.26 | 8.00 ± 0.30 | 7.95 ± 0.31 | 7.91 ± 0.34 | 7.87 ± 0.37 | 7.80 ± 0.41 | 7.71 ± 0.48 | 7.41 ± 0.74 |
| $12 + \log(S^+/H^+)$ | 5.49 ± 0.32 | 5.43 ± 0.29 | 5.44 ± 0.32 | 5.45 ± 0.37 | 5.44 ± 0.41 | 5.42 ± 0.45 | 5.40 ± 0.53 | 5.35 ± 0.64 | 5.27 ± 0.88 | 4.96 ± 1.92 |
| $12 + \log(S^{++}/H^+)$ | 6.69 ± 0.18 | 6.59 ± 0.14 | 6.58 ± 0.15 | 6.58 ± 0.16 | 6.57 ± 0.15 | 6.55 ± 0.15 | 6.52 ± 0.16 | 6.47 ± 0.17 | 6.37 ± 0.20 | 6.04 ± 0.27 |
| $ICF(S^+ + S^{++})$ | 1.31 ± 0.08 | 1.29 ± 0.07 | 1.27 ± 0.08 | 1.25 ± 0.09 | 1.24 ± 0.09 | 1.23 ± 0.10 | 1.22 ± 0.11 | 1.22 ± 0.12 | 1.21 ± 0.14 | 1.20 ± 0.20 |
| $12 + \log(S/H)$ | 6.84 ± 0.37 | 6.73 ± 0.32 | 6.72 ± 0.35 | 6.71 ± 0.40 | 6.69 ± 0.43 | 6.67 ± 0.48 | 6.64 ± 0.55 | 6.59 ± 0.67 | 6.48 ± 0.90 | 6.15 ± 1.93 |
| $\log(S/O)$ | −1.34 ± 0.02 | −1.45 ± 0.02 | −1.42 ± 0.02 | −1.39 ± 0.02 | −1.35 ± 0.02 | −1.33 ± 0.02 | −1.31 ± 0.02 | −1.30 ± 0.03 | −1.31 ± 0.03 | −1.34 ± 0.04 |
| $12 + \log(N^+/H^+)$ | 5.92 ± 0.01 | 5.95 ± 0.01 | 5.96 ± 0.01 | 5.97 ± 0.01 | 5.95 ± 0.02 | 5.93 ± 0.02 | 5.91 ± 0.02 | 5.89 ± 0.02 | 5.84 ± 0.02 | 5.65 ± 0.03 |
| $\log(N/O)$ | −1.54 ± 0.06 | −1.53 ± 0.05 | −1.51 ± 0.05 | −1.49 ± 0.05 | −1.47 ± 0.05 | −1.46 ± 0.06 | −1.44 ± 0.06 | −1.42 ± 0.07 | −1.38 ± 0.07 | −1.29 ± 0.10 |
| $12 + \log(O/H)$ (N2) | 8.02 ± 0.06 | 8.04 ± 0.07 | 8.05 ± 0.09 | 8.07 ± 0.13 | 8.07 ± 0.17 | 8.07 ± 0.21 | 8.08 ± 0.25 | 8.08 ± 0.32 | 8.09 ± 0.46 | 8.11 ± 1.14 |
| $12 + \log(O/H)$ ($R_{23lower}$) | 8.06 ± 0.08 | 8.07 ± 0.08 | 8.08 ± 0.10 | 8.09 ± 0.11 | 8.09 ± 0.12 | 8.09 ± 0.13 | 8.09 ± 0.14 | 8.10 ± 0.16 | 8.11 ± 0.19 | 8.19 ± 0.30 |
| $12 + \log(O/H)$ (Ar3O3) | 8.03 ± 0.06 | 7.98 ± 0.06 | 8.00 ± 0.06 | 8.02 ± 0.08 | 8.03 ± 0.08 | 8.04 ± 0.07 | 8.05 ± 0.08 | 8.05 ± 0.09 | 8.04 ± 0.10 | 7.99 ± 0.14 |
| $12 + \log(O/H)$ (S3O3) | 8.27 ± 0.05 | 8.25 ± 0.04 | 8.27 ± 0.04 | 8.28 ± 0.04 | 8.29 ± 0.04 | 8.29 ± 0.04 | 8.30 ± 0.04 | 8.29 ± 0.04 | 8.28 ± 0.05 | 8.26 ± 0.07 |
| $R_{S2}$ | 1.50 ± 0.03 | 1.47 ± 0.02 | 1.61 ± 0.01 | 1.69 ± 0.02 | 1.66 ± 0.01 | 1.73 ± 0.03 | 1.68 ± 0.02 | 1.70 ± 0.02 | 1.71 ± 0.04 | 1.83 ± 0.02 |
| $\log(SO_{23})$ | −0.78 ± 0.26 | −0.80 ± 0.26 | −0.78 ± 0.25 | −0.76 ± 0.25 | −0.75 ± 0.25 | −0.75 ± 0.25 | −0.74 ± 0.25 | −0.75 ± 0.24 | −0.77 ± 0.24 | −0.81 ± 0.23 |
| N2 | −1.63 ± 0.01 | −1.60 ± 0.01 | −1.56 ± 0.02 | −1.53 ± 0.03 | −1.52 ± 0.04 | −1.52 ± 0.05 | −1.51 ± 0.06 | −1.49 ± 0.08 | −1.47 ± 0.11 | −1.44 ± 0.29 |
| $\log(R_{23})$ | 0.92 ± 0.04 | 0.92 ± 0.04 | 0.92 ± 0.05 | 0.91 ± 0.05 | 0.91 ± 0.06 | 0.91 ± 0.06 | 0.91 ± 0.07 | 0.91 ± 0.08 | 0.91 ± 0.09 | 0.94 ± 0.15 |
| $\log(O_{32})$ | 0.65 ± 0.06 | 0.63 ± 0.06 | 0.59 ± 0.06 | 0.55 ± 0.06 | 0.54 ± 0.06 | 0.53 ± 0.07 | 0.52 ± 0.07 | 0.50 ± 0.08 | 0.48 ± 0.09 | 0.42 ± 0.16 |
| $\log(Ar_3O_3)$ | −1.78 ± 0.04 | −1.82 ± 0.04 | −1.81 ± 0.05 | −1.79 ± 0.06 | −1.78 ± 0.06 | −1.77 ± 0.06 | −1.76 ± 0.06 | −1.76 ± 0.07 | −1.78 ± 0.08 | −1.81 ± 0.11 |
| $\log(S_3O_3)$ | −1.15 ± 0.08 | −1.17 ± 0.06 | −1.15 ± 0.06 | −1.12 ± 0.07 | −1.11 ± 0.07 | −1.10 ± 0.07 | −1.10 ± 0.07 | −1.11 ± 0.08 | −1.12 ± 0.09 | −1.15 ± 0.12 |
| $\log(U)([S II]/[S III])$ | −1.42 ± 0.17 | −1.52 ± 0.12 | −1.53 ± 0.12 | −1.54 ± 0.13 | −1.55 ± 0.12 | −1.56 ± 0.15 | −1.58 ± 0.13 | −1.60 ± 0.14 | −1.66 ± 0.19 | −1.70 ± 0.22 |
| $\log(U)([O II]/[O III])$ | −2.50 ± 0.02 | −2.52 ± 0.02 | −2.55 ± 0.02 | −2.58 ± 0.02 | −2.59 ± 0.02 | −2.60 ± 0.02 | −2.61 ± 0.02 | −2.62 ± 0.03 | −2.64 ± 0.03 | −2.69 ± 0.06 |
| $\log(\eta')$ | 0.28 ± 0.07 | 0.25 ± 0.06 | 0.28 ± 0.06 | 0.31 ± 0.06 | 0.32 ± 0.06 | 0.32 ± 0.06 | 0.32 ± 0.07 | 0.33 ± 0.07 | 0.31 ± 0.08 | 0.35 ± 0.14 |
| $\log$ ([O III] $\lambda5007/H\beta$) | 0.70 ± 0.01 | 0.69 ± 0.01 | 0.68 ± 0.01 | 0.68 ± 0.02 | 0.67 ± 0.02 | 0.67 ± 0.02 | 0.66 ± 0.02 | 0.66 ± 0.02 | 0.66 ± 0.03 | 0.67 ± 0.04 |
| $\log$ ([N II] $\lambda6584/H\alpha$) | −1.63 ± 0.05 | −1.60 ± 0.05 | −1.56 ± 0.05 | −1.53 ± 0.06 | −1.52 ± 0.07 | −1.52 ± 0.08 | −1.51 ± 0.09 | −1.49 ± 0.10 | −1.47 ± 0.10 | −1.44 ± 0.14 |
| $\log$ ([S II] $\lambda\lambda6717,31/H\alpha$) | −1.30 ± 0.06 | −1.27 ± 0.04 | −1.24 ± 0.03 | −1.22 ± 0.03 | −1.21 ± 0.03 | −1.20 ± 0.06 | −1.19 ± 0.03 | −1.18 ± 0.03 | −1.17 ± 0.07 | −1.16 ± 0.05 |

*References.* PM03: (Pérez-Montero & Díaz 2003); G92: (Garnett 1992); H06: (Hägele et al. 2006).
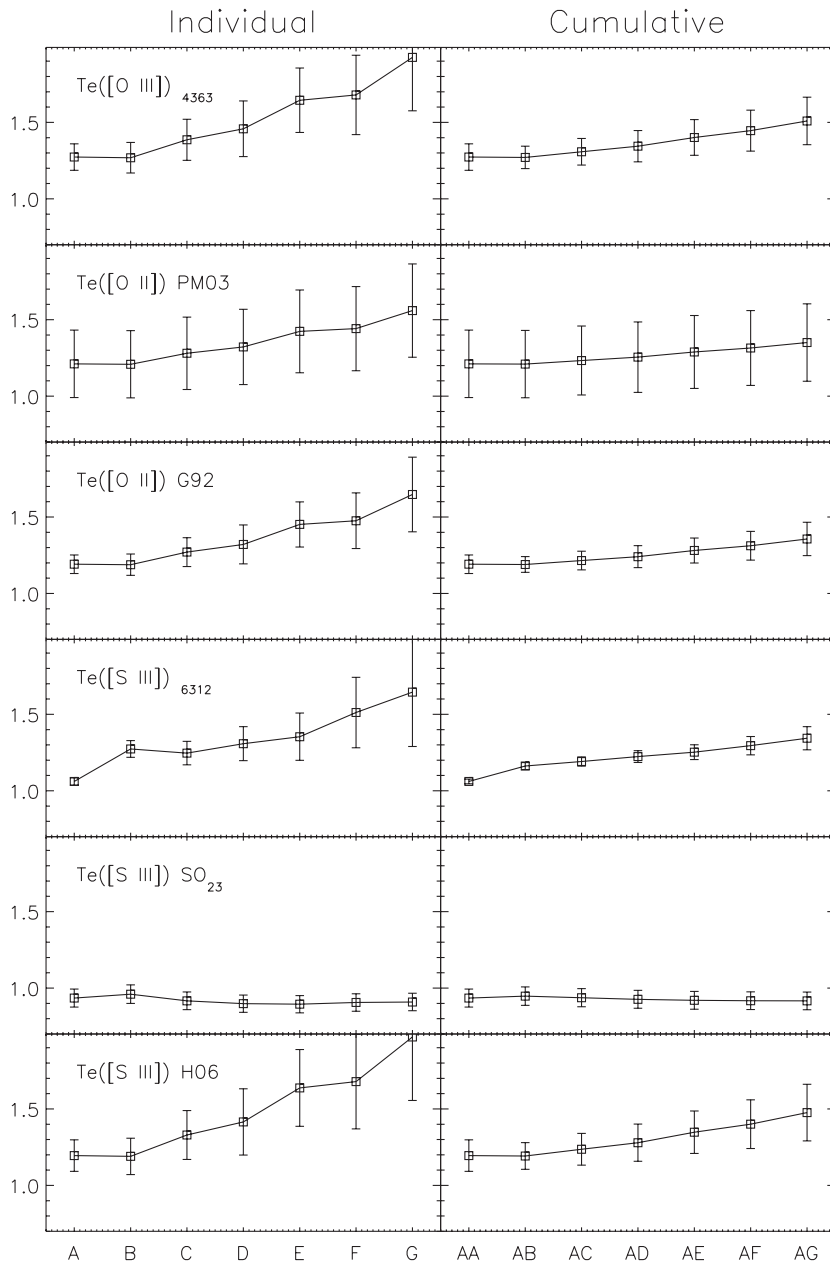
**Figure 22.** IC 132: temperatures estimated for individual and accumulated shells as labelled in each panel. The vertical lines are the associated error.

shocks or supernovae) 'escaped' the central zone and is still propagating outside. However, it may be noted that (N/O) is smoothed in the cumulative case and also becomes compatible with a constant ratio.

The empirical abundances in Fig. 26 all hint at radial increase, but again when the errors are considered all are compatible with a constant value through the region. All the indicators, except the one based on $S_3O_3$, may be set to a value of 8.0, in agreement with the mean value from the 2D maps. $S_3O_3$ reaches higher values by almost 0.25 dex even within the errors.

Fig. 27 shows the various line ratios used. $R_{S2}$ is in almost all cases above the theoretical limit for the [S II] ratio, although in the cumulative case the dispersion is lower than in the individual ones and the values are closer to the upper theoretical limit; a systematic effect that produces 'unrealistic' results is evident. When comparing

with the 2D maps, also the trend is different as the spaxels at the borders of the map have low $R_{S2}$ (~0.7). This reflects the problems with the line deblending, its dependence on the S/N or limitations in the atomic values to estimate $n_e$ in the low-density regime, as discussed previously in Section 3.1.

$\log(SO_{23})$ is constant through the region; taking into account the errors, the range lies within the fit produced by Díaz et al. (2007) for $T_e$ determination. It is worth noticing that Díaz et al. (2007) only used high-metallicity H II regions in their fit. This sets a limit $\log(SO_{23}) = -1.0$ for the validity of the relation, although many objects exist below this limit even in the compilation they present. If the fit is extended to low-metallicity objects, then it may shift the relation to produce higher temperatures. The values of $\log(R_{23})$, $\log(Ar_3O_3)$ and $\log(S_3O_3)$ are compatible, within the errors, with no gradient. The ionization sensitive ratio $\log(O_{32})$

Individual    Cumulative
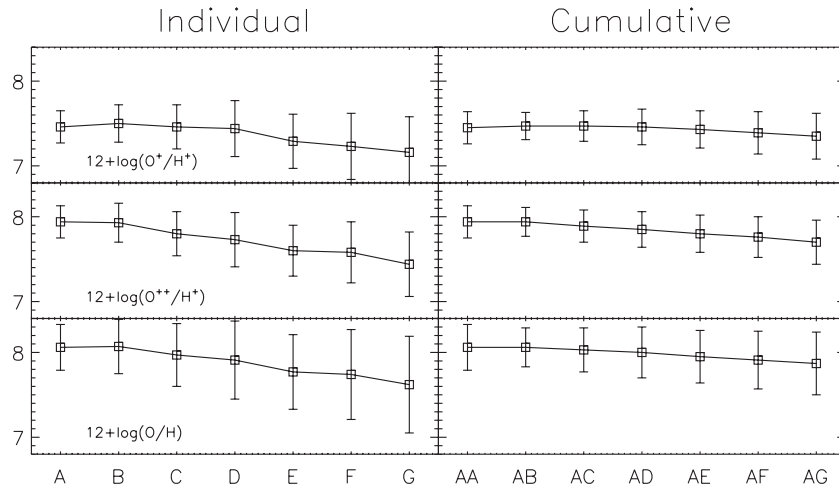


**Figure 23.** IC 132: ionic and total oxygen abundances for individual and accumulated shells.

Individual    Cumulative
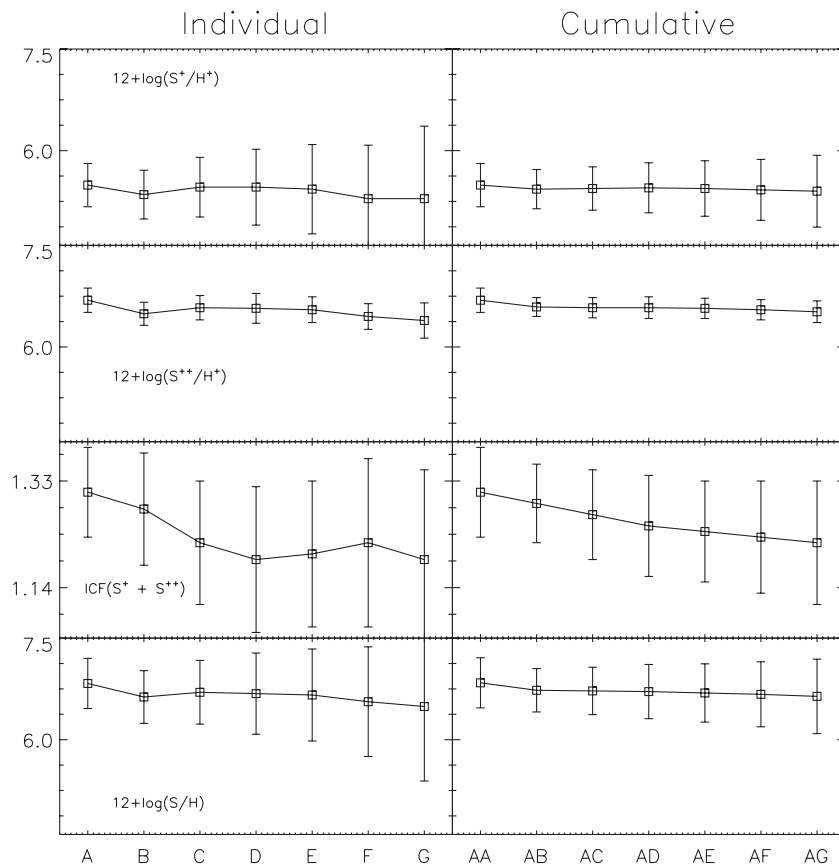


**Figure 24.** IC 132: ionic and total oxygen abundances for individual and accumulated shells.

(McGaugh 1991) indicates that the ionization decreases with radius.

Fig. 28 shows the softness parameter $\eta' = ([O\,II]\,\lambda3727/[O\,III]\,\lambda\lambda4959,5007)/([S\,II]\,\lambda\lambda6717,6731/[S\,III]\,\lambda\lambda9069,9532)$, defined by Vílchez et al. (1988) as an indicator of the effective temperature. To first order insensitive to the ionization parameter in the nebula, it grows inversely proportional to the temperature. $\eta'$ is also compatible with a constant value when errors are considered, and an increase with radius is not expected considering $T_e$ trends in Fig. 22.

Ionization sensitive ratios are plotted in Fig. 29 – a decrease of ionization with radius is concluded from the three indicators.

In general when comparing the shell analysis with the 2D maps, a statistical agreement is found between the mean of the distribution and the s.d. (*s*). However, some evident features in the maps disappear in the shell analysis. A clear example is the 'wall' that runs diagonally in the south-east section of many 2D maps for IC 132. Hence, the shell analysis must always be complemented with the maps for a full analysis of the region and exploitation of the IFS capabilities.
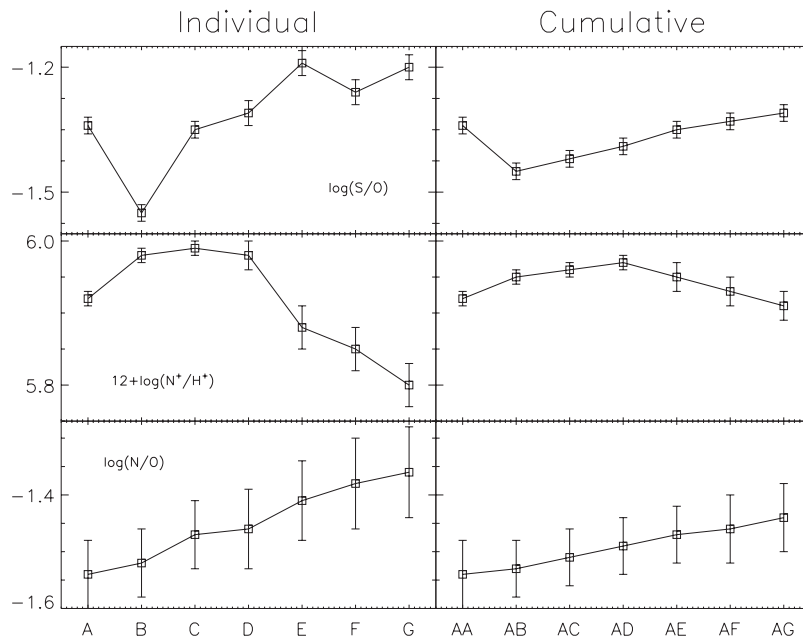
**Figure 25.** IC 132: ionic ratios and N$^+$ abundances for individual and accumulated shells.
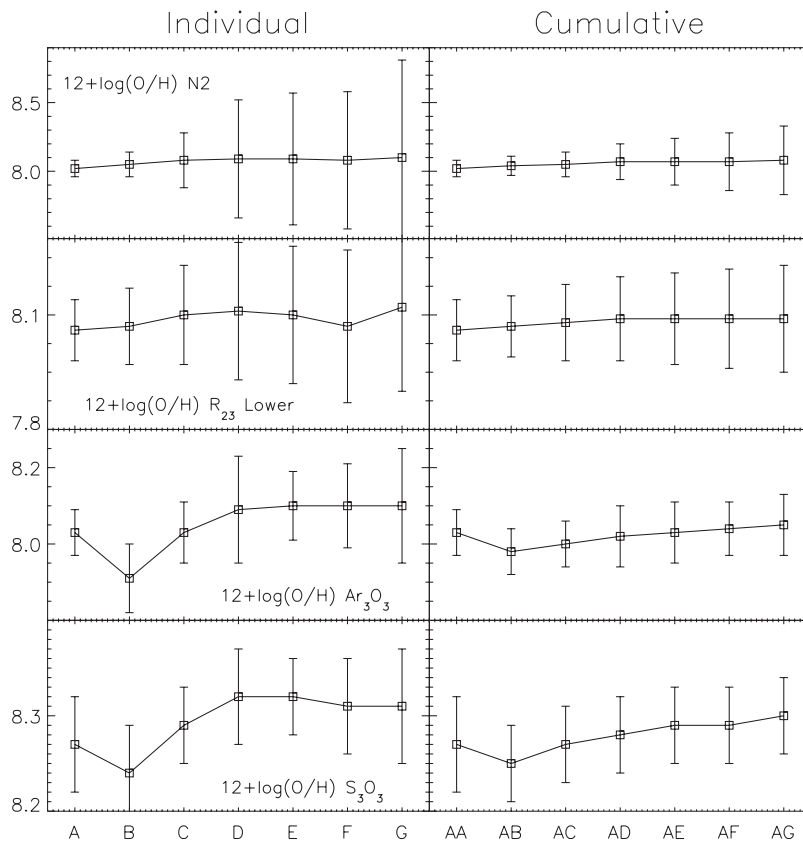


**Figure 26.** IC 132: empirical abundance indicators for individual and accumulated shells.

### 7.2  Integrated properties of the individual central regions

In contrast to the IC 132 frame that shows a single region, our observed frames in the centre of M33 contain several localized H II regions. We have used the charts from Hodge et al. (2002) to match separate regions in the Hα map. The identification of the regions

together with the number from Boulesteix et al. (1974) (which we called BCLMP) is shown in Fig. 31.

A segmentation analysis was performed for BCLMP 93; the rest of the central regions are too faint to obtain spectra with S/N high enough if segmented. The Hα levels used to measure BCLMP 93 integrated shells are shown in Fig. 32. The measured line fluxes
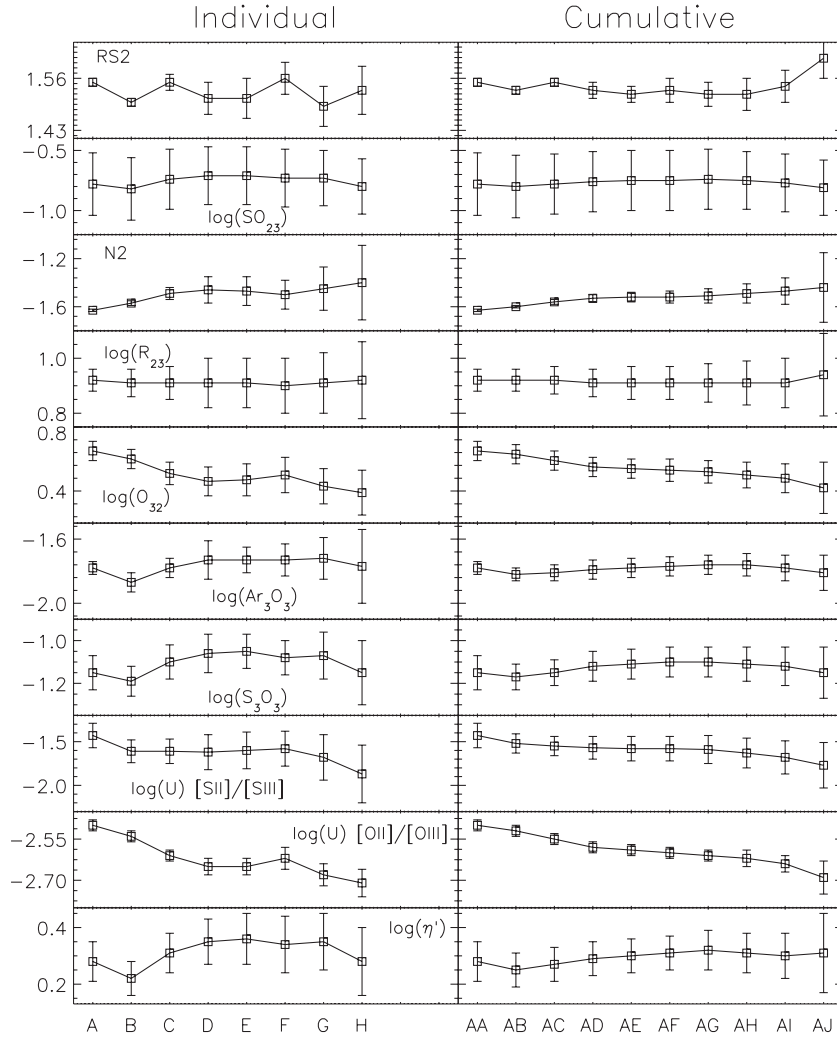
**Figure 27.** IC 132: various line ratios for individual and accumulated shells.

and derived quantities are given in Tables 8, 9, 10 and 11, while the corresponding plots are in Figs 33, 34, 35 and 36.

Fig. 33 shows a steep increase of $T_e$([S III]) for the individual shells but a moderate one for the cumulative analysis. The sulphur ionic abundances show a slight decrease with radius, although they are consistent with being uniform when errors are considered.

Empirical abundance indicators are represented in Fig. 34. N2, albeit with large errors, is compatible with constant abundance. The $R_{23}$-based abundance decreases for the individual shells but becomes compatible with constant in the cumulative case. The same can be concluded for $S_3O_3$. Within the errors, they are all compatible with being constant.

For the line ratios in Fig. 35, $R_{S2}$ is always below the low density limit indicating higher densities in the central region than in the outskirts. They show that $n_e$ values decrease with radius in the individual case, while for the cumulative shells the last point shows an increase in $n_e$ for the outermost spaxels. Even when the rest of the ratios indicate some variation trend, in general they are compatible with a constant value, except for the last two ratios. The $\log(U)_{[O II]/[O III]}$ increases while $\eta'$ decreases. The decrease in $\eta'$ is compatible with the trend displayed by $T_e$([S III]) in Fig. 33.

All the ionization sensitive ratios in Fig. 36 show a clear increase with radius. This is puzzling, as one would expect that when [O III]/H$\beta$ increases, both [N II]/H$\alpha$ and [S II]/H$\alpha$ should decrease. Possible causes may be a projection effect of two zones physically separated but on the same line of sight or in general, multiplicity of the region or even the meddling effect of diffuse radiation.

The large error bars in some line ratio plots are a consequence of the relatively small S/N of the data. We can nevertheless distinguish some differences between IC 132 and BCLMP 93. First, the higher Balmer decrement $C$(H$\beta$) and smaller EW(H$\beta$) in BCLMP 93, shown in Fig. 37, indicate higher extinction and either an older H II region or, more likely, a larger contamination due to the underlying stellar population unrelated to the ionizing cluster in the central regions of M33, i.e. the bulge population. Regarding the electron temperatures, only $T_e$([S III])$_{6312}$ is computed for both regions and provides a result that suggests an outward increasing temperature for each region.

Due to the radial decrease in the ionization parameter, we expect to observe a radial decrease in ionization; IC 132 (Fig. 29) shows a decreasing [O III]/H$\beta$ and increasing [N II]/H$\alpha$ and [SII]/H$\alpha$, but in
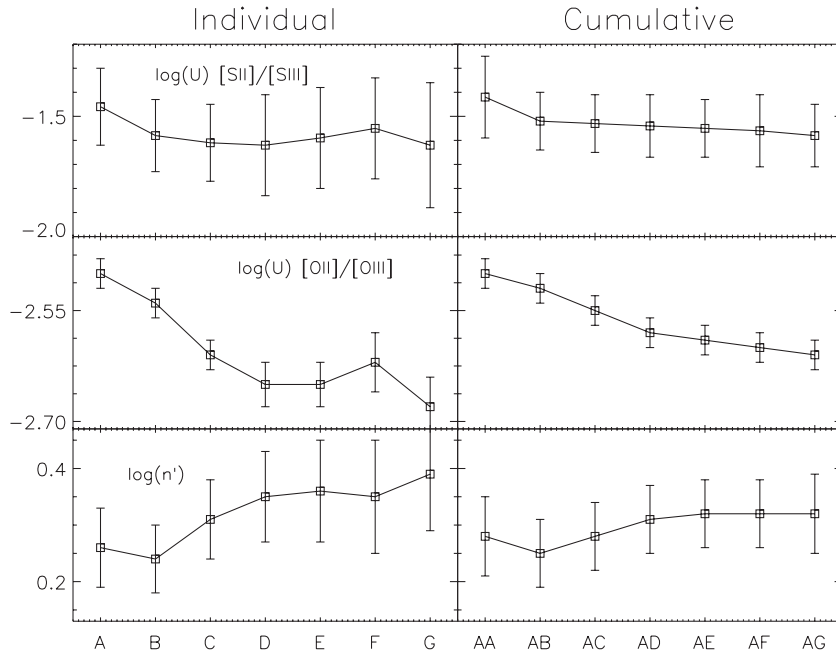
**Figure 28.** IC 132: ionization parameter from sulphur and oxygen and the parameter $\eta'$ (see text) for individual and accumulated shells.
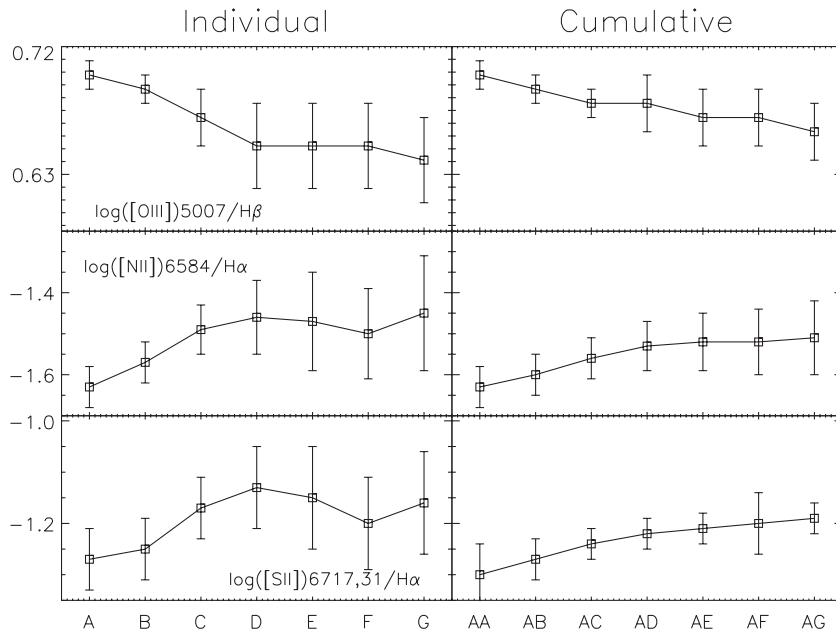


**Figure 29.** IC 132: ionization sensitive line ratios for individual and accumulated shells.

BCLMP 93 (Fig. 36) these line ratios seem to increase outwards. We have already discussed a possible explanation due to confusion in the central region.

## 8  CONCLUSIONS

The main objective of this work was to study with spatially resolved spectroscopy the differences in the characteristics between the innermost and outermost regions of star formation in nearby spiral galaxies with the aim of exploring the differences in the properties of intense star formation activity in widely contrasting environments.

We have presented the results of our IFS data obtained with PMAS in PPak mode at the CAHA 3.5-m telescope, of H II regions in M33, selected to cover a wide range in environment and properties of the star-forming regions. Our sample includes the luminous H II region IC 132 in the outer disc and the innermost H II regions in a field of $500 \times 300 \, pc^2$ that surrounds the galaxy centre. The results are presented in the form of intensity maps of the H II region intrinsic parameters: line ratios, excitation, extinction, electron density, electron temperatures and elemental abundances with a sampling of $1 \times 1 \, arcsec^2$. We also studied internal gradients of the intrinsic parameters of the H II regions for apertures or shells defined according to their average surface brightness in H$\alpha$.
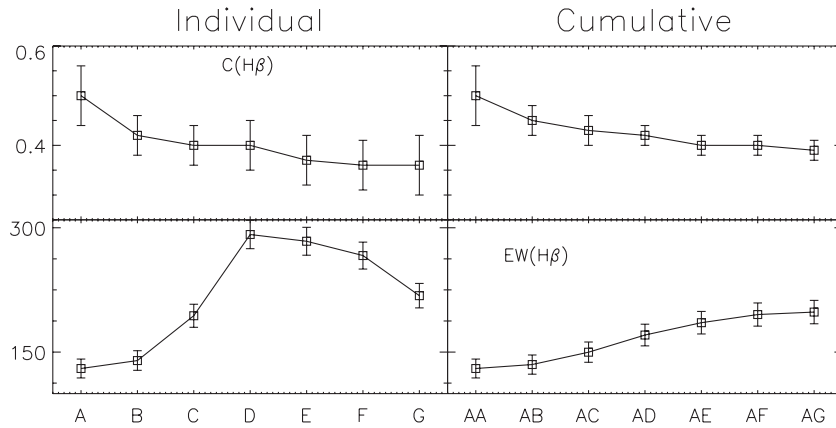
**Figure 30.** IC 132: extinction parameter $C(\mathrm{H}\beta)$ and equivalent width $\mathrm{EW}(\mathrm{H}\beta)$ for individual and accumulated shells.
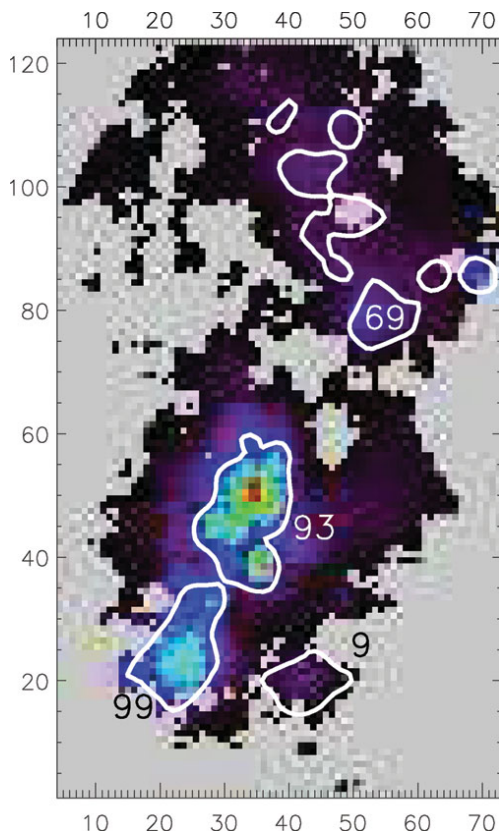


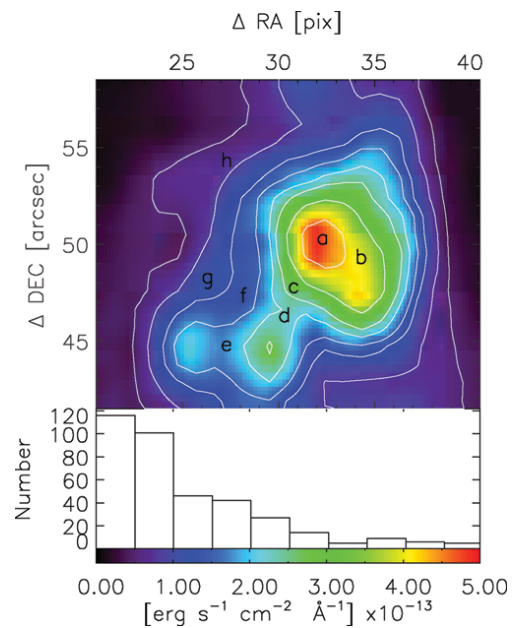**Figure 31.** Identification of regions from the (Hodge et al. 2002) catalogue. The labels are the BCLMP numbers (see text).



**Figure 32.** BCLMP 93 shell segmentation.

Our main findings are as follows:

(i) *Extinction*. We find a clear difference in the extinction and its radial gradient between the innermost and outer regions in M33. While IC 132 shows a global value of $C(\mathrm{H}\beta)$ of about 0.3 and indications of lower extinction at larger radius, $C(\mathrm{H}\beta)$ for BCLMP 93 is globally around 1.3, decreasing outwards in the region.

(ii) *Equivalent widths and ages*. In both systems, the $\mathrm{EW}(\mathrm{H}\beta)$ is smaller in the centre of the region and grows to a maximum in the intermediate shells before dropping in the outer shells. The radial behaviour of the $\mathrm{EW}(\mathrm{H}\beta)$ can be understood by a combination of factors: first, the continuum in the inner regions is strongly affected by the massive ionizing stars; secondly, the outer regions are af-

fected by the disc (IC 132) or bulge (BCLMP 93) component and globally the brightness of the emission lines decreases radially outwards. Thus, the $\mathrm{EW}(\mathrm{H}\beta)$ is probably peaking in the transition zone between the edge of the ionizing cluster and the regions where the surface brightness of $\mathrm{H}\beta$ drops below that of the older population.

We find a smaller equivalent width of $\mathrm{H}\beta$ in BCLMP 93 than in IC 132 indicating higher extinction and either an older H II region or more likely a larger contamination due to the presence of an old stellar population in the central regions of M33, i.e. the bulge population.

It is interesting to note that the maximum $\mathrm{EW}(\mathrm{H}\beta) \sim 300$ Å in IC 132 is close to the maximum of $\sim 400$ Å for STARBURST99 models (Leitherer et al. 1999), assuming instantaneous star formation with the upper mass limit $= 100\,\mathrm{M}_\odot$, zero-age main sequence, an initial mass function with $\alpha = 2.35$ and $Z = 0.020\,\mathrm{Z}_\odot$. The asymptotic maximum of the cumulative $\mathrm{EW}(\mathrm{H}\beta)$ reaches $\sim 200$ Å indicating an ionizing cluster with an age of less than 3 Myr that is in agreement with the detection of WN stars that are expected to appear after 2.5 Myr of evolution of a young massive cluster.

**Table 8.** Reddening-corrected fluxes for BCLMP 93 with integration over individual Hα shells. Lines are normalized to Hβ = 100.

| λ | Ion | Individual | | | | | | | |
|---|---|---|---|---|---|---|---|---|---|
| | | A | B | C | D | E | F | G | H |
| 3727 | [O II] | 160.7 ± 11.4 | 183.9 ± 12.6 | 230.8 ± 21.4 | 232.2 ± 18.9 | 235.0 ± 24.4 | 244.8 ± 21.9 | 264.8 ± 25.1 | 294.7 ± 52.4 |
| 4010 | Hδ | 23.4 ± 3.2 | 24.3 ± 3.2 | 21.4 ± 4.5 | 21.2 ± 5.5 | 21.0 ± 5.1 | 21.0 ± 5.9 | 17.4 ± 7.1 | 13.8 ± 11.7 |
| 4340 | Hγ | 43.0 ± 2.3 | 43.3 ± 2.0 | 42.3 ± 3.0 | 43.0 ± 2.9 | 41.6 ± 3.5 | 43.0 ± 4.4 | 41.7 ± 5.1 | 41.3 ± 9.5 |
| 4363 | [O III][a] | − 4.6 ± 1.3 | − 4.0 ± 1.4 | − 5.8 ± 2.0 | − 4.9 ± 1.9 | − 5.9 ± 2.1 | − 7.8 ± 2.5 | − 12.6 ± 2.9 | − 21.3 ± 4.6 |
| 4861 | [Hβ] | 100.0 ± 3.5 | 100.0 ± 3.4 | 100.0 ± 5.2 | 100.0 ± 4.7 | 100.0 ± 4.8 | 100.0 ± 5.5 | 100.0 ± 7.0 | 100.0 ± 10.8 |
| 4959 | [O III] | 2.4 ± 1.0 | 2.0 ± 1.2 | 3.6 ± 1.6 | 4.4 ± 1.5 | 4.9 ± 1.3 | 6.6 ± 1.9 | 9.5 ± 2.9 | 15.2 ± 3.8 |
| 5007 | [O III] | 9.4 ± 0.8 | 7.9 ± 0.9 | 11.1 ± 1.2 | 11.4 ± 1.3 | 13.5 ± 1.4 | 18.0 ± 2.0 | 22.1 ± 2.6 | 35.3 ± 4.0 |
| 6312 | [S III] | 1.3 ± 0.9 | 1.3 ± 1.1 | 1.3 ± 1.3 | 1.8 ± 1.7 | 2.1 ± 2.1 | 2.8 ± 2.7 | 3.5 ± 3.7 | 5.0 ± 5.7 |
| 6548 | [N II] | 10.1 ± 1.2 | 11.0 ± 1.5 | 11.8 ± 1.5 | 13.3 ± 1.5 | 12.0 ± 1.4 | 12.2 ± 1.2 | 13.2 ± 2.0 | 12.6 ± 3.5 |
| 6564 | Hα | 283.8 ± 7.6 | 283.8 ± 7.5 | 281.2 ± 10.8 | 280.1 ± 10.1 | 282.3 ± 10.1 | 282.2 ± 11.2 | 284.8 ± 14.8 | 282.3 ± 22.6 |
| 6584 | [N II] | 55.5 ± 2.1 | 59.0 ± 2.4 | 66.0 ± 3.2 | 68.6 ± 3.3 | 68.0 ± 3.1 | 66.8 ± 3.1 | 69.0 ± 4.4 | 68.9 ± 6.9 |
| 6717 | [S II] | 25.0 ± 1.3 | 30.2 ± 1.4 | 35.5 ± 2.0 | 38.2 ± 2.2 | 40.0 ± 2.4 | 41.4 ± 2.6 | 44.5 ± 3.2 | 52.1 ± 5.3 |
| 6731 | [S II] | 23.3 ± 1.1 | 24.3 ± 1.2 | 28.2 ± 1.6 | 29.2 ± 1.8 | 31.0 ± 2.0 | 32.4 ± 2.1 | 34.2 ± 2.6 | 38.6 ± 4.1 |
| 7136 | [Ar III] | 0.6 ± 7.1 | 0.7 ± 4.6 | 1.4 ± 6.5 | 1.3 ± 9.3 | 1.7 ± 10.9 | 2.2 ± 11.9 | 2.2 ± 10.3 | 8.3 ± 13.5 |
| 9068 | [S III] | 27.1 ± 14.4 | 29.0 ± 20.7 | 31.7 ± 25.3 | 32.6 ± 30.6 | 32.9 ± 32.9 | 30.3 ± 32.6 | 26.8 ± 35.1 | 15.7 ± 44.6 |
| $I(H\beta)$ (erg s$^{-1}$ cm$^{-2}$ 10$^{-13}$) | | 21.28 ± 0.05 | 18.95 ± 0.05 | 18.61 ± 0.07 | 18.66 ± 0.06 | 18.48 ± 0.06 | 18.08 ± 0.07 | 18.25 ± 0.09 | 18.63 ± 0.14 |
| $C(H\beta)$ | | 0.66 ± 0.06 | 0.52 ± 0.06 | 0.68 ± 0.08 | 0.84 ± 0.07 | 1.02 ± 0.07 | 1.24 ± 0.08 | 1.25 ± 0.09 | 1.08 ± 0.11 |
| EW(Hβ) (Å) | | 38.08 ± 6.17 | 46.96 ± 6.85 | 47.47 ± 6.89 | 55.80 ± 7.47 | 50.28 ± 7.09 | 48.44 ± 6.96 | 42.13 ± 6.49 | 33.43 ± 5.78 |

[a]Contaminated by mercury street lamps.

**Table 9.** Integrated temperatures, abundances and line ratios for BCLMP 93 individual Hα shells.

| | Individual | | | | | | | |
|---|---|---|---|---|---|---|---|---|
| | A | B | C | D | E | F | G | H |
| $T_e$([S III])$_{6312}$ | 8000 ± 200 | 8000 ± 200 | 7600 ± 300 | 8400 ± 400 | 9100 ± 500 | 10300 ± 700 | 12400 ± 1100 | 16000 ± 2700 |
| $T_e$([S III])$_{SO_{23}}$ | 6000 ± 300 | 6100 ± 300 | 6200 ± 300 | 6200 ± 300 | 6200 ± 300 | 6300 ± 300 | 6500 ± 400 | 6700 ± 400 |
| 12+log(S$^+$/H$^+$) | 6.34 ± 0.66 | 6.38 ± 0.91 | 6.50 ± 1.05 | 6.39 ± 1.26 | 6.32 ± 1.38 | 6.20 ± 1.55 | 6.05 ± 1.95 | 5.90 ± 3.04 |
| 12+log(S$^{++}$/H$^+$) | 6.93 ± 0.42 | 6.96 ± 0.59 | 7.04 ± 0.68 | 6.95 ± 0.80 | 6.86 ± 0.86 | 6.74 ± 0.94 | 6.54 ± 1.11 | 6.33 ± 1.57 |
| 12+log(O/H) (N2) | 8.45 ± 0.81 | 8.47 ± 0.90 | 8.51 ± 2.25 | 8.53 ± 2.10 | 8.52 ± 2.07 | 8.51 ± 2.48 | 8.52 ± 4.50 | 8.53 ± 10.60 |
| 12+log(O/H) ($R_{23upper}$) | 8.92 ± 0.10 | 8.87 ± 0.10 | 8.75 ± 0.10 | 8.75 ± 0.10 | 8.75 ± 0.10 | 8.73 ± 0.10 | 8.69 ± 0.10 | 8.63 ± 0.10 |
| 12+log(O/H) (Ar$_3$O$_3$) | 8.55 ± 2.16 | 8.63 ± 0.89 | 8.67 ± 0.57 | 8.67 ± 0.85 | 8.68 ± 0.74 | 8.67 ± 0.64 | 8.64 ± 0.64 | 8.75 ± 0.13 |
| 12+log(O/H) (S$_3$O$_3$) | 8.88 ± 0.07 | 8.92 ± 0.11 | 8.88 ± 0.12 | 8.87 ± 0.14 | 8.84 ± 0.14 | 8.80 ± 0.13 | 8.75 ± 0.14 | 8.69 ± 0.19 |
| $R_{S2}$ | 1.07 ± 0.01 | 1.24 ± 0.01 | 1.26 ± 0.01 | 1.31 ± 0.01 | 1.29 ± 0.01 | 1.28 ± 0.01 | 1.30 ± 0.01 | 1.35 ± 0.02 |
| $n_e$ | 328 – | 137 – | 127 – | 85 – | 101 – | 109 – | 91 – | 55 – |
| log (SO$_{23}$) | − 0.01 ± 0.03 | − 0.03 ± 0.03 | − 0.09 ± 0.03 | − 0.08 ± 0.03 | − 0.09 ± 0.03 | − 0.12 ± 0.04 | − 0.18 ± 0.04 | − 0.24 ± 0.06 |
| N2 | − 0.71 ± 0.11 | − 0.68 ± 0.12 | − 0.63 ± 0.27 | − 0.61 ± 0.25 | − 0.62 ± 0.25 | − 0.63 ± 0.30 | − 0.62 ± 0.53 | − 0.61 ± 1.25 |
| log ($R_{23}$) | 0.24 ± 0.08 | 0.29 ± 0.07 | 0.39 ± 0.10 | 0.39 ± 0.09 | 0.40 ± 0.11 | 0.43 ± 0.10 | 0.47 ± 0.11 | 0.54 ± 0.19 |
| log (O$_{32}$) | − 1.13 ± 0.13 | − 1.27 ± 0.17 | − 1.20 ± 0.16 | − 1.17 ± 0.15 | − 1.11 ± 0.15 | − 1.00 ± 0.14 | − 0.92 ± 0.16 | − 0.77 ± 0.21 |
| log (Ar$_3$O$_3$) | − 1.19 ± 3.97 | − 1.03 ± 2.11 | − 0.91 ± 1.64 | − 0.93 ± 2.38 | − 0.90 ± 2.19 | − 0.91 ± 1.84 | − 1.00 ± 1.60 | − 0.63 ± 0.56 |
| log (S$_3$O$_3$) | 0.56 ± 0.18 | 0.65 ± 0.26 | 0.54 ± 0.30 | 0.54 ± 0.35 | 0.45 ± 0.37 | 0.32 ± 0.41 | 0.18 ± 0.48 | − 0.05 ± 0.68 |
| log ($U$)([S II]/[S III]) | − 2.33 ± 0.31 | − 2.39 ± 0.43 | − 2.44 ± 0.50 | − 2.47 ± 0.59 | − 2.53 ± 0.63 | − 2.57 ± 0.68 | − 2.70 ± 0.81 | − 2.85 ± 1.15 |
| log ($U$)([O II]/[O III]) | − 3.93 ± 0.05 | − 4.03 ± 0.06 | − 3.98 ± 0.06 | − 3.95 ± 0.05 | − 3.91 ± 0.05 | − 3.82 ± 0.05 | − 3.76 ± 0.05 | − 3.63 ± 0.07 |
| log ($\eta'$) | 1.52 ± 0.11 | 1.63 ± 0.13 | 1.52 ± 0.15 | 1.48 ± 0.16 | 1.38 ± 0.17 | 1.25 ± 0.17 | 1.09 ± 0.17 | 0.85 ± 0.24 |
| log ([O III] λ5007/Hβ) | − 1.03 ± 0.04 | − 1.10 ± 0.05 | − 0.95 ± 0.05 | − 0.94 ± 0.05 | − 0.87 ± 0.05 | − 0.74 ± 0.05 | − 0.65 ± 0.05 | − 0.45 ± 0.05 |
| log ([N II] λ6584/Hα) | − 0.71 ± 0.01 | − 0.68 ± 0.02 | − 0.63 ± 0.01 | − 0.61 ± 0.02 | − 0.62 ± 0.01 | − 0.63 ± 0.01 | − 0.62 ± 0.02 | − 0.61 ± 0.03 |
| log ([S II] λλ6717,31/Hα) | − 0.77 ± 0.07 | − 0.72 ± 0.08 | − 0.64 ± 0.08 | − 0.62 ± 0.08 | − 0.60 ± 0.08 | − 0.58 ± 0.09 | − 0.56 ± 0.09 | − 0.49 ± 0.09 |

For BCLMP 93 the same procedure suggests an upper limit for the age of the cluster of about 5 Myr, bearing in mind that the large contamination due to the underlying bulge population precludes a more precise age estimate. This age makes the central region older than IC 132 and could explain the lack of present-day WR features in the region.

(iii) *Electron density.* The electron density ($n_e$) was estimated from the RS2 = [S II] λ6717/[S II] λ6731 line ratio after deblending the doublet. This diagnostic situates the H II regions in the low density limit. Even if an exact value for $n_e$ is not possible, a variation in the ratio with position is observed, supporting the fact that to assume a single $n_e$ value to characterize a whole H II region is too simplistic. Better spectral resolution, access to alternative density diagnostics and revision of the theoretical estimation based on new atomic data for collisional strengths are necessary to shed light on the subject.

**Table 10.** Reddening-corrected fluxes for BCLMP 93 with integration over cumulative Hα shells. Lines are normalized to Hβ = 100.

| | | | | | Cumulative | | | |
|---|---|---|---|---|---|---|---|---|
| | | $\overline{AA}$ | $\overline{AB}$ | $\overline{AC}$ | $\overline{AD}$ | $\overline{AE}$ | $\overline{AF}$ | $\overline{AG}$ | $\overline{AH}$ |
| 3727 | [O II] | 160.7 ± 11.4 | 171.6 ± 11.4 | 190.3 ± 13.8 | 200.4 ± 14.1 | 207.1 ± 14.7 | 213.1 ± 15.2 | 220.2 ± 16.1 | 229.4 ± 17.7 |
| 4010 | Hδ | 23.4 ± 3.2 | 23.8 ± 3.1 | 23.0 ± 3.1 | 22.6 ± 3.5 | 22.3 ± 3.7 | 22.0 ± 3.9 | 21.4 ± 4.2 | 20.4 ± 4.9 |
| 4340 | Hγ | 43.0 ± 2.3 | 43.1 ± 2.1 | 42.9 ± 2.1 | 42.9 ± 2.2 | 42.6 ± 2.3 | 42.7 ± 2.5 | 42.6 ± 2.6 | 42.4 ± 3.2 |
| 4363 | [O III]$^a$ | − 4.6 ± 1.3 | − 4.3 ± 1.3 | − 4.8 ± 1.4 | − 4.8 ± 1.4 | − 5.1 ± 1.5 | − 5.5 ± 1.6 | − 6.4 ± 1.7 | − 8.1 ± 2.0 |
| 4861 | [Hβ] | 100.0 ± 3.5 | 100.0 ± 3.4 | 100.0 ± 3.7 | 100.0 ± 3.9 | 100.0 ± 3.9 | 100.0 ± 4.1 | 100.0 ± 4.4 | 100.0 ± 5.0 |
| 4959 | [O III] | 2.4 ± 1.0 | 2.2 ± 1.1 | 2.7 ± 1.1 | 3.1 ± 1.2 | 3.4 ± 1.2 | 3.9 ± 1.2 | 4.7 ± 1.4 | 6.0 ± 1.6 |
| 5007 | [O III] | 9.4 ± 0.8 | 8.7 ± 0.8 | 9.5 ± 0.9 | 9.9 ± 0.9 | 10.6 ± 1.0 | 11.8 ± 1.1 | 13.2 ± 1.2 | 15.9 ± 1.3 |
| 6312 | [S III] | 1.3 ± 0.9 | 1.3 ± 1.0 | 1.3 ± 1.1 | 1.4 ± 1.2 | 1.5 ± 1.4 | 1.7 ± 1.6 | 2.0 ± 1.9 | 2.4 ± 2.4 |
| 6548 | [N II] | 10.1 ± 1.2 | 10.5 ± 1.3 | 11.1 ± 1.3 | 11.4 ± 1.3 | 11.5 ± 1.3 | 11.5 ± 1.2 | 11.8 ± 1.3 | 11.9 ± 1.5 |
| 6564 | Hα | 283.8 ± 7.6 | 283.8 ± 7.4 | 283.0 ± 8.0 | 282.3 ± 8.3 | 282.3 ± 8.4 | 282.3 ± 8.6 | 282.6 ± 9.2 | 282.6 ± 10.5 |
| 6584 | [N II] | 55.5 ± 2.1 | 57.1 ± 2.2 | 60.0 ± 2.4 | 62.1 ± 2.5 | 63.2 ± 2.5 | 63.8 ± 2.5 | 64.5 ± 2.7 | 65.0 ± 3.1 |
| 6717 | [S II] | 25.7 ± 1.3 | 28.8 ± 1.3 | 30.6 ± 1.4 | 32.3 ± 1.5 | 33.6 ± 1.6 | 34.7 ± 1.7 | 34.6 ± 1.8 | 38.2 ± 2.1 |
| 6731 | [S II] | 23.7 ± 1.1 | 23.1 ± 1.1 | 24.2 ± 1.1 | 25.7 ± 1.2 | 26.7 ± 1.3 | 27.0 ± 1.4 | 29.9 ± 1.5 | 29.5 ± 1.7 |
| 7136 | [Ar III] | 0.6 ± 7.1 | 0.7 ± 5.6 | 1.0 ± 3.8 | 1.0 ± 3.8 | 1.1 ± 4.7 | 1.3 ± 5.6 | 1.4 ± 6.1 | 1.7 ± 6.9 |
| 9068 | [S III] | 27.1 ± 14.4 | 27.7 ± 17.2 | 28.8 ± 19.5 | 29.9 ± 22.0 | 30.7 ± 24.0 | 30.7 ± 25.1 | 30.1 ± 26.5 | 29.8 ± 29.1 |
| $I(H\beta)$ | | 21.28 ± 0.05 | 40.23 ± 0.10 | 58.83 ± 0.16 | 77.49 ± 0.21 | 95.97 ± 0.27 | 114.05 ± 0.33 | 132.30 ± 0.41 | 150.92 ± 0.53 |
| (erg s$^{-1}$ cm$^{-2}$ 10$^{-13}$) | | | | | | | | | |
| $C(H\beta)$ | | 0.66 ± 0.06 | 0.60 ± 0.04 | 0.62 ± 0.04 | 0.68 ± 0.03 | 0.75 ± 0.03 | 0.83 ± 0.03 | 0.89 ± 0.03 | 0.92 ± 0.03 |
| EW(Hβ) (Å) | | 38.08 ± 6.17 | 41.80 ± 6.47 | 43.44 ± 6.59 | 45.89 ± 6.77 | 46.67 ± 6.83 | 46.94 ± 6.85 | 46.21 ± 6.80 | 44.13 ± 6.64 |

$^a$Contaminated by mercury street lamps.

**Table 11.** Integrated temperatures, abundances and line ratios for BCLMP 93 accumulated Hα shells.

| | | | | Cumulative | | | | |
|---|---|---|---|---|---|---|---|---|
| | $\overline{AA}$ | $\overline{AB}$ | $\overline{AC}$ | $\overline{AD}$ | $\overline{AE}$ | $\overline{AF}$ | $\overline{AG}$ | $\overline{AH}$ |
| $T_e([S III])_{6312}$ | 8000 ± 200 | 8000 ± 200 | 7900 ± 200 | 8000 ± 300 | 8200 ± 300 | 8600 ± 300 | 9100 ± 400 | 9900 ± 500 |
| $T_e([S III])_{SO_{23}}$ | 6000 ± 300 | 6000 ± 300 | 6100 ± 300 | 6100 ± 300 | 6200 ± 300 | 6200 ± 300 | 6200 ± 300 | 6300 ± 300 |
| $12 + \log(S^+/H^+)$ | 6.35 ± 0.66 | 6.35 ± 0.77 | 6.39 ± 0.86 | 6.39 ± 0.96 | 6.37 ± 1.03 | 6.33 ± 1.10 | 6.29 ± 1.21 | 6.21 ± 1.36 |
| $12 + \log(S^{++}/H^+)$ | 6.93 ± 0.42 | 6.95 ± 0.50 | 6.97 ± 0.56 | 6.96 ± 0.62 | 6.94 ± 0.66 | 6.90 ± 0.70 | 6.84 ± 0.75 | 6.76 ± 0.83 |
| $12 + \log(O/H)$ (N2) | 8.45 ± 0.81 | 8.46 ± 0.82 | 8.48 ± 1.05 | 8.49 ± 1.19 | 8.49 ± 1.25 | 8.50 ± 1.33 | 8.50 ± 1.56 | 8.50 ± 2.06 |
| $12 + \log(O/H)$ ($R_{23upper}$) | 8.92 ± 0.10 | 8.90 ± 0.10 | 8.85 ± 0.10 | 8.83 ± 0.10 | 8.81 ± 0.10 | 8.80 ± 0.10 | 8.79 ± 0.10 | 8.77 ± 0.10 |
| $12 + \log(O/H)$ ($Ar_3O_3$) | 8.55 ± 2.16 | 8.61 ± 1.18 | 8.64 ± 0.53 | 8.64 ± 0.53 | 8.65 ± 0.55 | 8.65 ± 0.56 | 8.65 ± 0.57 | 8.65 ± 0.52 |
| $12 + \log(O/H)$ ($S_3O_3$) | 8.88 ± 0.07 | 8.90 ± 0.09 | 8.89 ± 0.10 | 8.89 ± 0.11 | 8.88 ± 0.11 | 8.86 ± 0.12 | 8.84 ± 0.12 | 8.81 ± 0.12 |
| $R_{S2}$ | 1.08 ± 0.01 | 1.25 ± 0.01 | 1.27 ± 0.01 | 1.26 ± 0.01 | 1.26 ± 0.01 | 1.28 ± 0.01 | 1.16 ± 0.01 | 1.30 ± 0.01 |
| $n_e$ | 312 – | 133 – | 119 – | 127 – | 122 – | 103 – | 224 – | 95 – |
| $\log(SO_{23})$ | − 0.01 ± 0.03 | − 0.02 ± 0.03 | − 0.05 ± 0.03 | − 0.06 ± 0.03 | − 0.07 ± 0.03 | − 0.08 ± 0.03 | − 0.09 ± 0.03 | − 0.11 ± 0.04 |
| N2 | − 0.71 ± 0.11 | − 0.70 ± 0.11 | − 0.67 ± 0.14 | − 0.66 ± 0.15 | − 0.65 ± 0.16 | − 0.65 ± 0.17 | − 0.64 ± 0.19 | − 0.64 ± 0.25 |
| $\log(R_{23})$ | 0.24 ± 0.08 | 0.26 ± 0.07 | 0.31 ± 0.08 | 0.33 ± 0.08 | 0.34 ± 0.08 | 0.36 ± 0.08 | 0.38 ± 0.08 | 0.40 ± 0.09 |
| $\log(O_{32})$ | − 1.13 ± 0.13 | − 1.20 ± 0.14 | − 1.20 ± 0.14 | − 1.19 ± 0.14 | − 1.17 ± 0.13 | − 1.13 ± 0.13 | − 1.09 ± 0.13 | − 1.02 ± 0.12 |
| $\log(Ar_3O_3)$ | − 1.19 ± 3.97 | − 1.07 ± 2.62 | − 0.99 ± 1.34 | − 1.00 ± 1.32 | − 0.98 ± 1.43 | − 0.97 ± 1.49 | − 0.97 ± 1.49 | − 0.97 ± 1.38 |
| $\log(S_3O_3)$ | 0.56 ± 0.18 | 0.60 ± 0.22 | 0.57 ± 0.24 | 0.56 ± 0.27 | 0.54 ± 0.29 | 0.50 ± 0.30 | 0.44 ± 0.32 | 0.35 ± 0.36 |
| $\log(U)([S II]/[S III])$ | − 2.35 ± 0.31 | − 2.37 ± 0.36 | − 2.39 ± 0.41 | − 2.42 ± 0.45 | − 2.44 ± 0.48 | − 2.45 ± 0.51 | − 2.49 ± 0.55 | − 2.54 ± 0.61 |
| $\log(U)([O II]/[O III])$ | − 3.93 ± 0.05 | − 3.98 ± 0.05 | − 3.98 ± 0.05 | − 3.97 ± 0.05 | − 3.95 ± 0.04 | − 3.93 ± 0.04 | − 3.89 ± 0.04 | − 3.84 ± 0.04 |
| $\log(\eta')$ | 1.52 ± 0.11 | 1.56 ± 0.12 | 1.55 ± 0.13 | 1.53 ± 0.13 | 1.50 ± 0.14 | 1.45 ± 0.14 | 1.39 ± 0.14 | 1.29 ± 0.15 |
| $\log([O III] \lambda 5007/H\beta)$ | − 1.03 ± 0.04 | − 1.06 ± 0.04 | − 1.02 ± 0.04 | − 1.00 ± 0.04 | − 0.97 ± 0.04 | − 0.93 ± 0.04 | − 0.88 ± 0.04 | − 0.80 ± 0.04 |
| $\log([N II] \lambda 6584/H\alpha)$ | − 0.71 ± 0.01 | − 0.70 ± 0.01 | − 0.67 ± 0.01 | − 0.66 ± 0.01 | − 0.65 ± 0.01 | − 0.65 ± 0.01 | − 0.64 ± 0.01 | − 0.64 ± 0.01 |
| $\log([S II] \lambda\lambda 6717,31/H\alpha)$ | − 0.76 ± 0.07 | − 0.74 ± 0.04 | − 0.71 ± 0.03 | − 0.69 ± 0.02 | − 0.67 ± 0.02 | − 0.66 ± 0.02 | − 0.64 ± 0.02 | − 0.62 ± 0.02 |

(iv) *Electron temperature.* For the central zone of IC 132, the electron temperature ($T_e$) was estimated from the detected [O III] λ4363 and [S III] λ6312 lines allowing the use of the [O III] λλ4959,5007/[O III] λ4363 and [S III] λλ9069,9532/[S III] λ6013 ratios to compute $T_e$([O III]) and $T_e$([S III]), respectively. For BCLMP 93 the lack of detection of [O III] λ4363 implies that only $T_e$([S III]) was determined in its central zone. The blueshift of the galaxy means that the [O III] λ4363 line is only an upper limit, as it is affected by the street light mercury line (Hg I λ4358.3).

The 2D distribution of $T_e$([O III]) and $T_e$([O II]) in IC 132 appears to be rather uniform in the high surface brightness region surrounded by slightly hotter gas. The mean values are 16 100 K for $T_e$([O III]) and between 15 300 and 13 700 K for $T_e$([O II]) with an rms scatter per spaxel of about 3200 K in all cases. For $T_e$([S III]) we find a
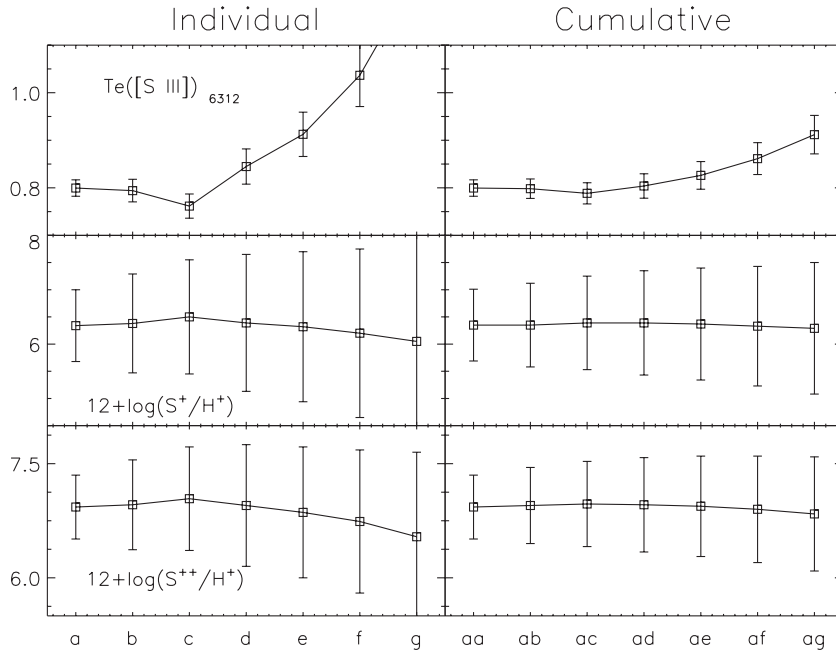
**Figure 33.** BCLMP 93 temperature and ionic abundances estimated from the sulphur lines for the individual and cumulative shells.
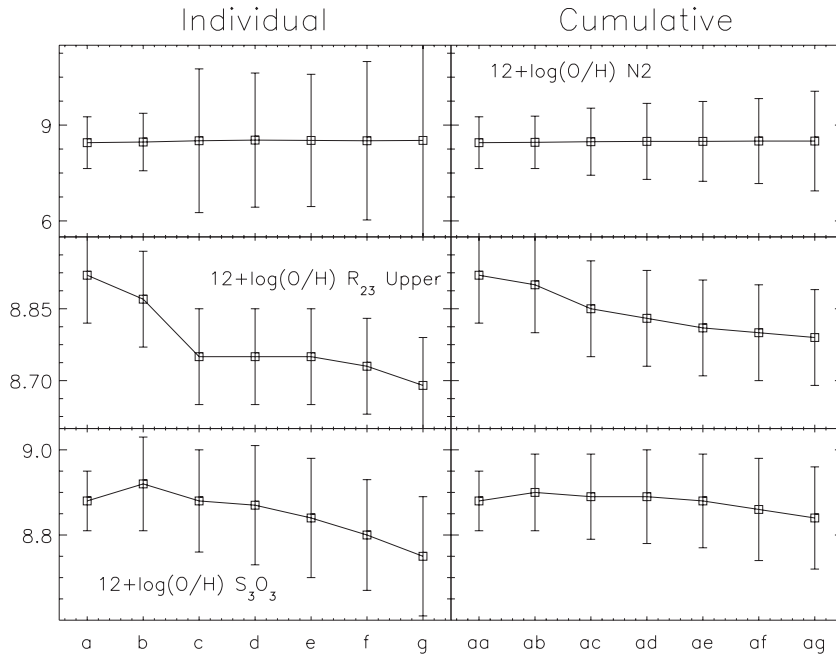


**Figure 34.** BCLMP 93 empirical abundance estimates for the individual and cumulative shells.

mean value of 16 200 K with an rms of 3800 K over 279 spaxels. Given that the maps include about 300 spaxels, the error of the mean temperatures is less than 600 K. These results are confirmed by the segmentation analysis that shows a positive gradient in all temperature estimates and a global cumulative value of 13 500 K for $T_e$([O II]) and 15 100 for $T_e$([O III]) while $T_e$([S III]) reaches an asymptotic value of 13 600 K.

Higher $T_e$([S III]) is derived for IC 132 than for BCLMP 93. This is in agreement with the centre being more metallic than the disc. Consequently, in the central regions cooling is more efficient through fine structure lines in the IR.

The analysis in shells indicates that the direct method is reliable for the brightest zones. However, as the radial distance within the regions increases, the lines are still detected in the integrated spectra and can be included in the usual temperature computation, but the inclusion of fainter zones produces physically unrealistic temperature values.

This can be seen in Tables 7 and 11 and in Figs 22 and 33 where the outer ring drives the temperatures up. This is true for temperature determinations using [O III] $\lambda$4363 and [O II] $\lambda$6312 and hence cannot be attributed just to the contamination of [O III] $\lambda$4363 by street lights due to the particular blueshift of M33.
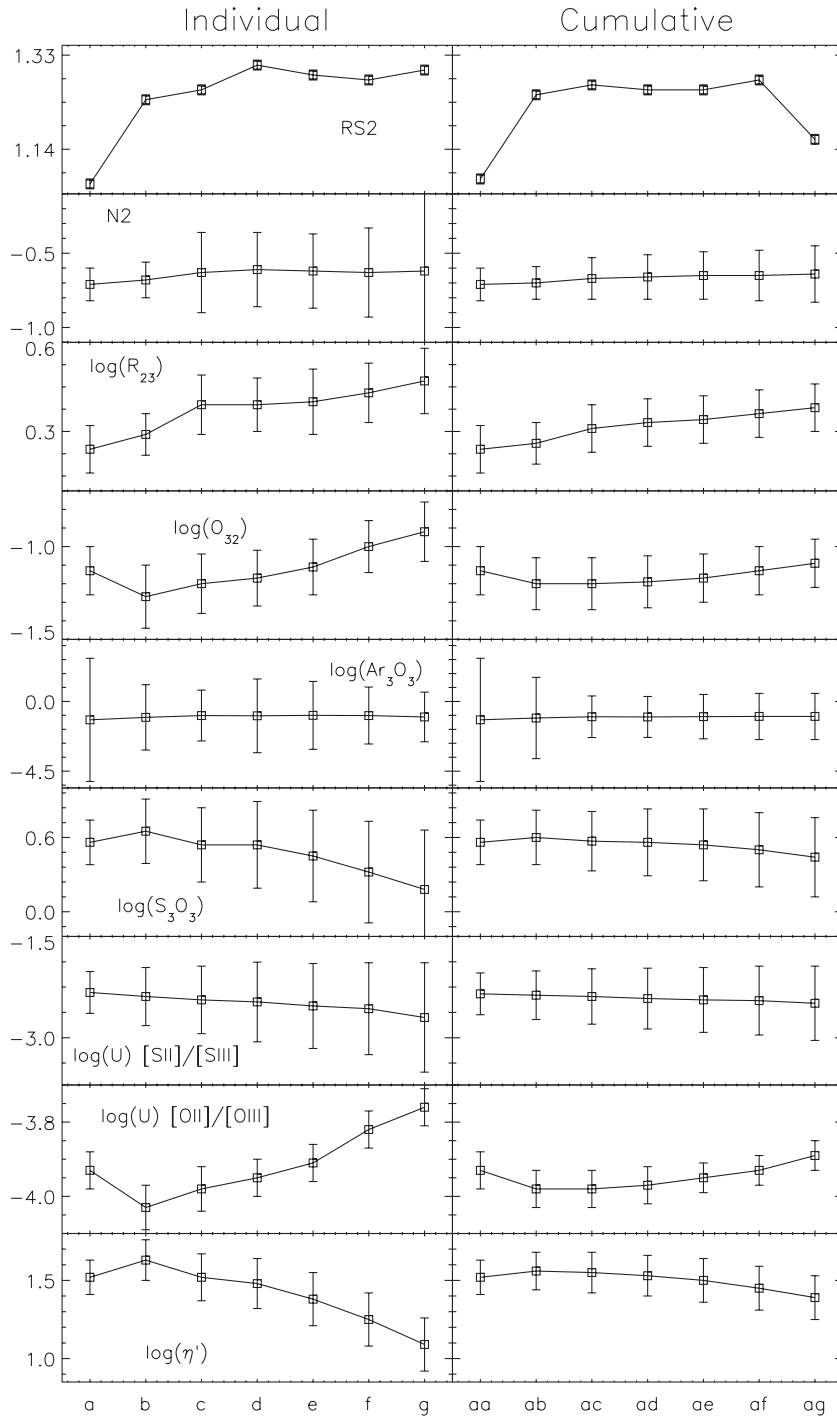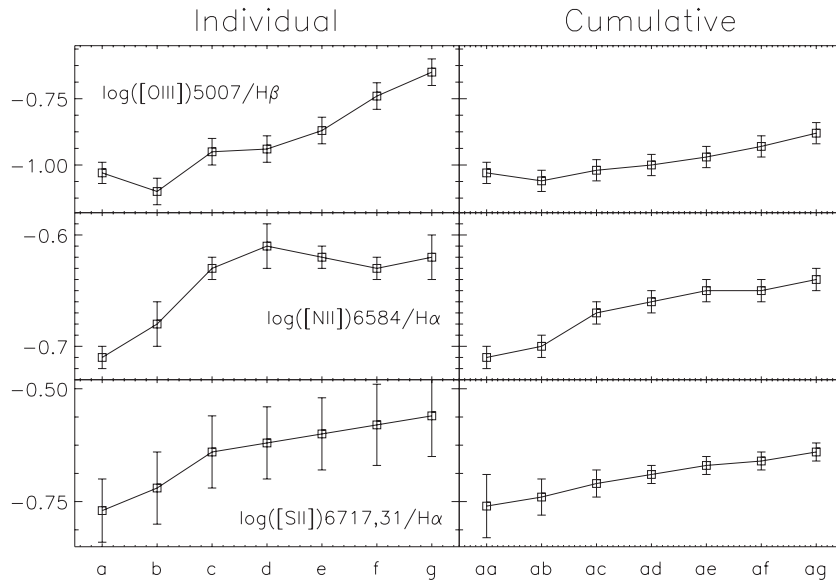
**Figure 35.** BCLMP 93 line ratios for the individual and cumulative shells.

(v) *Abundances.* The smallest dispersion in O/H determined from empirical indicators is obtained for O3N2 followed by N2. Although the related line ratio may have a large dispersion along the region, whether or not it is transferred to (O/H) depends on the calibration of the relation. If the conversion is lineal, the steepness of the slope dictates the dispersion in (O/H). This is why the oxygen abundances from O3N2 and N2 are almost constant *despite the fact that the line ratios have been discarded as good indicators because of their larger dependence on excitation (Relaño et al. 2010).*

$R_{23}$ displays a dispersion of $\sim$0.3 dex for the central zone; however, when individual spaxels are converted to (O/H) an extra difficulty is found because the upper and lower branches are included for the same object; thus, the spaxels in the transition zone have larger uncertainty depending on the calibration chosen. This is worse for the (Pilyugin 2001a) method because a first estimation of (O/H) is required and the area of transition between branches is not defined. *The fact that for the same region both branches are involved is suspicious and raises the question about the validity of the method when applied to individual spaxels.*

**Figure 36.** BCLMP 93 ionization ratios for the individual and cumulative shells.
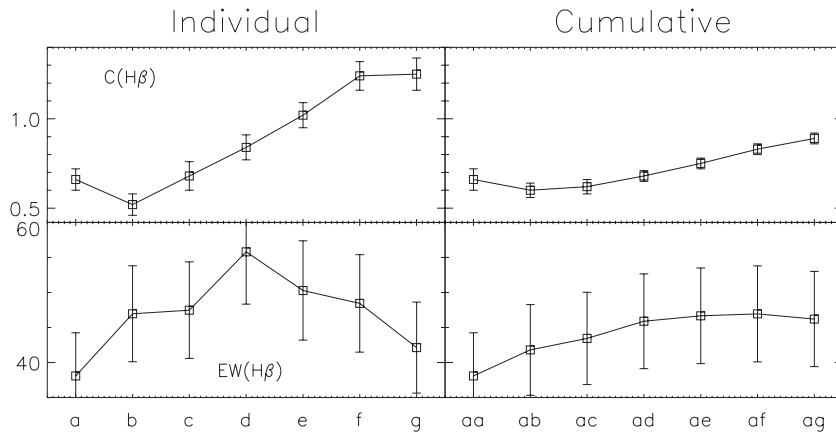


**Figure 37.** BCLMP 93 extinction parameter and EW(H$\beta$) for the individual and cumulative shells.

Sulphur is the only direct indicator in common for IC 132 and BCLMP 93. It shows higher abundance for the central region, coinciding with the results for the rest of the empirical indicators.

(vi) *Diagnostic diagrams.* Our search for systematic differences between the inner and outer H II regions in M33 was complemented with the use of diagnostic diagrams. In particular, we focused on the [O III] $\lambda$5007/H$\beta$, versus [N II] $\lambda$6584/H$\alpha$ diagram and found that the individual spaxels display a wide range of ionization conditions, extending by more than 2.5 dex from the location of the brightest spot. The distribution of points for the two H II regions considered displays a striking clear dichotomy. While the points for BCLMP 93 show a vertical scatter, the points for IC 132 have a horizontal spread orthogonal to that of BCLMP 93. The regions occupied by the distributions have hardly any superposition, while some points clearly move away from the H II region zone of the diagnostic diagram intruding in the AGN and transition zone. This intrusion raises a question about the wisdom of using the results of global models in the diagnostic diagrams for individual spaxels of resolved systems, including the definition of the H II boundary line.

Thus, it is important to be cautious when applying or comparing model predictions for global observations to spatially resolved data.

In this case, the BPT diagnostic diagrams may give misleading results for spaxels with ionization conditions that may not be reached in global spectra (Ercolano et al. 2012).

Bearing this in mind we computed pseudo-3D photoionization models and compared the distributions of observed line ratios in the diagnostic diagram with the results of our photoionization models and found that it was possible to reproduce the spread observed in the [O III] $\lambda$5007/H$\beta$ versus [N II] $\lambda$6584/H$\alpha$ diagram for both zones. We conclude that the position and horizontal spread of points in IC 132 are reproduced by models with high $U$, high $T_*$ and low $Z$, while the position and the vertical scatter of the observed points in the central H II regions are better reproduced by models with lower $U$ and $T_*$ and higher $Z$. The contribution of the central X-ray source to the ionization budget is not clear, since not very anomalous line ratios were detected in its proximity.

(vii) *WR stars.* Blue WR features were isolated and characterized for IC 132; the spatial resolution is enough to distinguish two concentrations. No WR features were detected in the central zone in apparent discordance with theoretical predictions that higher metallicity regions should have larger WR content, but perhaps consistent with the estimated larger age of the central region.

## ACKNOWLEDGMENTS

## REFERENCES

Abbott D. C., Conti P. S., 1987, ARA&A, 25, 113
Aggarwal K. M., Keenan F. P., 1999, ApJS, 123, 311
Aller L. H., 1942, ApJ, 95, 52
Allington-Smith J., 2006, New Astron. Rev., 50, 244
Alloin D., Collin-Souffrin S., Joly M., Vigroux L., 1979, A&A, 78, 200
Alonso-Herrero A., García-Marín M., Monreal-Ibero A., Colina L., Arribas S., Alfonso-Garzón J., Labiano A., 2009, A&A, 506, 1541
Alonso-Herrero A., García-Marín M., Rodríguez Zaurín J., Monreal-Ibero A., Colina L., Arribas S., 2010, A&A, 522, A7
Baldwin J. A., Phillips M. M., Terlevich R., 1981, PASP, 93, 5
Barbosa F. K. B., Storchi-Bergmann T., Cid Fernandes R., Winge C., Schmitt H., 2009, MNRAS, 396, 2
Barker T., 1980, ApJ, 240, 99
Blackman C. P., 1983, MNRAS, 202, 379
Boksenberg A., Willis A. J., Searle L., 1977, MNRAS, v, 15ᴘ
Bothun G. D., 1992, AJ, 103, 104
Boulesteix J., Courtes G., Laval A., Monnet G., Petit H., 1974, A&A, 37, 33
Bresolin F., Garnett D. R., Kennicutt R. C., Jr, 2004, ApJ, 615, 228
Bresolin F., Stasińska G., Vílchez J. M., Simon J. D., Rosolowsky E., 2010, MNRAS, 404, 1679
Cairós L. M., Caon N., Papaderos P., Kehrig C., Weilbacher P., Roth M. M., Zurita C., 2009a, ApJ, 707, 1676
Cairós L. M., Caon N., Zurita C., Kehrig C., Weilbacher P., Roth M., 2009b, A&A, 507, 1291
Castañeda H. O., Vílchez J. M., Copetti M. V. F., 1992, A&A, 260, 370
Cheng K. P., Collins N., Angione R., Talbert F., Hintzen P., Smith E. P., Stecher T., The UIT Team, 1997, Uv/visible Sky Gallery on CDROM. UITVi; Vol. U
Christensen T., Petersen L., Gammelgaard P., 1997, A&A, 322, 41
Copetti M. V. F., Writzl B. C., 2002, A&A, 382, 282
Corbelli E., Salucci P., 2000, MNRAS, 311, 441

Crockett N. R., Garnett D. R., Massey P., Jacoby G., 2006, ApJ, 637, 741
De Robertis M. M., Dufour R. J., Hunt R. W., 1987, 81, 195
Denicoló G., Terlevich R., Terlevich E., 2002, MNRAS, 330, 69
Díaz A. I., Pérez-Montero E., 2000, MNRAS, 312, 130
Diaz A. I., Terlevich E., Pagel B. E. J., Vílchez J. M., Edmunds M. G., 1987, MNRAS, 226, 19
Díaz Á. I., Terlevich E., Castellanos M., Hägele G. F., 2007, MNRAS, 382, 251
Dinerstein H. L., 1990, in Thronson H. A., Shull J. M., eds, The Interstellar Medium in Galaxies. Kluwer, Dordrecht, the Netherlands, p. 257
D'Odorico S., Benvenuti P., 1983, MNRAS, 203, 157
Dors O. L., Jr, Storchi-Bergmann T., Riffel R. A., Schimdt A. A., 2008, A&A, 482, 59
Edmunds M. G., Pagel B. E. J., 1984, MNRAS, 211, 507
Ercolano B., Dale J. E., Gritschneder M., Westmoquette M., 2012, MNRAS, 420, 141
Ferland G. J., Korista K. T., Verner D. A., Ferguson J. W., Kingdon J. B., Verner E. M., 1998, PASP, 110, 761
Fischer C., Tachiev G., 2004, At. Data Nucl. Data Tables, 87, 1
Fischer C., Tachiev G., Irimia A., 2006, At. Data Nucl. Data Tables, 92, 607
Foschini L., Rodriguez J., Fuchs Y., Ho L. C., Dadina M., Di Cocco G., Courvoisier T. J.-L., Malaguti G., 2004, A&A, 416, 529
Freedman W. L. et al., 2001, ApJ, 553, 47
García-Benito R. et al., 2010, MNRAS, 408, 2234
García-Marín M., Colina L., Arribas S., Monreal-Ibero A., 2009, A&A, 505, 1319
Garnett D. R., 1992, AJ, 103, 1330
Hägele G. F., Pérez-Montero E., Díaz Á. I., Terlevich E., Terlevich R., 2006, MNRAS, 372, 293 (H06)
Hägele G. F., Díaz Á. I., Terlevich E., Terlevich R., Pérez-Montero E., Cardaci M. V., 2008, MNRAS, 383, 209
Hodge P. W., Skelton B. P., Ashizawa J., 2002, An Atlas of Local Group Galaxies. Kluwer, Dordrecht
Hudson C. E., Bell K. L., 2005, A&A, 430, 725
Izotov Y. I., Stasińska G., Meynet G., Guseva N. G., Thuan T. X., 2006, A&A, 448, 955
James B. L., Tsamis Y. G., Barlow M. J., 2010, MNRAS, 401, 759
Kauffmann G. et al., 2003, MNRAS, 346, 1055
Keel W. C., 1983, ApJS, 52, 229
Kelz A. et al., 2006, PASP, 118, 129
Kennicutt R. C., Jr, 1998, ARA&A, 36, 189
Kennicutt R. C., Jr, Keel W. C., Blaha C. A., 1989, AJ, 97, 1022
Kennicutt R. C., Jr, Bresolin F., Garnett D. R., 2003, ApJ, 591, 801
Kent S. M., 1987, AJ, 94, 306
Kobulnicky H. A., Kennicutt R. C., Jr, Pizagno J. L., 1999, ApJ, 514, 544
Kewley L. J., Dopita M. A., 2002, ApJS, 142, 35
Kewley L. J., Ellison S. L., 2008, ApJ, 681, 1183
Kinkel U., Rosa M. R., 1994, A&A, 282, L37
Kobulnicky H. A., Kennicutt R. C., Jr, Pizagno J. L., 1999, ApJ, 514, 544
Kormendy J., McClure R. D., 1993, AJ, 105, 1793
Kosugi G. et al., 1995, PASP, 107, 474
Kwitter K. B., Aller L. H., 1981, MNRAS, 195, 939
Lagos P., Telles E., Muñoz-Tuñón C., Carrasco E. R., Cuisinier F., Tenorio-Tagle G., 2009, AJ, 137, 5068
Leitherer C. et al., 1999, ApJS, 123, 3
McCall M. L., Rybski P. M., Shields G. A., 1985, ApJS, 57, 1
McGaugh S. S., 1991, ApJ, 380, 140
McLaughlin B. M., Bell K. L., 1998, J. Phys. B: At. Mol. Phys., 31, 4317
Magrini L., Corbelli E., Galli D., 2007a, A&A, 470, 843
Magrini L., Vílchez J. M., Mampaso A., Corradi R. L. M., Leisy P., 2007b, A&A, 470, 865
Magrini L., Stanghellini L., Corbelli E., Galli D., Villaver E., 2010, A&A, 512, A63
Maíz-Apellániz J., Pérez E., Mas-Hesse J. M., 2005, in de Grijs R., González Delgado R. M., eds, Starbursts: From 30 Doradus to Lyman Break Galaxies. Springer, Dordrecht, p. P44
Massey P., Bianchi L., Hutchings J. B., Stecher T. P., 1996, ApJ, 469, 629

Massey P., Olsen K. A. G., Hodge P. W., Strong S. B., Jacoby G. H., Schlingman W., Smith R. C., 2006, AJ, 131, 2478
Meynet G., Maeder A., 2005, A&A, 429, 581
Middleton M. J., Sutton A. D., Roberts T. P., 2011, MNRAS, 417, 464
Minniti D., Olszewski E. W., Rieke M., 1993, ApJ, 410, L79
Monreal-Ibero A., Relaño M., Kehrig C., Pérez-Montero E., Vílchez J. M., Kelz A., Roth M. M., Streicher O., 2011, MNRAS, 413, 2242
Pagel B. E. J., Edmunds M. G., Blackwell D. E., Chun M. S., Smith G., 1979, MNRAS, 189, 95
Pettini M., Pagel B. E. J., 2004, MNRAS, 348, L59
Pérez-Montero E., Díaz A. I., 2003, MNRAS, 346, 105
Pérez-Montero E., Díaz A. I., 2005, MNRAS, 361, 1063
Pérez-Montero E., Díaz A. I., Vílchez J. M., Kehrig C., 2006, A&A, 449, 193
Pérez-Montero E. et al., 2011, A&A, 532A, 141
Pilyugin L. S., 2001a, A&A, 369, 594
Pilyugin L. S., 2001b, A&A, 373, 56
Pilyugin L. S., 2001c, A&A, 374, 412
Pindao M., Schaerer D., González Delgado R. M., Stasińska G., 2002, A&A, 394, 443
Raimann D., Storchi-Bergmann T., Bica E., Melnick J., Schmitt H., 2000, MNRAS, 316, 559
Ramsbottom C. A., Bell K. L., 1996, At. Data Nucl. Data Tables, 54, 357
Regan M. W., Vogel S. N., 1994, ApJ, 434, 536
Relaño M., Monreal-Ibero A., Vílchez J. M., Kennicutt R. C., 2010, MNRAS, 402, 1635
Rosolowsky E., Simon J. D., 2008, ApJ, 675, 1213
Roth M. M. et al., 2005, PASP, 117, 620
Rubin R. H., 1989, in Torres-Peimbert S., ed., Proc. IAU Symp. 131, Planetary Nebulae. Kluwer, Dordrecht, p. 221
Sánchez S., 2004, Astron. Nachr., 325, 167
Sánchez S. T., Becker A., Kelz A., 2004, Astron. Nachr., 325, 171

Sánchez S., Cardiel N., 2005, Calar Alto Newsletter, n.10
Sánchez S. F., Aceituno J., Thiele U., Pérez-Ramírez D., Alves J., 2007, PASP, 119, 1186
Schaerer D., Vacca W. D., 1998, ApJ, 497, 618
Searle L., 1971, ApJ, 168, 327
Shaw R. A., Dufour R. J., 1995, PASP, 107, 896
Skillman E. D., 1998, in Aparicio A., Herrero A., Sanchez F., eds, Stellar Astrophysics for the Local Group: VIII Canary Islands Winter School of Astrophysics. Cambridge Univ. Press, Cambridge, p. 457
Smith H. E., 1975, ApJ, 199, 591
Stasińska G., 1990, A&AS, 83, 501
Stasińska G., 2002, Rev. Mex. Astron. Astrofis. Ser. Conf., 12, 62
Stasińska G., 2006, A&A, 454, L127
Stasińska G., Cid Fernandes R., Mateus A., Sodré L., Asari N. V., 2006, MNRAS, 371, 972
Storchi-Bergmann T., Calzetti D., Kinney A. L., 1994, ApJ, 429, 572
Tayal S. S., 2007, ApJS, 171, 331
Tayal S. S., Gupta G. P., 1999, ApJ, 526, 544
van den Bergh S., 1991, PASP, 103, 609
van den Bergh S., 2000, The Galaxies of the Local Group, 1st edn. Cambridge Univ. Press, Cambridge
Veilleux S., Osterbrock D., 1987, ApJS, 63, 295
Vílchez J. M., Esteban C., 1996, MNRAS, 280, 720
Vílchez J. M., Pagel B. E. J., Diaz A. I., Terlevich E., Edmunds M. G., 1988, MNRAS, 235, 633
Wang W., Liu X.-W., Zhang Y., Barlow M. J., 2004, A&A, 427, 873
Weng S.-S., Wang J.-X., Gu W.-M., Lu J.-F., 2009, PASJ, 61, 1287
Zaritsky D., Kennicutt R. C. Jr, Huchra J. P., 1994, ApJ, 420, 87

This paper has been typeset from a TEX/LATEX file prepared by the author.